HIGH-RESOLUTION LASER RADAR PERFORMANCE ANALYSIS

by

DONGWOOK PARK

S.B., Massachusetts Institute of Technology
(1982)

S.M., Massachusetts Institute of Technology
(1984)

SUBMITTED IN PARTIAL FULFILLMENT
OF THE REQUIREMENTS FOR THE
DEGREE OF

DOCTOR OF PHILOSOPHY

at the

MASSACHUSETTS INSTITUTE OF TECHNOLOGY

January 1988

© Massachusetts Institute of Technology, 1988

Signature cf Author ....
Department of Electrical Engineering and
Computer Science,
January 1988

Certified by . ...
Jeffrey H. Shapiro
Thesis Supervisor

Accepted by . ι ....
Arthur C. Smith
Chairman, Department Committee on Graduate Students

HIGH-RESOLUTION LASER RADAR PERFORMANCE ANALYSIS

by

DONGWOOK PARK

Submitted to the Department of Electrical Engineering
and Computer Science on January 20th, 1988
in partial fulfillment of the requirements for the Degree of
Doctor of Philosophy

ABSTRACT

High-resolution microwave radars, such as synthetic aperture radars (SAR's) and range-Doppler (RD) radars, exploit coherent target return processing to achieve spatial resolution better than the diffraction limits of their antennas. These techniques applied in the laser radar context provide the same resolution enhancement on top of the improved diffraction-limit afforded by their much shorter operating wavelengths. This thesis develops a self-consistent laser radar system theory for these coherent imaging systems and analyzes their performance, measured by spatial resolution, carrier-to-noise ratio (CNR), and signal-to-noise ratio (SNR), in a variety of situations. Analysis of the effects that laser frequency instability, atmospheric turbulence, target/radar motion errors, and laser speckle have on the system performance are stressed. Preliminary evaluation of the results indicates that these imagers may be feasible in the near future.

Thesis Supervisor: Jeffrey H. Shapiro

Title: Professor of Electrical Engineering

ACKNOWLEDGEMENTS

I would like to thank my thesis supervisor Professor Jeffrey H. Shapiro for his guidance and support. He has been everything a graduate student could ask for in a thesis supervisor. I am deeply grateful to him.

To the members of the Optical Propagation and Communication Group at MIT, I owe much thanks for their company over the years. I would like to thank Kin-Wai Leong, Naomi Zirkind, and Seng-Tiong Ho in particular for many useful discussions on both technical and nontechnical matters.

Finally, I want to thank my parents, who have sacrificed so much for their children. I dedicate this thesis to them.

To my parents

TABLE OF CONTENTS

LIST OF FIGURES

CHAPTER I

INTRODUCTION

1.1. Motivation and Introduction

Radars can yield useful information about the nature of the targets. Although they have been operated at wavelengths from meters to fractions of a micron, the vast preponderance of radar systems are microwave radars, working at centimeter wavelengths [1]. These microwave radars provide adequate angular, range, and velocity resolution for many applications, and operate at wavelengths for which the absorption and scattering characteristics of the atmosphere are relatively benign [1,2]. In some applications, however, laser radars, operating in the optical or infrared (IR) frequency bands, offer significant advantages over their microwave counterparts.

In recent years, there has been considerable interest in developing coherent laser radars, i.e., radars which use laser sources and coherent optical (heterodyne) detection [3-7]. For a variety of reasons, the focus of this activity has been on 10.6 μm wavelength systems using CO_2 lasers [3,4,6]. The attractiveness of laser systems vis a vis microwave systems is three-fold. First, a diffraction-limited radar antenna of diameter D produces a far-field angular beamwidth of approximately λ/D at wavelength λ. This gives a 10 μm wavelength radar a beamwidth 1,000 times narrower than that of a

1 cm wavelength radar of the same antenna size. Second, a radar using pulses of duration τ can infer target range (from roundtrip delay) to a resolution of approximately $c\tau/2$, where c is the speed of light [1,8]. Laser systems can therefore afford much better range resolution than microwave systems in that they can employ far shorter pulse durations. Finally, a Doppler (velocity measuring) radar of dwell time T has a velocity resolution of roughly $\lambda/4T$ [1,8]. Once again, the shortness of laser wavelengths compared to microwave wavelengths offers a dramatic improvement. These fundamental advantages must be tempered, however, by key disadvantages of laser radars, namely, problems with atmospheric propagation caused by turbulence and turbidity [9-11], problems with target-induced fluctuations (laser speckle) [12], and the relative immaturity of laser radar technology as compared to microwave techonology. In fact, it seems clear already that laser radars will develop to fill new application niches, rather than supplanting microwave systems in their present uses.

This thesis is concerned with system theory for coherent laser radars. Previous efforts in this regard have concentrated on conventional imaging configurations (angle-angle imaging) in which the radar beam is scanned across the target, and intensity and/or range and/or Doppler shift measurements are accumulated at a raster of picture elements (pixels). These studies have established the basic intermediate frequency (IF) signal models for such systems [6,13], as well as quantified the impact of

atmospheric turbulence and target speckle on imaging performance
[6,14-16]. In essence, these studies have applied microwave
radar theory with modifications dictated by the different physics
of the optical situations. Our interest is similar in spirit,
but the laser radars we shall address are high-resolution imaging
systems, namely synthetic aperture radars and range-Doppler
radars [17-19]. Our primary interest in these imagers is based
on the fact that in some applications, for example detailed
mapping of terrain or navigational guidance, the
diffraction-limited spatial resolution of angle-angle imagers may
not be good enough. The high-resolution imagers, on the other
hand, are capable of better-than-diffraction-limited spatial
resolution through coherent processing of the target return.

High-resolution imaging radars in the microwave range have
existed for some time, with synthetic aperture radars (SAR) and
range-Doppler (RD) radars leading the way. Significant success
has been achieved with SAR's in the area of high-resolution
terrain imaging [20], while the primary application of RD radars
has been in radar astronomy [21,22]. In both SAR and RD imaging,
there is a relative motion between the radar and the target, and
range-delay and Doppler shift measurements are utilized to form a
high-resolution image of the target.

Microwave treatments of SAR and RD imaging have not
addressed a variety of issues that may be of paramount importance
for optical systems of these genres. Laser frequency
instability, atmospheric turbulence, laser speckle, and

target/radar platform vibrations are particular examples. The main thrust of this thesis is to fill these gaps by developing laser radar system theory results for these high-resolution imagers, starting from the available laser radar IF signal model. That will in turn help us better assess the comparative benefits of operating these imagers in the optical and/or IR end of the spectrum.

1.2. Thesis Outline

The thesis is organized as follows. In Chapter II, we describe in some detail the basic laser radar system model. This model consists of four major parts: transmitter, atmospheric propagation, target interaction, and receiver front end. It is essentially the same as the one used in conventional-imaging laser radar theory. Thus, we expect to be able to compare the merits of the high-resolution imagers we shall study against angle-angle imagers on a fair basis.

In Chapter III, we discuss the performances of SAR's and RD radars under ideal operating conditions. The performances are evaluated in terms of spatial resolution, carrier-to-noise ratio (CNR), and signal-to-noise ratio (SNR). We start off by going over the underlying principle of high-resolution imagers in general, and then, we apply the specifics to first SAR's and then to RD radars. In the SAR section, we first examine the unmodulated continuous-wave (CW) case, showing how a dramatic

improvement in the azimuthal (along-track) resolution can be achieved, and then, we extend our analysis by introducing a temporal modulation into this radar for improved cross-track resolution. The RD radar section looks at the special case of imaging a spatially unresolved rotating target. In the first half of the section, we examine a processing architecture that employs a bank of matched-filters, wherein the notion of ambiguity function plays a key role. The second half deals with an architecture that largely overcomes the tradeoff constraint between the range and Doppler resolutions which arises in the first architecture.

In chapter IV, we investigate the degradation of imager performance brought on by problems such as laser frequency instability, atmospheric turbulence, and target/radar motion errors. In each case, we take the basic framework developed in Chapters II and III and accomodate within that framework an appropriate statistical model which represents the particular problem being addressed. Results of these analyses are compared against the results of the ideal case in Chapter III and interpreted in physical terms. We also lock at how systems employing different types of transmitted waveforms are affected by these various perturbations.

In Chapter V, we take some prototype imaging systems and look at how such systems might perform under a variety of realistic scenarios. This is done by using a set of reasonable values for transmitter, receiver and perturbation model

parameters. The results are discussed. Feasibility of these imagers is discussed based on these results.

Chapter VI contains the summary of the thesis and a list of recommended future work. Some of the items on the list include: relaxing various assumptions made in the thesis; investigating performance optimization issues in regard to the choice of system parameters; and finally, examining alternative/additional processing architectures to improve the performance of the high-resolution laser radars.

CHAPTER II

LASER RADAR SYSTEM MODEL

Consider the generic coherent laser radar system shown in block diagram form in Fig. 2.1. In this system, the modulated output of a transmitter laser is shaped by beam formation optics, and directed by scanning/pointing plus exit optics. After propagating through an atmospheric path, the resulting illumination beam reflects off a target. This reflected beam propagates back through the atmosphere to the radar receiver, where it is collected by entrance plus scanning and pointing optics. The collected target return field is superposed, through a beam combiner, with the field of a strong local oscillator laser on the surface of a photodetector. The local oscillator is coherent with the transmitter laser, but operates at an intermediate frequency offset, ν_{IF}, from the transmitter laser carrier frequency. Bandpass filtering is used to select out the photocurrent beat frequency components in the vicinity of ν_{IF}. These are then processed to yield target information.

The preceding system description is sufficiently general to encompass both the conventional angle-angle imaging systems [6] and the high-resolution imaging systems that will be the subject of this thesis. In this chapter, we shall draw, therefore, upon the basic system models employed in the studies of conventional imagers to provide the foundation for our analyses. For the most part, as in the previous theoretical work [6], technological

(a)

(b)
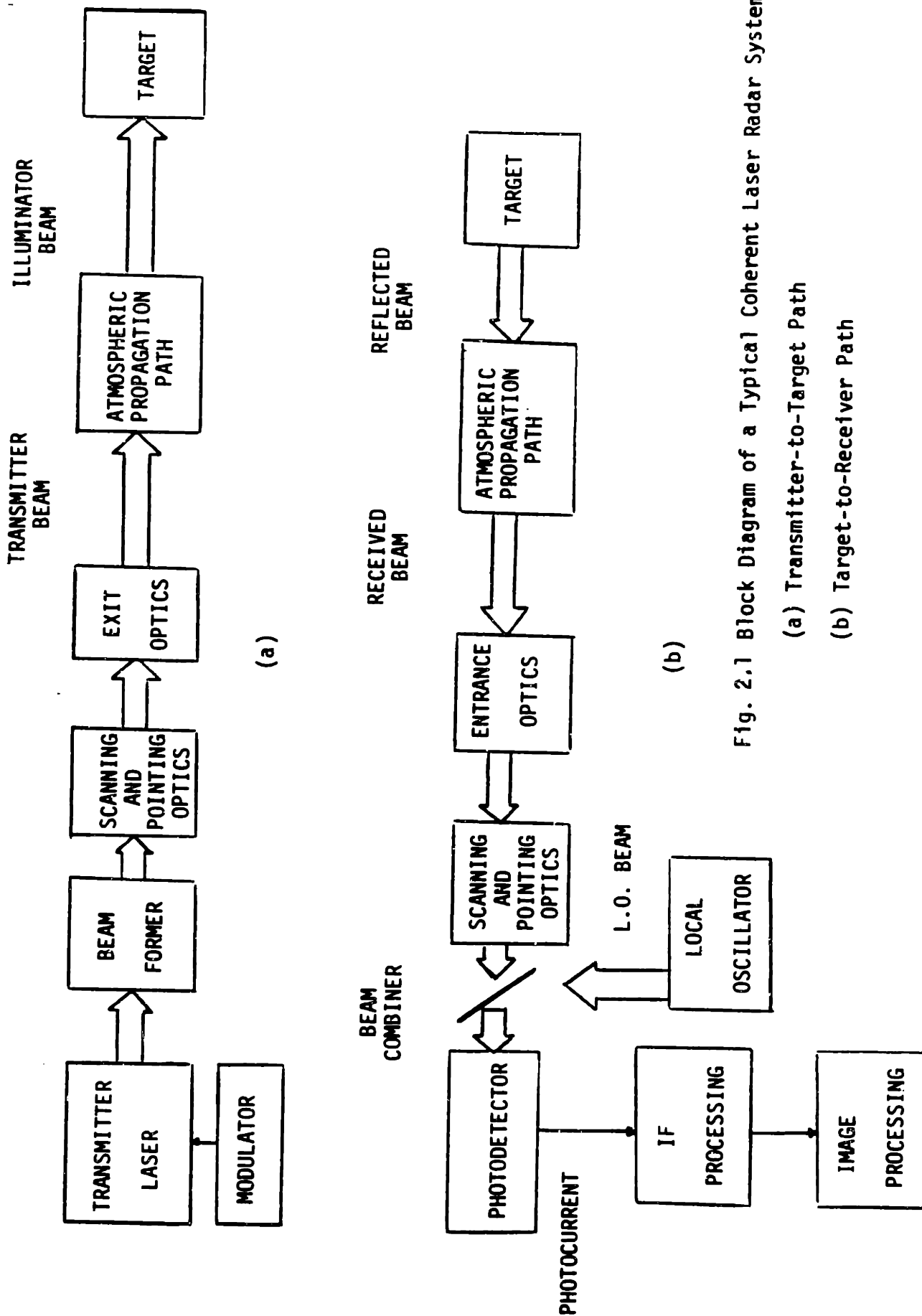
Fig. 2.1 Block Diagram of a Typical Coherent Laser Radar System

(a) Transmitter-to-Target Path

(b) Target-to-Receiver Path

details will not be carefully included. However, where appropriate, analytical assumptions commensurate with current practice in experimental CO_2 laser radars will be employed. In this regard, we shall assume henceforth that, unless stated otherwise, the system of interest is a monostatic shared optics radar in which the transmitter and the receiver employ a common telescope equipped with an appropriate optical transmit/receive (T/R) switch, as is done in MIT Lincoln Laboratory test bed radars [3].

The laser radar system model divides naturally into four parts: the transmitter, the propagation path, the target, and the receiver front end (up to but not including the image processing part). Although all of these elements are sensitive to the vector (polarization) characteristics of optical radiation, we shall follow the usual scalar-wave modelling approach.

2.1. Transmitter Model

Let the exit pupil of the transmitter be at the $z=0$ plane in a Cartesian coordinate system. The transmitter model characterizes $E_T(\bar{p},t)$, the real-valued optical-frequency field of the transmitter beam ($[W/m^2]^{1/2}$), as a function of transverse coordinates $\bar{p} = (x,y)$ and time t. We shall assume narrowband (quasimonochromatic) operation about center frequency ν_0 (Hz), corresponding to a nominal wavelength $\lambda = c/\nu_0$. It is thus convenient to work with complex envelopes in all our field

manipulations, i.e., we deal with $\underline{E}_T(\bar{p},t)$, a complex-valued baseband field such that

$$E_T(\bar{p},t) = \text{Re}\{ \underline{E}_T(\bar{p},t)\exp[-j2\pi\nu_0 t] \}. \qquad (2.1.1)$$

The normalization employed in defining $\underline{E}_T$ will be taken to be that which makes $| \underline{E}_T(\bar{p},t)|^2$ the short-time average power density of the transmitter beam at $(\bar{p},t)$ in the exit pupil. The spatio-temporal characteristics of the transmitter beam are the essence of the transmitter model. Mathematically, the following form is convenient for our purposes

$$\underline{E}_T(\bar{p},t) = \underline{s}(t) \; \underline{U}_T(\bar{p},t)\exp[-j\Phi(t)] , \qquad (2.1.2)$$

where

$\underline{s}(t)$ = temporal modulation (transmitted waveform),

$\underline{U}_T(\bar{p},t)$ = normalized spatial beam pattern,

$\Phi(t)$ = phase error due to frequency instability.

Let us consider the component terms in (2.1.2). The beam pattern $\underline{U}_T$ is normalized to satisfy $\int d\bar{p} \; | \underline{U}_T(\bar{p},t)|^2 = 1$, where the integration is carried out over the exit pupil area. It therefore represents, in its spatial dependence, the (assumed perfectly stable) transverse mode behavior of the transmitter laser as modified by the beam forming optics in Fig. 2.1a. The time dependence of $\underline{U}_T$ is taken to represent the effects of the pointer/scanner and/or transmitter motion. For stationary optics

on a motionless radar platform, $\underline{U}_T$ will be time independent. For stationary optics on a radar platform moving with velocity $\bar{v} = \bar{v}_T$ + $v_z\hat{z}$, where $\hat{z}$ is the z-axis unit vector and $\bar{v}_T$ ($\bar{v}_T \cdot \hat{z} = 0$) is the transverse velocity, we have

$$\underline{U}_T(\bar{p},t) = \underline{U}_T^O(\bar{p} - \bar{v}_T t)\exp[-jkv_z t] , \qquad (2.1.3)$$

with $k=2\pi/\lambda$ being the wavenumber. In Eq. (2.1.3), $\underline{U}_T^O$ is the fixed spatial beam pattern in the radar's rest-frame, and $\exp[-jkv_z t]$ is the Doppler shift arising from the longitudinal motion of the transmitter.

Because of the form of Eq. (2.1.1) and the normalization used for $\underline{U}_T$, it follows that $|\underline{s}(t)|^2$ is the transmitted power at time t, and (when $v_z = 0$, $\Phi(t) = 0$) $\arg(\underline{s}(t))$ is the transmitted phase modulation at time t. We use $\underline{s}(t)$ to represent a deterministic temporal modulation (amplitude, frequency, phase) imposed on the transmitter. Depending on the application, this modulation may be totally absent ($\underline{s}(t) =\sqrt{P_T}$ for a CW beam of power P_T), or it may represent a simple pulse or a train of pulses.

The preceding components of the transmitter model are all ideal in the sense that no random fluctuations are included. For the high-resolution imagers we want to study, assumption of a completely nonrandom transmitter during the coherent integration period is unrealistic. These imagers are particularly sensitive to the coherence (frequency stability) of the transmitter. Thus,

the $\Phi(t)$ term is included in (2.1.2) to introduce such instabilities. We shall take this term to be of the form

$$\Phi(t) = 2\pi \int_{-\infty}^{t} du \ \tilde{f}(u) , \qquad (2.1.4)$$

where $\tilde{f}(u)$ is the instantaneous frequency fluctuation. We will have more to say regarding the frequency stability issue in Chapter IV.

2.2. Propagation Model

There are three types of situations to consider when modelling the propagation of the transmitted beam to the target and/or propagation of the scattered beam to the receiver. They are: propagation through free-space, propagation through a turbulent atmosphere, and propagation through a turbid atmosphere. Among the three, turbid atmosphere propagation is of the least interest to us as the received signal energy is then typically insufficient for imaging. For angle-angle imaging, turbulence may be a very serious problem for large aperture systems, but perhaps not as important for compact (small aperture) systems [10,11,14]. For high-resolution imaging, the atmospheric coherence length, which reflects the turbulence strength, must be compared against not only the aperture size but also against the extent of the displacement of the radar and/or the target during the coherent integration time.

Free-space propagation is usually achievable only in
exoatmospheric situations; at 10.6 μm, absorption in the
atmosphere is significant [9].

For the most part in this thesis (except in the section that
deals with the effects of atmospheric turbulence), we will use
the free-space propagation model with a correction to account for
the atmospheric loss. In this regime, propagation of narrowband
optical radiation through distance L near the optical axis
(paraxial case) can be characterized by the following version of
the quasimonochromatic (QM) Huygens-Fresnel principle [10]

$$\underline{E}_L(\bar{p}',t) = \int_{z=0} d\bar{p}\ \underline{E}_i(\bar{p},t-L/c)\ \underline{h}(\bar{p} - \bar{p}')\ , \qquad (2.2.1)$$

where

$\underline{E}_i(\bar{p},t)$ = incident (input) field at z=0 plane,

$\underline{E}_L(\bar{p}',t)$ = propagated (output) field at z=L plane,

$\underline{h}(\bar{p})$ = $(1/j\lambda L)\exp[jkL + jk|\bar{p}|^2/2L - \alpha L/2]$.   (2.2.2)

Propagation of the incident field $\underline{E}_i$ through distance L
corresponds to, from a system theory point of view, passing
through a linear, space-invariant filter whose impulse response
is given by $\underline{h}(\bar{p})$ of (2.2.2). α in (2.2.2) is the effective
atmospheric attenuation coefficient with the unit of 1/m, and k =
$2\pi\nu_0/c$ is the wavenumber; L/c in (2.2.1) accounts for the nominal
delay of $\underline{E}_i$ due to the distance between the input and the output
planes. [If the incident field has a large temporal bandwidth,
the nominal delay L/c must be modified to include the transverse

coordinate dependence.] The spatial impulse response needs to be modified in the presence of atmospheric turbulence; this is done in Chapter IV.

In the Fraunhofer diffraction or far-field limit, where $D^2/\lambda L \ll 1$, with D being the size of the source aperture, (2.2.1) reduces to the following form

$$\underline{E}_L(\bar{p}',t) = \underline{h}(\bar{p}') \cdot \underline{\mathcal{E}}_i(\bar{p}'/\lambda L, t-L/c) , \qquad (2.2.3)$$

where

$$\underline{\mathcal{E}}_i(\bar{f},t-L/c) = \text{2D spatial Fourier transform of}$$
$$\underline{E}_i(\bar{p},t-L/c). \qquad (2.2.4)$$

Because of the reciprocity of free-space [23], the QM Huygens-Fresnel principle (2.2.1) can be used to describe both the propagation of the transmitted beam to the target plane, and the propagation of the scattered beam back to the transmitter/receiver. Therefore, the far-field approximation of Eqs. (2.2.3) and (2.2.4) may be used for the propagation of the scattered field as well, provided that the target is sufficiently small.

2.3. **Target Model**

Because of the short wavelengths employed in laser radars, target surfaces encountered in most situations can be characterized as rough surfaces, i.e., $\sigma_h \gg \lambda$ prevails where σ_h

is the target's rms surface height fluctuation. That makes it necessary to treat the scattering by the target in a statistical manner [12]. We will assume throughout the thesis that we are dealing only with surface scattering coming from diffuse (speckle) targets described above.

We shall adopt the following multiplicative model to describe the relationship between the incident field and the reflected field at the reference plane z=L, which is taken to be the nominal target plane (see Fig. 2.2) [6]:

$$\underline{E}_R(\bar{p},t) = \underline{T}(\bar{p}) \, \underline{E}_L(\bar{p},t) \, , \qquad (2.3.1)$$

where $\underline{E}_L(\bar{p},t)$ and $\underline{E}_R(\bar{p},t)$ correspond to the incident and the reflected fields at the z=L plane, respectively, and $\underline{T}(\bar{p})$ is complex field reflection coefficient of the target at $\bar{p}$. [We have assumed that the target is stationary.] The statistical model for $\underline{T}(\bar{p})$ at wavelength λ will be assumed to be [6,7,13]

$$< \underline{T}(\bar{p}) > \quad = 0 \, ,$$
$$< \underline{T}(\bar{p}) \, \underline{T}(\bar{p}') > \; = 0 \, , \qquad (2.3.2)$$
$$< \underline{T}(\bar{p}) \, \underline{T}^*(\bar{p}') > \; = \lambda^2 \mathcal{J}(\bar{p})\delta(\bar{p}-\bar{p}') \, ,$$

where $\mathcal{J}(\bar{p})$ represents the average reflectivity of the target surface at $\bar{p}$, and * denotes complex conjugation. Following the standard laser radar theory, $\underline{T}(\bar{p})$ is modelled as a circulo-complex Gaussian random process [6,8].

$$\underline{E}_L(\bar{\rho},t)$$

$$\underline{E}_R(\bar{\rho},t)$$

TARGET

$$\underline{E}_R(\bar{\rho},t) = \underline{T}(\bar{\rho})\underline{E}_L(\bar{\rho},t)$$

$$z = L \quad \text{TARGET PLANE}$$

$$\langle \underline{T}(\bar{\rho}) \rangle = 0$$

$$\langle \underline{T}(\bar{\rho})\underline{T}(\bar{\rho}') \rangle = 0$$
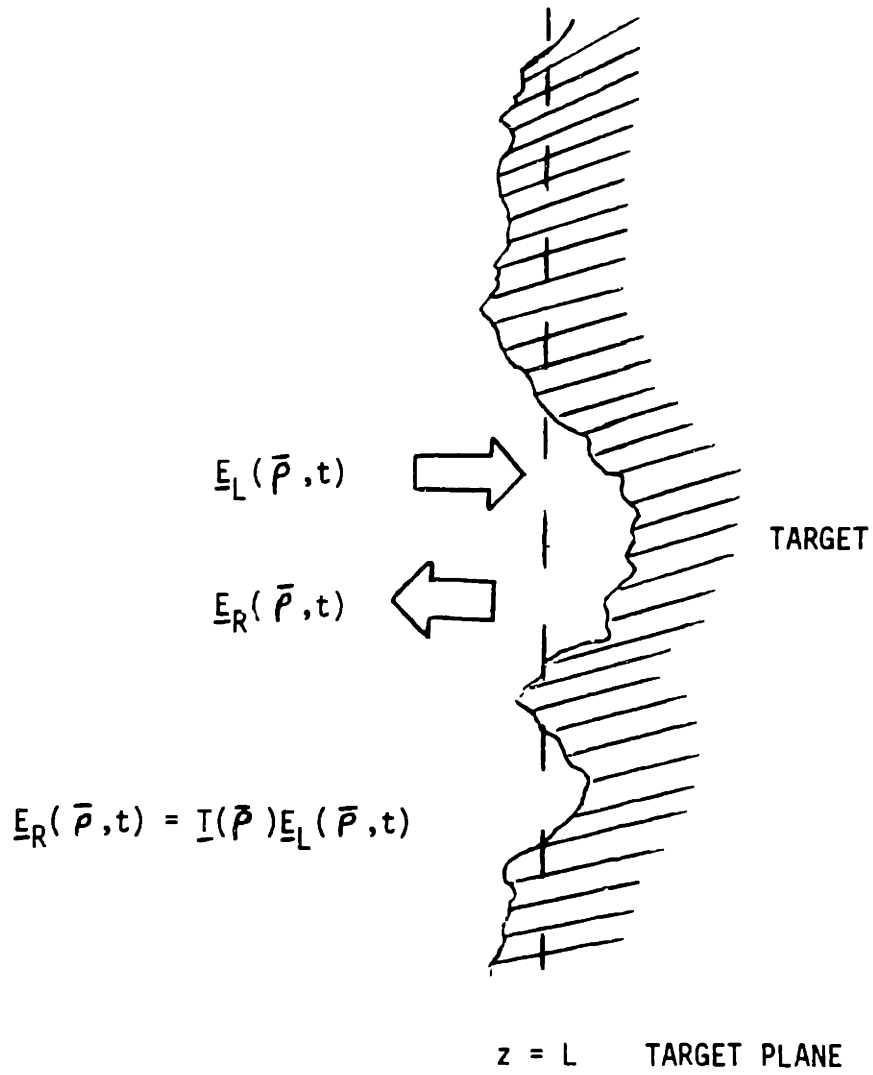
$$\langle \underline{T}(\bar{\rho})\underline{T}^*(\bar{\rho}') \rangle = \lambda^2 \underline{J}(\bar{\rho})\delta(\bar{\rho}-\bar{\rho}')$$

Fig. 2.2. Incident Beam-Target Interaction Model

A few remarks regarding the diffuse target model represented by (2.3.1) and (2.3.2) are in order. Physically, a rough target surface turns a spatially coherent incident beam into a spatially incoherent scattered beam. This effect, coupled with the temporal coherence of the source (laser), gives rise to the well-known laser speckle phenomenon [12], which degrades the quality of the target image and thus must be dealt with in the post-detection part of the receiver. The impulse $\delta(\bar{p}-\bar{p}')$ in (2.3.2) represents this spatial incoherence aspect of the scattering process. The dependence of $\mathcal{T}$ on $\bar{p}$ accomodates the spatial variation of the reflectivity strength. For imaging applications, i.e., for our purpose, $\mathcal{T}(\bar{p})$ will be the quantity of interest to us; we are trying to obtain a high-resolution image of $\mathcal{T}$.

2.4. Receiver Front End Model

Heterodyne photodetection is essential to all coherent laser radars since they require both phase and amplitude information of the target return. When the reflected field at the target plane is propagated back to the receiver (Fig. 2.1b), it goes through the heterodyne detection process.

After passing through the entrance optics, the target return field $\underline{E}_S(\bar{p},t)$ is combined with a CW local oscillator (LO) beam of frequency $v_0 - v_{IF}$ via a beam combiner. The LO field $\underline{E}_{LO}(\bar{p},t)$ is given by

$$\underline{E}_{LO}(\bar{p},t) = \sqrt{P_{LO}} \; \underline{U}_{LO}(\bar{p},t) \exp[j2\pi\nu_{IF}t]\exp[-j\Phi(t)], \qquad (2.4.1)$$

where P_{LO} is the LO beam power, and $\underline{U}_{LO}(\bar{p},t)$ is the normalized spatial LO beam pattern whose time dependence represents pointer/scanner and radar motion as in (2.1.3) for $\underline{U}_T$. Note that the frequency instability term $\Phi(t)$ is the same as that in (2.1.2) for $\underline{E}_T$ because we assume that the LO beam is derived from the same laser that is used to obtain the transmitter beam. The resultant beam from the beam combiner illuminates the photodetector, and the photocurrent from the detector is then passed through an IF filter. The IF filter is a bandpass filter whose center frequency is around ν_{IF}; its main function is to select out the signal component of the photocurrent [10].

In the limit of a strong LO beam, we can use the IF signal model shown in Fig. 2.3 for the normalized complex envelopes of the target return and the LO shot noise [10,24]:

$$r(t) = \text{Re} \{ \underline{r}(t) \exp[-j2\pi\nu_{IF}t] \}, \qquad (2.4.2)$$

where

$$\underline{r}(t) = \underline{y}(t) + \underline{n}(t), \qquad (2.4.3)$$

$\underline{n}(t) = $ LO shot noise

> $= $ zero-mean, circulo-complex, passband-filtered white Gaussian noise with spectral density $h\nu_0/\eta$,

$\underline{y}(t) = $ target return

$$= \int_{detector} d\bar{p} \; \underline{E}_S(\bar{p},t) \cdot \underline{U}_{LO}^{*}(\bar{p},t) \exp[j\Phi(t)] , \qquad (2.4.4)$$
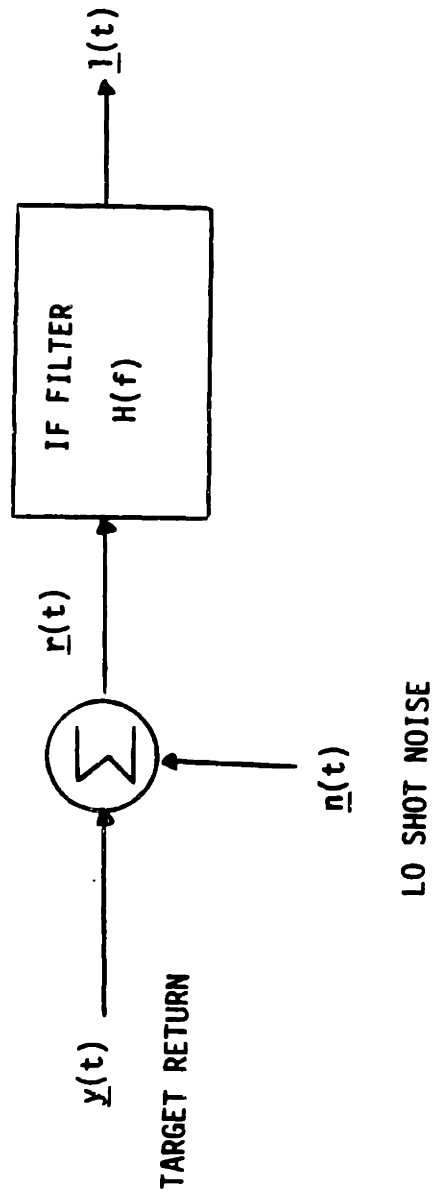
Fig. 2.3. IF Signal Model in the limit of a Strong LO Beam

where $h\nu_0$ is the photon energy at the laser wavelength, and η the quantum efficiency of the photodetector.

The antenna theorem for heterodyne reception [25] allows the overlap integral (2.4.4) to be evaluated at any convenient plane along the path of the optical beam instead of at the photodetector. In typical practice, the LO field backpropagated to the radar entrance pupil obeys the relationship $\underline{U}_{LO}^{O*}(\bar{p}) = \underline{U}_T^C(\bar{p})$. Thus, the antenna theorem along with the reciprocity of free space permit us to express the overlap integral of Eq. (2.4.4) as an integral at the target plane $z=L$ [6]

$$\underline{y}(t) = \int d\bar{p}\ \underline{T}(\bar{p})\ \underline{h}^2(\bar{p})\,\underline{\mathcal{U}}_T^2(\bar{p}/\lambda L,\ t-L/c)$$
$$z=L\quad \cdot\ \underline{s}(t-2L/c)\exp[-j(\Phi(t-2L/c)-\Phi(t))]\ , \qquad (2.4.5)$$

where we have used the far-field approximation. [We will continue to assume in all subsequent analyses that our laser radar system operates in the far-field limit.] In Eq. (2.4.5) $\underline{\mathcal{U}}_T$ is the spatial Fourier transform of $\underline{U}_T$, and we have neglected the radar lag angle.

Up to this point, the radar system model we have developed has not distinguished between conventional angle-angle imagers and our high-resolution imagers. The choices made for the transmitter waveform and the IF filter inject this distinction into the analysis. Thus, in what follows, the IF filter has the dual responsibility of selecting the beat-frequency components in the vicinity of ν_{IF} - for heterodyne detection - and, at the same

time, prcoessing the target return in a coherent manner to
produce high-resolution images. Just how this is done will be
discussed in Chapter III.

CHAPTER III

PERFORMANCE UNDER IDEAL OPERATING CONDITIONS

For angle-angle laser radars, spatial resolution is essentially dictated by the size of the laser beam on the target. Therefore, even though angle-angle laser radars afford spatial resolution quite superior to that of equal-aperture microwave systems, it is clear that for some applications, their diffraction-limited resolution may be inadequate, thus providing the rationale for examining high-resolution imagers such as SAR's and RD radars in the optical and IR frequency regimes. These imagers, under appropriate operating conditions, are capable of spatial resolutions much better than the diffraction-limited resolutions. We shall analyze in this chapter the performance of these optical SAR's and RD radars, assuming ideal operating conditions. The chapter is organized as follows.

The first section (Section 3.1) of this chapter is divided into two parts. In the first part, we focus on the common underlying principle of these high-resolution imagers; the exploitation of a relative motion between the target and the radar that introduces a position-dependent Doppler frequency shift to the target return.

The second part of Section 3.1 introduces basic notations and performance measures which will be used throughout the thesis. Spatial resolution and carrier-to-noise ratio (CNR) are formally defined and interpreted in physical terms.

Signal-to-noise ratio (SNR), a measure of the random fluctuations of the target return strength, is also defined and discussed.

Section 3.2 deals with SAR imaging. First, the one-dimensional (CW) case is discussed, wherein CW transmission is used, i.e., the transmitted waveform employs no temporal modulation. A very simple physical picture is used to illustrate how a drastic improvement in the along-track (azimuth) resolution can be made. The CW SAR analysis is then followed, with minimal amount of modification, by the analysis of the two-dimensional (2D) SAR imaging, where a fine cross-track resolution is achieved via temporal modulation of the transmitted beam.

Section 3.3 examines range-Doppler imaging in two parts. The first part deals with a processor which uses a bank of filters matched to the transmitted waveform. The discussion on the performance of this type of imager is centered around the notion of ambiguity function [1,8], which directly relates the range-delay and Doppler resolutions to the transmitted waveform. The second part involves an analysis of a different type of processor which, by using a train of short pulses, overcomes the tradeoff constraint between the range and Doppler resolutions that is inherent in the first type of processing scheme.

The major novelty of Chapter III, compared to the existing microwave SAR and RD radar theory, is the CNR analysis. Here, we incorporate the effects of LO shot noise and laser speckle into the CNR calculations; the CNR expressions are then interpreted in an intuitively pleasing manner. The performance analysis of this

chapter also serves a useful purpose in that it provides the
basic framework for the analysis of Chapter IV.

3.1. Fundamentals

3.1.1. Underlying Principle of High-Resolution Radars

Whenever there is relative motion between the transmitter
and the receiver, the transmitted signal acquires a Doppler
frequency shift, from the receiver's perspective, that is
proportional to the relative velocity. The same phenomenon
occurs for a radar and a target in relative motion, and provides
the basis for the high-resolution imaging schemes we are about to
discuss.

Let $R(t)$ be the range at time t from the center of the
radar's exit optics to a particular fixed location, in the
target's rest frame, on the target. Then, the Doppler shift
experienced by the return from this target point that is received
at the laser radar is given by

$$\nu_D(t) = -2\dot{R}(t)/\lambda , \qquad\qquad (3.1.1)$$

where $\dot{R}(t)$ is the (time) rate at which the range is changing, and
λ is the laser wavelength.

Suppose now that the Doppler shift $\nu_D(t)$ varies for
different points on the illuminated target. As an example,

consider the configuration for SAR imaging as shown in Fig. 3.1:
a stationary target is located at nominal distance L meters away
from a radar that is translating with respect to the target. Let
the radar's transverse coordinate at time t be $\bar{p}_R(t) = (vt,0)$.
Then, the range from the radar to a point scatterer on the target
located at $\bar{p}_S = (x,y)$ as a function of time is

$$R(t) \simeq L + ((x-vt)^2 + y^2)/2L, \qquad (3.1.2)$$

and the corresponding Doppler shift history is given by

$$\nu_D(\bar{p},t) \simeq 2v(x-vt)/\lambda L \qquad (3.1.3)$$

for $L \gg [(x-vt)^2 + y^2]^{1/2}$. Clearly, the Doppler shift is
position- dependent: it depends on the x-coordinate of the point
scatterer.

Another example of configuration that gives a rise to a
position-dependent Doppler shift is shown in Fig. 3.2. In this
setup - one commonly found in radar astronomy applications of the
range-Doppler radars - the radar is stationary while the target
rotates about some axis (z in the figure) with rotation rate Ω.
When we stare at the figure for a while, it becomes clear that
the locus of points with same y(t) values generate target returns
with same Doppler frequency shift value at time t. [Actually,
the iso-Doppler contours have slight curvatures but in the
far-field limit, the curvatures can be ignored.] Thus, once

⟨ FRONT VIEW ⟩

⟨ SIDE VIEW ⟩
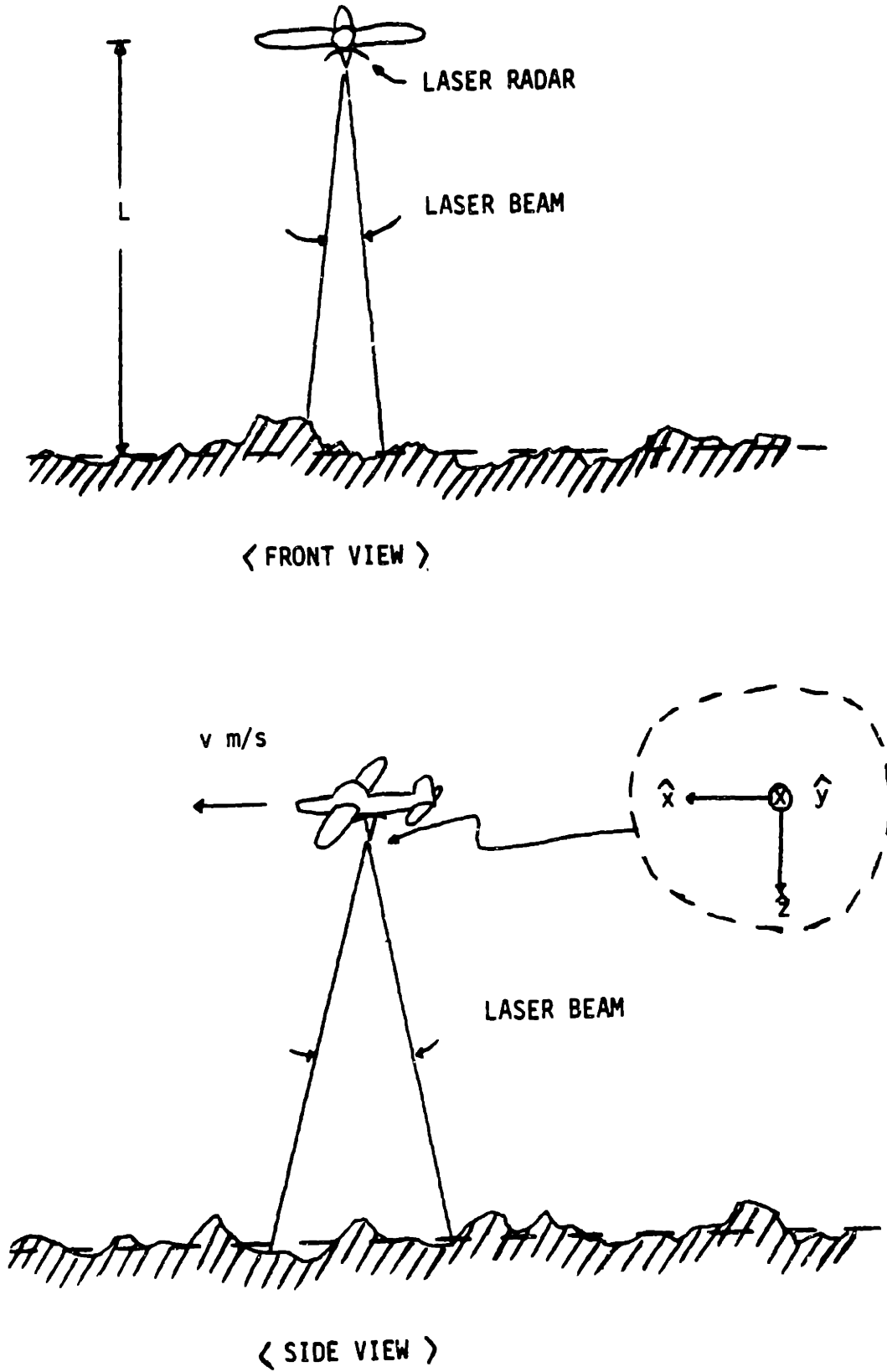
Fig. 3.1   CW SAR Configuration
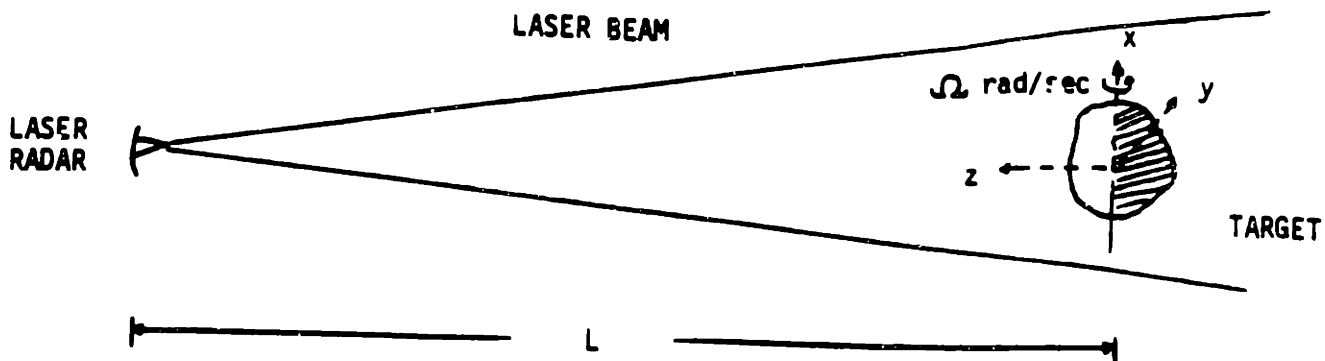
Fig. 3.2 RD Radar Configuration
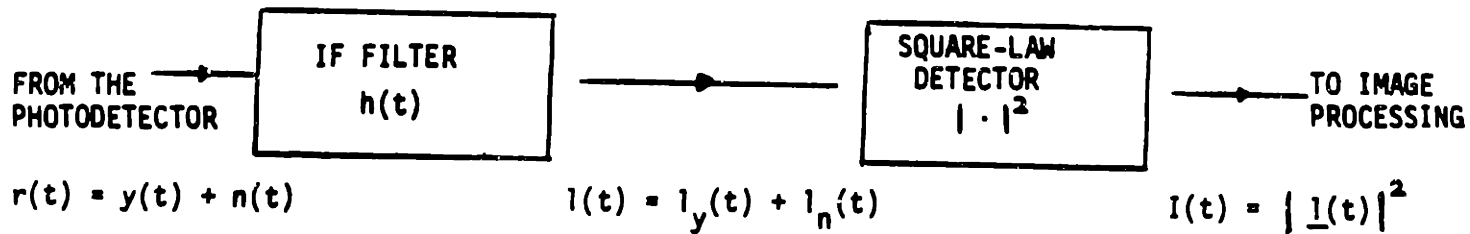
Fig. 3.3 Post-Detection Processor

again, the Doppler shift of the target return varies with the target coordinate.

In both examples just cited, because different portions of the target generate different Doppler shift histories, it is possible to separate out the individual components from the gross target return and identify them with certain parts of the target. This requires some apriori knowledge regarding the target, such as the nominal range to the target, the rotation rate (if any), etc., which may be acquired through alternate modes of operation with the same radar, or some complementary sensor system.

What we just described in the last paragraph is the essence of high-resolution imaging. Just how the process of sorting out various Doppler components is carried out falls under the realm of transmitted waveform and IF filter design. In deciding what the optimal design should be, other performance factors such as the CNR and complexity of the processor must be taken into acount in addition to the spatial resolution. In most cases, the transmitted signal is amplitude and/or frequency-modulated to yield an acceptable range resolution, as the relative motion between the radar and the target helps resolve only the Doppler dimension of the target. [The temporal modulation, on the other hand, helps resolve the dimension orthogonal to the Doppler dimension, i.e., the range dimension.] If there are several locations on the target with same range and Doppler values - as is often the case with some applications of range-Doppler radars - interferometry [21,22] can be used to resolve that ambiguity.

3.1.2. Notations and Performance Measures

Let us look now, in more detail, at the post-photodetection part of the processor in these imagers (see Fig. 3.3). The structure shown in the figure is the prototype that will be used for the most part in this thesis. In some cases, where a bank of filters or a two-stage (cascaded) filter is used, the structure in Fig. 3.3 becomes a module which serves as the basic building block. Thus, it is worthwhile to closely examine the processor. In this section, we will also establish some notations which will be used throughout the thesis, and with these notations, introduce the performance measures we will use to evaluate the imaging systems.

The output of the photodetector, r(t), [which is made up of a target return component y(t) and a LO shot noise component n(t), - cf. (2.4.2)-(2.4.4)] is filtered by a bandpass filter with center frequency ν_{IF}. To be consistent with the earlier notation adopted in Chapter II, we write the impulse response h(t) of this filter in terms its complex envelope as follows:

$$h(t) = \text{Re}\{ \underline{h}(t) \exp[-j2\pi \nu_{IF} t] \}. \tag{3.1.4}$$

Let

$$\underline{l}(t) \equiv \underline{r}(t) * \underline{h}(t)$$

$$= \underline{l}_y(t) + \underline{l}_n(t) \tag{3.1.5}$$

be the complex envelope of the filtered output. We shall be interested in both the component of $\underline{l}(t)$ due to the target return $\underline{y}(t)$, and the component due to the local oscillator shot noise $\underline{n}(t)$; we shall use $\underline{l}_y(t)$ to denote the former, and $\underline{l}_n(t)$ to denote the latter.

The output of the IF filter is typically envelope (linear)-detected or square-law detected. For our purpose, we will adopt the square-law detection scheme, which is mathematically more convenient. Under this scheme, we use the following set of notations for the intensity, i.e., the output of the square-law detector:

$$I(t) \equiv |\underline{l}(t)|^2$$
$$I_y(t) \equiv |\underline{l}_y(t)|^2 \qquad\qquad (3.1.6)$$
$$I_n(t) \equiv |\underline{l}_n(t)|^2.$$

We now set forth the definitions of the performance measures. We will look at the carrier-to-noise ratio (CNR) first.

We define CNR to be

$$CNR \equiv \langle I_y(t) \rangle / \langle I_n(t) \rangle, \qquad\qquad (3.1.7)$$

where the angular brackets $\langle \;\; \rangle$ denote ensemble-averaging over target roughness, shot noise, and any other randomness that may occur. In physical terms, the CNR is the ratio of the average

target return power to the average noise power in the output of the filter $\underline{h}(t)$. It measures, in part, the sensitivity of the imaging system. The average target return intensity $\langle I_y(t) \rangle$ can be written as a target-plane integral in the following form:

$$\langle I_y(t) \rangle = \int d\bar{s} \; \mathcal{J}(\bar{s}) \; g(\bar{s}, t), \qquad (3.1.8)$$

where $\bar{s}$ is the target coordinate, $\mathcal{J}(\bar{s})$ the average target reflectivity of (2.3.2), and $g(\bar{s}, t)$ is a function of finite spatial width that depends on the diffraction-limited beam size, the transmitted waveform, and IF processing. Similarly, the average LO shot noise intensity can also be written as an integral:

$$\langle I_n(t) \rangle = \int_{-\infty}^{\infty} d\tau \; |\underline{h}(\tau)|^2 \; h\nu_0 \, / \, \eta$$
$$= \int_{-\infty}^{\infty} df \; |\underline{H}(f)|^2 \; \hbar\nu_0 \, / \, \eta \, , \qquad (3.1.9)$$

where $h\nu_0 \, / \, \eta$ is the spectral density of $\underline{n}(t)$ (cf. (2.4.4)), and $\underline{H}(f)$ is the Fourier transform of $\underline{h}(t)$.

Spatial resolution is perhaps the most important performance measure of imagers. Given that an imager's task is to map the profile of the average target reflectivity $\mathcal{J}(\bar{s})$, and that only the reflectivities of the area accessed by the sampling function $g(\bar{s}, t)$ of (3.1.8) are represented in the output $\langle I_y(t) \rangle$, it is sensible then to define the spatial resolution in terms of the width of $g(\bar{s}, t)$. Specifically, we define the spatial resolution

to be the full-width between the e^{-1} attentuation points of $g(\bar{s},t)$. For example, if $g(\bar{s},t) = \exp[-(x-vt)^2/a_x^2 -y^2/a_y^2]$, then according to our definition, the x- and y-resolutions are $2a_x$ and $2a_y$, respectively. To put it in simple terms, the spatial resolution cell represents the size of the target area that contributes to the intensity $I_y(t)$ at any given time.

A very prominent problem in any laser radar imaging scenario is laser speckle, which manifests itself as blotches of light and dark spots in the target images, making them far less useful. The seriousness of the problem caused by laser speckle can easily be grasped when we consider the degree of random fluctuation associated with $I_y(t)$. After all, the desired information $\mathcal{T}(\bar{p})$ is embodied in $\langle I_y(t)\rangle$, and if $I_y(t)$ is wildly fluctuating, our estimate of the target's reflecting characteristics will be unreliable even in the absence of LO shot noise. Because the complex envelope $\underline{l}_y(t)$ associated with a rough-surfaced target is a zero-mean circulo-complex Gaussian process, the intensity $I_y(t)$ has exponential statistics [12]. This means that there is a 100 % fluctuation associated with $I_y(t)$ about its mean!

We can measure the reliability of $I_y(t)$ by comparing the signal measure $\langle I_y(t)\rangle$ against the combined speckle and shot noise effects as follows:

$$SNR \equiv (\langle I(t)\rangle - \langle I_n(t)\rangle)^2 / var(I(t)). \qquad (3.1.10)$$

Because $I_n(t)$ also has exponential statistics [6,10] - but for a

different physical reason from $I_y(t)$ - and $\underline{1}_y(t)$ and $\underline{1}_n(t)$ are statistically independent, we have the following expression for SNR [6]:

$$SNR = (CNR/2) \ / \ [1 + CNR/2 + 1/2CNR], \qquad (3.1.11)$$

where CNR is given by (3.1.7). The first term in the denominator of (3.1.11) is due to both the LO shot noise and the target return while the second and the third terms are due to target return and LO shot noise alone, respectively. Note that even when LO shot noise is completely dominated by target return, i.e., CNR --> ∞, the SNR does not exceed unity because of the target speckle.

In angle-angle imaging, a solution to this problem can be found by averaging over several independent frames, thereby reducing the uncertainty regarding the measured intensity [6,16]. In most situations involving high-resolution imaging, however, we are not able to perform that kind of averaging because of the radar and/or target motion. Instead, we must resort to averaging over adjacent pixels. There exist various linear and nonlinear spatial filtering schemes - median filtering and geometric filtering [26-29], for example - which reduce the effect of speckle; however, they invariably do so at the cost of reduced spatial resolution.

At this point, we digress briefly to make a clear distinction between SNR and CNR. As pointed out previously, CNR

defined by (3.1.7) is an indicator of the average strength of the target return component $I_y(t)$, relative to that of the LO shot noise component $I_n(t)$. The SNR, on the other hand, acts as an indicator of how $<I_y(t)>$, the average signal component, fares against the overall fluctuation of the intensity $I(t)$, measured in terms of its variance, $var(I(t))$. Obviously, high CNR and SNR are desirable for a good estimate of $<I_y(t)>$; they would ensure that the output of the square-law detector $I(t)$ is due mostly to the target return, and that its deviation from the mean of the target return component is small.

Having laid down the basis of the high-resolution radars and a set of criteria to measure the performance of those systems, we now proceed to analyze specific types of systems, namely SAR's and RD radars. We start with the SAR's.

3.2. Synthetic Aperture Radar (SAR)

In this section, we present our treatment of optical SAR imaging, assuming that the coherent laser radar that operates under ideal conditions, i.e., without any atmospheric turbulence, transmitter frequency instability, or motion errors. We begin with a very simple, yet physical picture of how such a system can improve the spatial resolution of a conventional laser radar (angle-angle imager) by coherently integrating the target return. We then develop analytical results for the resolution and CNR behavior of such a radar, using the system model established in Chapter II. The first half of the section is devoted to one-dimensional case (CW SAR), in which a CW transmitter is used and only the along-track resolution is improved. The extension to the two-dimensional case (2D SAR) with a modulated transmitted signal is straightforward, and is considered in the second half.

3.2.1. CW SAR

Consider once again the CW SAR configuration shown in Fig. 3.3. A laser radar that is mounted on a vehicle - usually an aircraft - moving with transverse velocity v in the x-direction, observes a stationary, rough-surfaced target at nominal range L. The basic principle of SAR can be understood from the Doppler frequency history of the return from a point scatterer located at (x,y,L). Under this configuration, as pointed out earlier in

Section 3.1.1, the Doppler frequency shift of the return from the point scatterer at time t is given by

$$\nu_D(t) = -2\dot{R}(t)/\lambda$$
$$\simeq 2v(x-vt)/\lambda\, L, \qquad\qquad (3.2.1)$$

where $\dot{R}(t)$ is the rate at which the range is changing. From (3.2.1), we see that the target return from a point scatterer at (x,y,L) has a Doppler history that is a linear function of time with Doppler rate (slope) $\dot{\nu}_D = -2v^2/\lambda\, L$ and zero-intercept at t=x/v. In fact, what we have is a linear frequency-modulated (FM), or equivalently a chirped, signal. This is illustrated in Fig. 3.4. Equation (3.2.1) represents the observed Doppler shift over only the length of time that the point scatterer lies within the transmitter's spatial beam pattern, i.e., only when the scatterer is illuminated. As we shall see shortly, by taking this Doppler history into account, the SAR processor coherently integrates the return over the illumination time, performing basically a pulse-compression operation (usually called focussing or beam-sharpening in the SAR context). The result is a dramatic improvement in the the resolution along the x-direction.

At this point, we should point out that the returns from all scatterers on the target have the same linear FM Doppler history; they are merely time-delayed replicas of one another, the amount of delay depending on their x-coordinates. This means that there need be only one IF filter to process the target return, and the
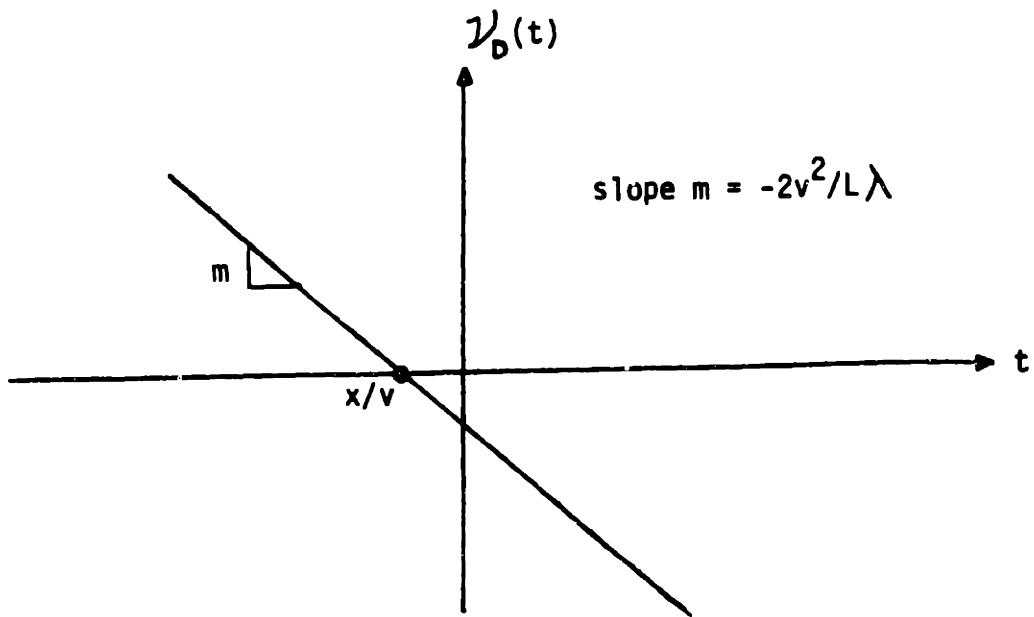
Fig. 3.4 Doppler History of Target Return from a Point Scatterer

reflectivity of a particular region of the target may be inferred by reading the output of the square-law detector at the appropriate time.

Let us now calculate the resolution and the CNR. We will try to optimize these quantities by designing our IF filter to account for the Doppler history of the return.

Assume that the transmitter transmits a CW, collimated elliptical-Gaussian beam:

$$\underline{E}_T(\bar{p},t) = \sqrt{P_T} \; \underline{U}_T^O(x-vt,y), \qquad (3.2.2)$$

where

$$\underline{U}_T^O(\bar{p}) = (2/\pi a_x a_y)^{1/2} \exp[-(x/a_x)^2 - (y/a_y)^2]. \qquad (3.2.3)$$

Here, P_T is the average transmitted power, and a_x, a_y are the transmitted beam's cross-sections along the x- and y-directions, respectively. a_x and a_y are different because, as it will become evident shortly, CW SAR improves only the resolution along the x-direction, and the resolution in the y-direction is simply the beamwidth along the y-direction at the target. Therefore, a_y should be much larger than a_x for the cases of interest here.

With the transmitted field given by (3.2.2), (3.2.3), the IF complex envelope of the target return, denoted by $\underline{y}(t)$, is given by (cf. (2.4.5))

$$\underline{y}(t) = \sqrt{P_T} \int d\bar{p} \ \underline{T}(\bar{p}) \ \underline{U}_L^2(x-vt,y) \ , \qquad (3.2.4)$$

where $\qquad z=L$

$$\underline{U}_L(\bar{p}) = -j(k^2 a_x a_y / 2\pi L^2)^{1/2} \exp[-\alpha L/2] \ \exp[jkL]$$

$$\cdot \exp[jk|\bar{p}|^2/2L - (k/2L)^2((a_x x)^2 + (a_y y)^2)]. \qquad (3.2.5)$$

Having established the structure of the IF signal, there remains the question of how to process this waveform so as to best utilize our knowledge of the Doppler history in improving the along-track resolution.

The simple linear time-dependence of the Doppler history for a point scatterer suggests that we reverse or compensate for this chirp with our processor. This can be accomplished by filtering $\underline{r}(t)$ (= $\underline{y}(t)$ + $\underline{n}(t)$ from Section 2.4) with a bandpass filter whose impulse response has a complex envelope of the form

$$\underline{h}(t) = \exp[-j\pi At^2 - 8(t/T)^2] \ , \qquad (3.2.6)$$

where

A = chirp rate ,

T = impulse response duration.

As a first step, let us see how the resolution and the CNR are affected by the filter parameters A and T.

With the IF filter of the form given in (3.2.6), we find that

$$\underline{1}_y(t) = -\sqrt{P_T}(k^2 a_x a_y/2\pi L^2) \ \underline{C} \ \exp[-\alpha L + j2kL] \qquad (3.2.7)$$

$$\cdot \int d\bar{p} \ \underline{T}(\bar{p}) \exp[jky^2/L - (ka_y y)^2/2L^2 - (t-x/v)^2 \ \underline{M}] \ ,$$

$$<I_y(t)> = P_T(k^2 a_x a_y/2\pi L^2)^2 | \ \underline{C} |^2 \exp[-2\alpha L] \ \lambda^2$$

$$\cdot \int d\bar{p} \ \mathcal{J}(\bar{p}) \exp[-(ka_y y/L)^2 - 2(t-x/v)^2 M'] \ , \qquad (3.2.8)$$

where $\underline{C}$ and $\underline{M}$ are complex-valued constants, and $M'=\text{Re}\{ \underline{M} \}$. The ensemble average $< \ >$ in Eq. (3.2.8) is taken over the target roughness. The expressions for $\underline{C}$ and $\underline{M}$ are as follows:

$$\underline{C} = [\pi \ / \ ((8/T^2 + k^2 a_x^2 v^2/2L^2) + j(\pi A - kv^2/L))]^{1/2} ,$$

and $\qquad\qquad\qquad\qquad\qquad\qquad\qquad\qquad\qquad\qquad (3.2.9)$

$$\underline{M} = [(8/T^2 + j\pi A)(k^2 a_x^2 v^2/2L^2 - jkv^2/L)]$$

$$/[(8/T^2 + k^2 a_x^2 v^2/2L^2) + j(\pi A - kv^2/L)]. \qquad (3.2.10)$$

Putting aside the constants in the front, we recognize the expression $\exp[-(ka_y y/L)^2 - 2(t-x/v)^2 M']$ in Eq. (3.2.8) as the generic function $g(\bar{s},t)$ introduced in Section 3.1.2 (cf. Eq. (3.1.8)), which determines the spatial resolution. Then, according to the definitions we adopted earlier, the along-track and cross-track spatial resolutions (resolutions along the x- and y-directions in our configuration) are given by $v\sqrt{2/M'}$ and $2L/ka_y$, respectively. We will denote these resolutions in the x- and y-directions by x_{res} and y_{res}, respectively. By the way, it is not surprising that the cross-track resolution does not depend on the filter parameters since the target motion is only in the

along-track direction and the IF filter operates only on the time-dependent part of $y(t)$.

Clearly, to optimize x_{res}, we must maximize M' with respect to A, for all T. The optimal value of A - leading to the maximum value of M'- is given by

$$A_{opt} = 2v^2/\lambda L, \qquad (3.2.11)$$

under the conditions

$$ka_x^2/2L \ll 1 , \quad \text{[Fraunhofer approx.]}$$
$$vT \gg 2a_x. \qquad (3.2.12)$$

This choice of A as the optimal value makes perfect physical sense because (3.2.11) corresponds exactly to the Doppler history for a point scatterer derived in (3.2.1), i.e., $A_{opt} = - \dot{v}_D(t)$ of (3.2.1). So, in effect, the filter is eliminating the chirp from the target return.

With this value of A, M' approaches the maximum value $2(v/a_x)^2$ as $T \rightarrow \infty$. Now, we need to consider how the choice of T would affect CNR. And since CNR depends on both $<I_y(t)>$ and $<I_n(t)>$, we need to examine the interplay between them. $<I_n(t)>$ is given by

$$<I_n(t)> = (h v_0 / \eta) T\sqrt{\pi} /4, \qquad (3.2.13)$$

where this time the ensemble average is taken over the shot noise. Note that $\langle I_n(t) \rangle$ is proportional to the impulse response duration T. $\langle I_y(t) \rangle$, on the other hand, is not proportional to T; both M' and $| \underline{c} |^2$ saturate to constant values as T $\longrightarrow \infty$, which in turn leads to the saturation of $\langle I_y(t) \rangle$. This makes physical sense because the target return has a finite bandwidth - roughly equal to the maximum Doppler shift of the illuminated area - and excess bandwidth of the IF filter (on top of the signal bandwidth) cannot increase the amount of energy present at the output of the filter. In view of the behavior of x_{res} and CNR as a function of T (see Fig. 3.5), we choose T = $4L/(ka_x v) = (2 \lambda L/\pi a_x)/v$ as the value which gives us an acceptable performance in terms of the x_{res} and CNR.

Note that our choice of T matches the duration of the illumination interval, i.e., the length of time for which a particular scatterer on the target is illuminated by the moving radar. This is consistent with our intuition that in imaging a particular scatterer, only the portion of the target return containing information about that scatterer should be utilized.

With the "optimal" values of A and T we have chosen, the CW SAR results can be summarized as follows:

$$A = 2v^2/\lambda L, \quad T = 4L/ka_x v, \quad \underline{M} = (v/a_x)^2$$

$$x_{res} = \sqrt{2}\, a_x,$$

$$y_{res} = 2L/ka_y,$$

(3.2.14)
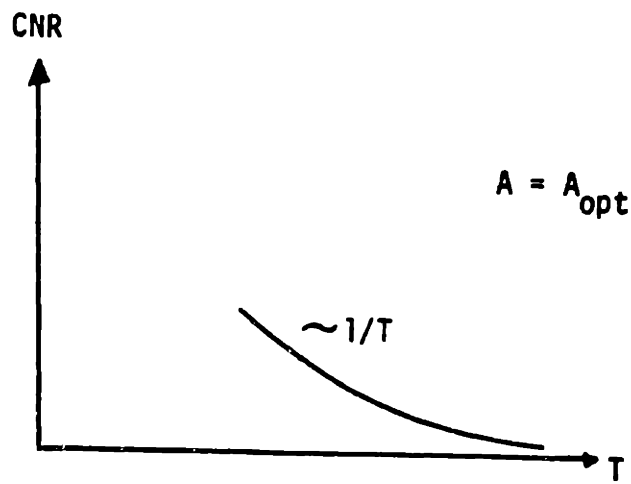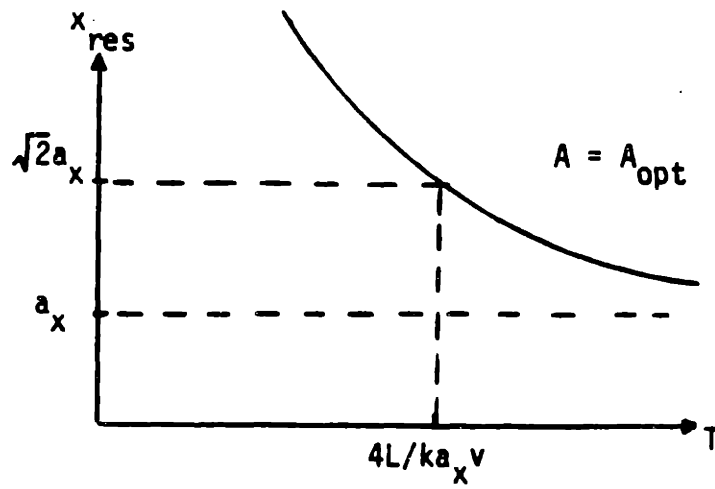
Fig. 3.5   Asymptotic Behavior of x_{res} and CNR

$$\langle I_y(t)\rangle = (\pi P_T a_x a_y \lambda /2\sqrt{2}\ Lv^2)\exp[-2\alpha L]\mathcal{J}_{ave}(vt), \quad (3.2.15)$$

$$\langle I_n(t)\rangle = h\nu_0 \lambda L/(2\sqrt{\pi}\ \eta va_x), \quad (3.2.16)$$

$$CNR(t) = (P_T a_x^2 a_y\ \eta /vL^2 h\nu_0)(\pi/2)^{3/2}$$
$$\cdot \exp[-2\alpha L]\mathcal{J}_{ave}(vt), \quad (3.2.17)$$

where

$$\mathcal{J}_{ave}(x) = (4/\pi x_{res}y_{res})\int d\bar{p}'\ \mathcal{J}(\bar{p}')$$
$$\cdot \exp[-(2(x-x')/x_{res})^2 - (2y'/y_{res})^2]. \quad (3.2.18)$$

$\mathcal{J}_{ave}(x)$ is basically a spatial average of $\mathcal{J}(\bar{p})$ over the region whose size is equal to the area of one resolution cell (x_{res} by y_{res}) and is centered at $(x,0)$.

The results above regarding the spatial resolution and the filter structure are not that different from those of microwave SAR theory [17,18,30-32]. What is new here is the CNR result. We will elaborate on the CNR result in a while.

At this point, let us compare the performance of our CW SAR system with that of a conventional angle-angle imaging system. The most striking thing is that the x_{res} for CW SAR system, $\sqrt{2}\ a_x$, is a quantity independent of all other parameters such as range L, velocity v, etc. More importantly, it is a great improvement over the conventional imager's resolution $2\sqrt{2}\ L/ka_x$ when operating in the far-field regime wherein $ka_x^2/L \ll 1$; this makes SAR's very attractive as high-resolution imagers. The y_{res} of the CW SAR, on the other hand, remains unaffected by the radar's motion and the IF-processing we have just prescribed. Thus, there is no distinction in y_{res} between the angle-angle imager

and the CW SAR. However, as we will see in the next section, y_{res} can be improved by modulating the transmitted signal.

Before we proceed to discuss CNR, we cast (3.2.17) into the standard form [13]:

$$CNR_{CW\ SAR} = (\eta P_T / h \nu_0 B_{CW\ SAR}) \cdot (A_R \varepsilon_{het} \exp[-2\alpha L] \rho / \pi L^2),$$

with
$$(3.2.19)$$

$A_R \varepsilon_{het} = \pi a_x a_y$ = effective heterodyne receiver mixing area,

$\rho \quad = \pi \mathcal{J}_{ave}$ = diffuse reflectivity , $\qquad (3.2.20)$

$B_{CW\ SAR} = (8/\pi)^{1/2}(v/a_x)$ = effective receiver bandwidth.

This bandwidth, $(8/\pi)^{1/2}(v/a_x)$, is comparable to the speckle decorrelation rate for translation found in [15]. Furthermore, note that since

$$TB_{CW\ SAR} = (8/\pi)^{1/2}(4L/ka_x^2) \gg 1, \qquad (3.2.21)$$

because of the far-field assumption, the bandwidth B_{CW-SAR} greatly exceeds 1/T, where T is the dwell time (illumination time). An angle-angle imager with a matched-filter, on the other hand, has a bandwidth B that is comparable to 1/T, the inverse of the dwell time. This difference is due to the fact that the translation-induced Doppler shift of the target return results in a larger bandwidth for the SAR. This means that with all parameters being equal (including the dwell time), a CW SAR

imager allows much more LO shot noise to pass through the IF filter than does an angle-angle imager, and as a result, the CW SAR system has a much lower CNR value than the angle-angle imaging system [In both systems, the target return is assumed to be matched-filtered so that most of the energy present in the target return passes through.] Furthermore, if the two systems were to have same spatial resolution, the angle-angle imager would have even greater advantage in CNR over the CW SAR, as the required increase in a_x for the angle-angle imager would increase the value of $A_R \varepsilon_{het}$, and thus further increase its CNR. In conclusion, the CW SAR gives a much improved along-track resolution over the conventional angle-angle imager but does so at the cost of inferior CNR performance.

Before we finish our analysis, let us compute the correlation functions of $\underline{l}_y(t)$ and $\underline{l}_n(t)$; these results could be used in speckle reduction analysis. With the filter parameters as specified by (3.2.14), we find that

$$< \underline{l}_y(t)\ \underline{l}_y^*(u) > = (\pi P_T a_x a_y\ \lambda /4v^2 L)\ \exp[-2\alpha L]$$
$$\cdot \mathcal{J}_{ave}(v(t+u)/2)\ \exp[-(v/a_x)^2(t-u)^2/2]$$

$$(3.2.22)$$

$$< \underline{l}_n(t)\ \underline{l}_n^*(u) > = (h\nu_0 \lambda L/2\sqrt{\pi}\ \eta\ va_x)\ \exp[-(v/a_x)^2(t-u)^2].$$

$$(3.2.23)$$

So, the speckle decorrelation time   is on the order of a_x/v.

3.2.2. Two-Dimensional (2D) SAR

In this section, we will show how to improve the cross-track resolution by utilizing target range information in a side-looking radar configuration wherein the range to a scatterer depends almost exclusively on its cross-track coordinate. As with the CW SAR analysis, the novelty of this section mainly lies in the derivation and interpretation of the CNR results.

Let us examine the side-looking configuration shown in Fig. 3.6. The radar is moving with velocity v m/s in the x-direction just as it did in the CW configuration. However, rather than looking straight down at the target, the radar now looks down at some angle ψ in order to avoid range ambiguities. L is now the nominal slant range to the center of the illuminated region on the target.

To accomplish the task of improving the cross-track resolution, we will need to (temporally) modulate the transmitted waveform. There are many modulation schemes for a waveform. Nevertheless, there are some common desired properties that a potential transmitted waveform must possess: one, it should be a wideband signal to ensure a good range resolution [8]; and two, it should consist of a periodic train of pulses whose pulse interval is sufficiently large so that the returns from different transmitted pulses do not overlap, eliminating any possible ambiguities. The periodically transmitted pulses serve the dual purposes of sampling the Doppler shift and providing the
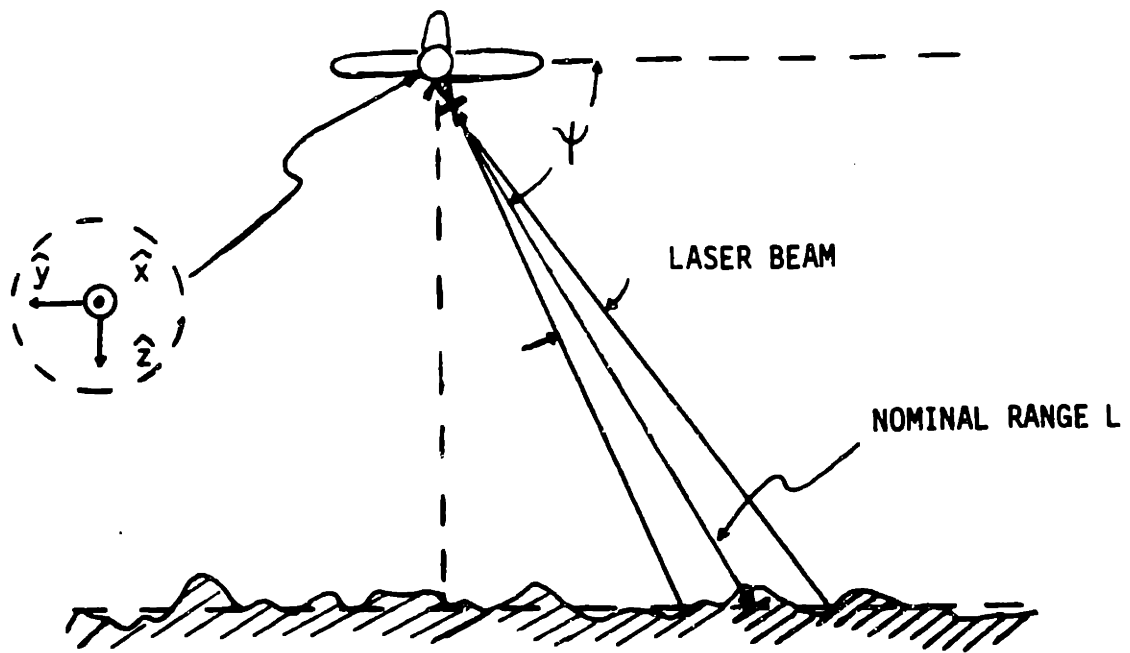
Fig. 3.6 Two-Dimensional SAR Configuration

range-coordinate (cross-track) information.

We shall now demonstrate the basics of 2D SAR imaging in the context of laser radar with a specific waveform. Discussion of the comparative advantages and disadvantages of various waveforms will follow thereafter.

Consider the following waveform comprised of chirped Gaussian pulse:

$$\underline{s}(t) = \sqrt{P_T} \sum_{m=-\infty}^{\infty} \underline{f}(t - mT_s + 2L/c) , \qquad (3.2.24)$$

where

$$\underline{f}(t) = \exp[-j\pi W_o t^2/T_o - 4t^2/T_o^2] , \qquad (3.2.25)$$

with

T_s = period of the pulse train ,

T_o = pulse duration

(fullwidth between e^{-2} points of $| \underline{f}(t)|^2$),

W_o = chirp bandwidth.

We will assume that $W_o T_o \gg 1$, i.e., the chirp bandwidth is much greater than the inverse of the pulse duration, and that $T_s \gg T_o$. This waveform, with proper choices of T_o, T_s and W_o, satisfies the aforementioned requirements for $\underline{s}(t)$. Moreover, it gives a certain symmetry between the Doppler and the range resolutions, as will be seen shortly. Finally, by setting $W_o = 0$ in the final results, we can obtain the corresponding results for a train of Gaussian pulses without any frequency modulation.

Assuming the same transmitted beam pattern $\underline{u}_T^o(\bar{p})$ as in the

CW case (cf. Eq. (3.2.3)), and the train of chirped-Gaussian pulses given by Eqs. (3.2.24) and (3.2.25) for $\underline{s}(t)$, we can write the complex envelope of the target return as follows:

$$\underline{y}(t) = \sum_{m=-\infty}^{\infty} \underline{Y}_m(t) , \qquad (3.2.26)$$

where

$$\underline{Y}_m(t) \equiv \underline{B} \int d\bar{p}\, \underline{T}(\bar{p}) \exp[j2ky\cos\psi + jk(y\sin\psi)^2/L$$
$$- (ka_\perp y\sin\psi/L)^2/2]\, \underline{f}(t - mT_s - 2y\cos\psi/c)$$
$$\cdot \exp[(jk/L - (ka_x/L)^2/2)(x-vt)^2] , \qquad (3.2.27)$$

with

$$\underline{B} \equiv \sqrt{P_T}(k^2 a_\perp a_x \sqrt{\sin\psi}/2\pi L^2)\, \exp[j2kL - \alpha L],$$

$$a_x, a_\perp = \text{cross-sections of the transmitted beam.}$$

a_y of the CW SAR has been replaced by $a_\perp$ because of the change in radar configuration. Note also that a geometric factor $\sqrt{\sin\psi}$ has been added to $\underline{T}(\bar{p})$ – and absorbed by $\underline{B}$ – so that the total scattered power by the target surface remains the same, independent of the look-down angle ψ . This modification is a necessary consequence of our target-interaction modelling which assumes that the target scatters the incoming coherent light evenly into the entire upper hemisphere regardless of ψ .

If we assume that the sum of the pulse duration T_o and the spread of range-delays of the returns from the illuminated target region is less than the interpulse interval T_s, then $\underline{Y}_m(t)$, the return due to the mth transmitted pulse, does not overlap in time with $\underline{Y}_{m'}(t)$ for $m \neq m'$. This means that at any given time t, the

target return $\underline{y}(t)$ is primarily associated with a single transmitted pulse (see Fig. 3.7a). Thus, $\underline{y}(t)$ can be divided into segments of equal length T_s, each segment consisting essentially of the return from a single pulse, and recorded in a two-dimensional format as shown in Fig. 3.7b. In this storage format, $\underline{y}(t)$ is represented by $\underline{y}(m,\tau)$, where m is used to index a particular time interval or, equivalently, the segment of the return associated with a particular transmitted pulse, and τ indicates time with respect to the center of that segment. That is

$$\underline{y}(m,\tau) = \underline{y}(mT_s+\tau)$$
$$\simeq \underline{Y}_m(mT_s+\tau), \qquad (3.2.28)$$

$$-T_s/2 \leq \tau \leq T_s/2.$$

Thus far, we have ignored the presence of the LO shot noise. In reality, however, we would be dealing with the sum of the target return and the shot noise: $\underline{r}(m,\tau)$ $(= \underline{y}(m,\tau) + \underline{n}(m,\tau))$, where $\underline{r}(m,\tau)$ and $\underline{n}(m,\tau)$ are defined in the same manner as $\underline{y}(m,\tau)$.

Because $\underline{n}(t)$ was previously modelled as a white noise with spectral density $h\nu_0/\eta$, its 2D representation $\underline{n}(m,\tau)$ is a 2D white noise with the following statistics:

$$< \underline{n}(m,\tau) \, \underline{n}^*(m',\tau') > = (h\nu_0 / \eta)\delta_{mm'}\delta(\tau-\tau'), \qquad (3.2.29)$$

$\underline{y}(t)$

$\underline{y}_m(t)$, RETURN DUE TO THE mTH TRANSMITTED PULSE

$(m-2)T_s$ $(m-1)T_s$ mT_s $(m+1)T_s$ $(m+2)T_s$

t
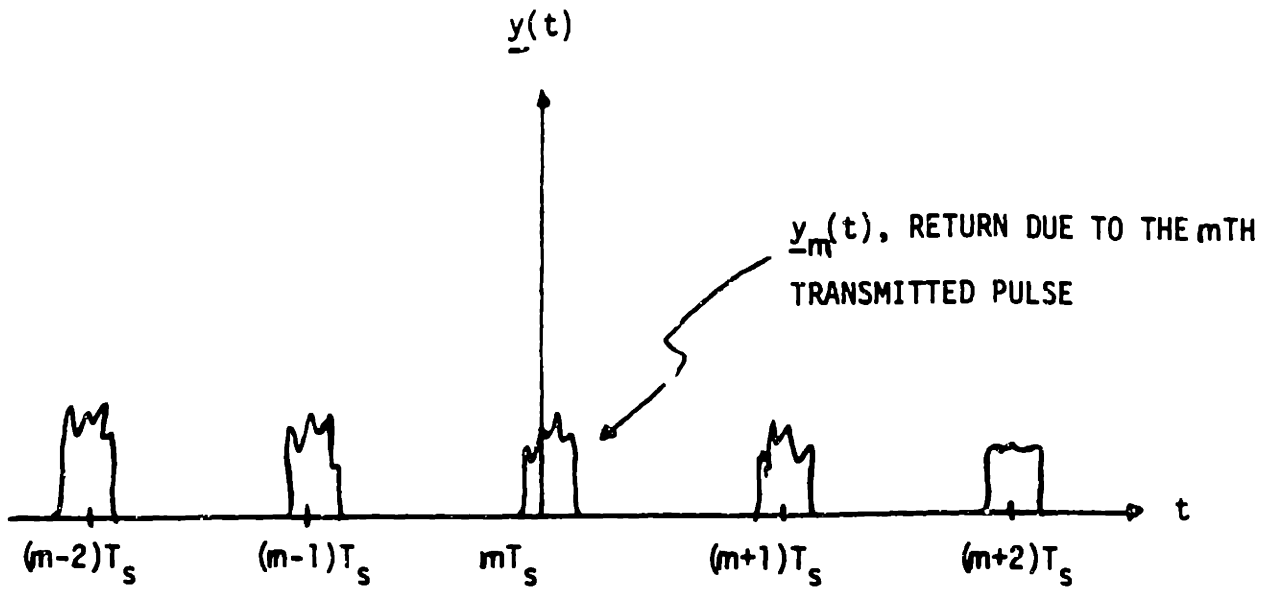
Fig. 3.7a   Target Return Associated with a Pulse Train

$\cdots$ m+2 m+1 m m-1 m-2 $\cdots$ $\longleftarrow$ n

$\tau = -T_s/2$

$\downarrow \tau$

$\cdots$ $\cdots$

$\tau = T_s/2$

RECORDING OF $\underline{y}(m,\tau)$, $\underline{y}(t)$ FOR

$mT_s - T_s/2 \leq t \leq mT_s + T_s/2$
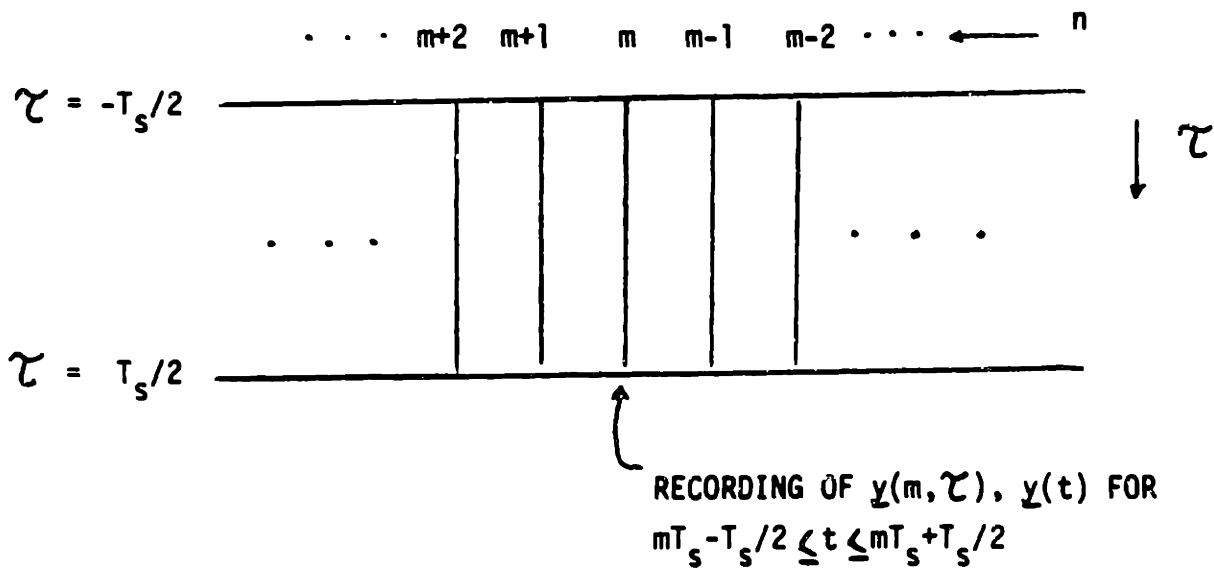
Fig. 3.7b   Two-Dimensional Storage Format

where $\delta_{mm'}$ is a Kronecker delta.

As mentioned at the beginning of this section, by transmitting pulses at a sufficiently high rate, we are in effect periodically sampling the Doppler shift due to the radar motion, and at the same time, using the individual pulses to obtain the range information. It is evident then that m and τ are the natural coordinates for carrying out these operations.

Once cast in the 2D format, the IF signal $\underline{r}(m,\tau)$ is then passed through a cascaded two-stage filter: a discrete-time filter $\underline{h}_1[m]$ followed by a continuous-time filter $\underline{h}_2(\tau)$ (see Fig. 3.8). The output of the two-stage filter $\underline{l}(m,\tau)$ is given by

$$\underline{l}(m,\tau) = (\ \underline{r}(m,\tau)\ \underset{\infty}{\circledast}\ \underline{h}_1[m]\ )\ *\ \underline{h}_2(\tau)$$
$$= \int_{-T_s/2}^{T_s/2} d\tau'\ [\ \sum_{m=-\infty}^{\infty} \underline{h}_1[m-m']\ \underline{r}(m',\tau')]\ \underline{h}_2(\tau - \tau'). \quad (3.2.30)$$

From the CW SAR analysis, it is clear that the optimal $\underline{h}_1[m]$ should be the discrete-time version of the filter $\underline{h}(t)$ given by Eqs. (3.2.6) and (3.2.14). For the continuous-time filter $\underline{h}_2(\tau)$, we also choose a matched-filter, $\underline{h}_2(\tau) = \underline{f}^*(-\tau)$, to perform the pulse compression. Thus, the processor for (3.2.30) uses

$$\underline{h}_1[m] = \exp[-(jk/L)(vmT_s)^2 - (ka_x/L)^2(vmT_s)^2/2]\ , \quad (3.2.31)$$

and

$$\underline{h}_2(\tau) = \exp[+j\pi W_o\tau^2/T_o - 4\tau^2/T_o^2]. \quad (3.2.32)$$
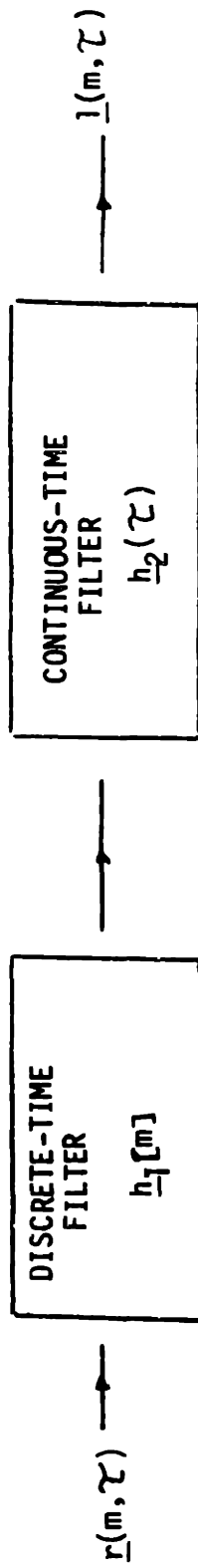
Fig. 3.8 2D SAR's Two-Stage Filter

The target return component of the discrete-time filter's output, denoted by $\underline{z}(m,\tau')$, is given by

$$\underline{z}(m,\tau') = (P_T/\pi)^{1/2}(ka_\perp \sqrt{\sin\psi}\,/2Lv T_s)\,\exp[j2kL-\alpha L]$$

$$\cdot\int d\bar{p}\;\underline{T}(\bar{p})\exp[j2ky\cos\psi\,+\,jk(y\sin\psi\,)^2/L$$

$$-(ka_\perp y\sin\psi\,/L)^2/2]\;\underline{f}(\tau'\,-\,2y\cos\psi\,/c) \qquad (3.2.33)$$

$$\cdot\exp[-j\alpha_1(m^2\,-\,\tilde{x}{}^2)]\;\exp[-\alpha_2(\tilde{x}\,-\,m)^2/2]$$

$$\cdot\sum_{l=-\infty}^{\infty}\{\exp[-(2\alpha_1(\tilde{x}\,-\,m)\,+\,2\pi l)^2/8\alpha_2]$$

$$\exp[-\,j((\tilde{x}\,+\,m)/2)(2\alpha_1(\tilde{x}\,-\,m)\,+\,2\pi l)]\}\;,$$

where

$$\tilde{x}\,-\,m \equiv (x\,-\,v(mT_s+\tau'))/vT_s\;,$$

$$\alpha_1 \equiv k(vT_s)^2/L\;,$$

$$\alpha_2 \equiv (ka_x vT_s)^2/2L^2$$

$$[\;\alpha_1 \gg \alpha_2 \text{ by far-field approximation}].$$

The effect of periodic sampling is evident in the summation term of (3.2.33), which has periodic peaks. It follows that $\underline{z}(m,\tau')$ receives contributions from all the scatterers in the vicinity of $x = v(mT_s+\tau') - \lambda\,lL/2vT_s$, $l = 0, \pm 1, \pm 2,\ldots$. [Of course, those contributions are weighted by $\exp[-\alpha_2(\tilde{x}\,-\,m)^2/2]$, the beam pattern on the target.] Since the purpose of the discrete-time filter is to select only the narrow strip centered at $x = mvT_s$, we want to avoid this type of aliasing, i.e., we want only one of those periodic peaks to be within the illuminated target region. This constraint provides a lower limit on the pulse-repetition-frequency (PRF) $1/T_s$. [The upper limit on PRF is set by the

range-delay spread of the illuminated target]. A quick calculation reveals that the condition for ensuring no aliasing is:

$$a_x \gtrsim vT_s \; . \tag{3.2.34}$$

This simply states that we need to transmit at least one pulse during the time it takes the radar to cover the distance a_x. Upon recognizing v/a_x as the speckle decorrelation rate found earlier, this statement can also be interpreted as the Nyquist sampling theorem in the spatial domain: the sampling rate $1/vT_s$ should exceed the spatial bandwidth of the speckle $1/a_x$. In this section, we will assume that aliasing does not occur.

Provided that there is no aliasing, i.e., the PRF is sufficiently high, only the $l = 0$ term remains from the summation in (3.2.33); it is approximately equal to

$$\exp[-(x-v(mT_s+ \tau'))^2/a_x^2], \tag{3.2.35}$$

which is identical to the CW SAR result. Now carrying out the continuous-time filtering, we obtain the following approximate result from Eq. (3.2.33) and the assumption $T_s \gg T_o$:

$$\underline{l}_y(m,\tau) = \underline{D} \int d\bar{p}\; \underline{T}(\bar{p}) \exp[j2ky\cos\psi + jk(y\sin\psi)^2/L$$
$$- (ka_\perp y\sin\psi/L)^2/2)]\; Q(x,y,m,\tau) \; , \tag{3.2.36}$$

where

$$\underline{D} \equiv (P_T/32)^{1/2}(ka_\perp\sqrt{\sin\psi}\ T_0/LvT_s)\ \exp[j2kL - \alpha L] \qquad (3.2.37)$$

$$Q(x,y,m,\tau) \equiv \exp[-(x-v(mT_s+\tau))^2(1/a_x^2 + (ka_x/2L)^2)]$$
$$\cdot\exp[-((\pi W_0)^2 + (4/T_0)^2)\ (\cos\psi\ /c)^2$$
$$\cdot(y-c\tau/2\cos\psi)^2/2]\ , \qquad (3.2.38)$$

We are now ready to compute the signal and noise components of the average intensity, $\langle I_y(m,\tau)\rangle\ (= \langle|\ \underline{1}_y(m,\tau)|^2\rangle)$ and $\langle I_n(m,\tau)\rangle\ (= \langle|\ \underline{1}_n(m,\tau)|^2\rangle)$, which are needed to evaluate the spatial resolution and CNR of the 2D SAR. From (3.2.36)-(3.2.38) we find that

$$\langle I_y(m,\tau)\rangle = |\ \underline{D}|^2\lambda^2\ \exp[-(b_1b_2/(b_1 + b_2))\cdot(c\tau/2\cos\psi)^2]$$
$$\cdot\int d\bar{p}\ \mathcal{J}(\bar{p})\exp[-2(x-v(mT_s+\tau))^2(1/a_x^2 + (ka_x/2L)^2)]$$
$$\cdot\exp[-(b_1+b_2)(y - (b_2/(b_1+b_2))\cdot(c\tau/2\cos\psi))^2]$$

$$(3.2.39)$$

and

$$\langle I_n(m,\tau)\rangle = (h\nu_0\ \lambda\ LT_0)\ /\ (2^{5/2}\ \eta\ a_xvT_s)\ , \qquad (3.2.40)$$

where

$$b_1 \equiv (ka_\perp\sin\psi\ /L)^2$$
$$b_2 \equiv [(\pi W_0)^2 + (4/T_0)^2](\cos\psi\ /c)^2 \qquad (3.2.41)$$
$$|\ \underline{D}|^2 = (P_T/32)(ka_\perp T_0/LvT_s)^2\sin\psi\ \exp[-2\alpha L].$$

From (3.2.39), we see that the along-track resolution x_{res} is still $\sqrt{2}\ a_x$ and has not changed from the CW SAR case. This is not surprising since no change has been made - except that the Doppler shift is now sampled instead of being measured

continuously - in the way the Doppler information is processed. The cross-track resolution, denoted by y_{res}, is given by

$$y_{res} = 2 \cdot [(ka_{\perp} \sin \psi/L)^2 + (\cos \psi/c)^2 ((\pi W_o)^2 + (4/T_o)^2)]^{-1/2}$$

$$\simeq (2c/\cos \psi)/[(\pi W_o)^2 + (4/T_o)^2]^{1/2}$$

[for a large on-target beam size]   (3.2.42)

$$(= 2c/(\pi W_o \cos \psi) \text{ since } W_o T_o >> 1 \text{ assumed})$$

Since W_o is the bandwidth of the transmitted waveform, the last result states the well-known fact: the range resolution improves with the bandwidth. Thus, in general, a marked improvement in the cross-track resolution can be achieved over the CW SAR case by having a large modulation bandwidth or a very short pulse. As a side note, the processed signal has a τ-duration of $\Delta \tau = (\cos \psi/c)\sqrt{(b_1+b_2)/b_1 b_2}$, where b_1 and b_2 are given by (3.2.39).

. If we assume that the average reflectivity $\mathcal{J}(\bar{p})$ is approximately constant over a resolution cell (x_{res} by y_{res}) and that y_{res} is much less than the range spread (beamwidth) $L/ka_{\perp} \sin \psi$, we can write CNR as

$$CNR_{2D \ SAR}(m,\tau) = \mathcal{J}(vmT_s, c\tau/2\cos \psi) \exp[-2aL](P_T \eta/h\nu_o)$$
$$\cdot (a_{\perp}^2 a_x^2 \pi^2 c T_o) \sin \psi \qquad (3.2.43)$$
$$\cdot \exp[-((ka_{\perp} \sin \psi/L)(c\tau/2\cos\psi))^2]$$
$$/(2L^3 W_o[1 + (4/\pi W_o T_o)^2]^{1/2} vT_s \lambda \cos \psi).$$

The expression for $CNR_{2D\ SAR}$ above may be cast into the standard form of Eq. (3.2.19) as follows:

$$CNR_{2D\ SAR}(m,\tau) = (\eta\ P_T/h\nu_0\ B_{2D\ SAR})$$
$$\cdot (A_R\varepsilon_{het}exp[-2\alpha L]\ \rho(m,\tau)/\pi L^2) \qquad (3.2.44)$$
$$\cdot \varepsilon_{range}exp[-((ka_\perp sin\psi/L)\cdot(c\tau/2cos\psi))^2],$$

where

$$A_R\varepsilon_{het} = \pi a_x a_\perp$$
$$= \text{effective heterodyne receiver mixing area,}$$

$$\rho(m,\tau) = \pi\ \mathcal{J}(vmT_s,\ c\tau/2cos\psi)$$
$$= \text{diffuse reflectivity}$$

$$B_{2D\ SAR} = B_1 B_2$$
$$= \text{two-dimensional bandwidth of the receiver,}$$

$$B_1 = (v/a_x)/(\pi/T_s)$$
$$= \text{normalized bandwidth of the discrete-time}$$
$$\text{filter } \underline{h}_1[m],$$

$$B_2 = \pi W_0[1 + (4/\pi W_0 T_0)^2]^{1/2} \simeq \pi W_0$$
$$= \text{bandwidth of the continuous-time filter } \underline{h}_2(\tau),$$

$$\varepsilon_{range} = \text{loss factor due to the range-delay spread}$$
$$\text{of the target}$$
$$= T_0\ /\ (2^\lambda Lcot\psi\ /\pi ca_\perp)$$

There are three noteworthy differences between this result and the result previously obtained for CW SAR: emergence of the range-delay spread loss factor ε_{range}; replacement of $B_{CW\ SAR}$ by $B_{2D\ SAR}$; and finally, presence of the last exponential factor in

(3.2.44).

The loss factor ε_{range} is simply the ratio of the transmitted pulse duration over the processed (filtered) signal's duration [which may be taken as the range-delay spread for the case we are considering]. Physically, the loss factor arises because the total energy in each return pulse - obtained by integrating the power carried by the target return over one period T_s - is independent of the range spread. This implies that $CNR_{2D\ SAR}$, representing the instantaneous power of the filtered target return, should decrease with increasing range-delay spread (the return pulse gets stretched out in time) to keep the energy constant. For CW SAR, where, instead of pulses, a CW signal is transmitted, there is a constant average power level for both the transmitted signal and the target return. Hence, $CNR_{CW\ SAR}$ has no ε_{range} factor.

$B_{2D\ SAR}$, the bandwidth, or more appropriately "bandarea" of the two-stage filter for the 2D SAR receiver, is a product of two bandwidths; the bandwidth for the discrete-time filter $\underline{h}_1[m]$ and the bandwidth for the continuous-time filter $\underline{h}_2(\tau)$. $B_{2D\ SAR}$ times the spectral density $h\nu_0/\eta$ (cf. (3.2.29)) gives the amount of noise power present at the output of the 2D filter.

The exponential factor $\exp[-((ka_\perp \sin\psi /L)(c\tau/2\cos\psi))^2]$ stems from the beam pattern of the illumination falling on the target. In other words, it is the relative intensity of the illumination at $y = c\tau/2\cos\psi$. This factor did not appear in the CW SAR result because there was no temporal modulation. With

CW SAR, the receiver effectively performs a spatial integration over the entire illuminated area in the cross-track direction.

Having stated the major differences between the results for 2D SAR and 1D (CW) SAR, we now turn our attention to the connection between $\underline{s}(t)$ and the system performance in the 2D SA.: case. The expressions for the cross-track resolution and the CNR bear out the important roles played by the pulse duration and bandwidth of $\underline{f}(t)$. The cross-track resolution improves with increasing bandwidth of $\underline{f}(t)$ whereas the CNR behaves in the opposite manner. We also note that an increase of pulse duration T_O leads to an increase in CNR, which is not surprising because a longer pulse means more energy in the target return [in fact, $P_T(T_O/T_S)$ is the (time-) average transmitted power]. These observations suggest that an ideal waveform, from performance point of view, should have a large bandwidth and a long pulse duration, i.e., a large time-bandwidth product (TBP).

Our analysis is general enough to allow, if one wishes to do so, a discussion on the relative advantages and disadvantages of using frequency modulation (as opposed to using shorter, unmodulated pulses) to achieve a high resolution in the cross-track direction. To provide a fair basis for a comparison, we shall pit the result for a train of chirped Gaussian pulses against that for a train of unmodulated Gaussian pulses. The peformance in the first case is given by Eqs. (3.2.42) and (3.2.43) while the performance in the second case - obtained simply by letting $W_O = 0$ in (3.2.42) and (3.2.43) - is given

below:

$$Y_{res} = cT_o/2\cos\psi \quad . \tag{3.2.45}$$

$$CNR_{2D\ SAR}(m,\tau) = \mathcal{J}(vmT_s, c\tau/2\cos\psi)\ \exp[-2\alpha L](P_T\ \eta\ /h\ \nu_o)$$
$$\cdot(a_\perp^2 a_\chi^2 \pi^2 cT_o)\ \sin\psi$$
$$\cdot\exp[-((ka_\perp\sin\psi\ /L)(c\tau/2\cos\psi))^2]$$
$$/(2L^3(4/\pi T_o)vT_s\lambda\ \cos\psi\ ). \tag{3.2.46}$$

[Of course, the numerical values of T_o may be quite different for the two cases.]

As an example of comparison between a system using FM pulses and a system using much shorter, unmodulated pulses, suppose we want those two systems to have roughly the same cross-track resolution (bandwidth) and CNR. This requires the latter system to provide a much higher peak power (P_T) to compensate for the short duration of its pulses, which may cause a problem since there is a limit on how large P_T can be.

Clearly, we need to consider several factors - resolution, CNR, and (peak and average) power constraints of the system, just to name a few - before judging which modulation format is suitable for the application on hand.

3.3. <u>Range-Doppler (RD) Radar</u>

In Section 3.2, we analyzed a SAR system which forms a high-resolution image of a spatially-resolved planar target. In this section, we present the performance analysis of range-Doppler radars. In particular, we examine the issues involving imaging of a rotating object. As with the SAR results, the major novelty here is the CNR analysis of RD radars in the optical context.

Section 3.3 is organized as follows. We start by describing some of the fundamental differences between RD imaging and SAR imaging, and go on to provide the necessary groundwork for the remainder of the section which is divided into two parts. The first part deals with a processing scheme that uses a collection of bandpass filters matched to the transmitted waveform. Spatial resolution and CNR are derived and discussed in terms of ambiguity function. The second part is devoted to a different type of processing scheme involving periodic transmission of wideband pulses. This scheme, which is similar to the 2D SAR imaging in many respects, eliminates to a large extent the need to compromise between a good range resolution and a good Doppler resolution that is normally associated with the first type of processing.

Although SAR and RD imaging utilize the same underlying physical principle examined in Section 3.1.1, in many respects

range-Doppler imaging is quite different from SAR imaging. This is because the former exploits relative motion between the target and the radar that is due to target motion (in our case target rotation), whereas the latter depends on relative motion provided by radar translation. There exist three major problems we face in imaging a rotating target. They are: one, changes in the reflecting strength of a particular region because of the change in the orientation of the region with respect to the incident beam; two, movement of the region itself during imaging (due to rotation), which can cause blurring of the target image [see, for example, [18-20], for details on the motion-through-resolution-cell problem]; and three, different parts of the target having different Doppler histories.

The first two problems mentioned above necessitate having a relatively short coherent integration time while the third problem rules out the possibility of processing the target return with a single filter, as done in the CW SAR case.

Consider the configuration of Fig. 3.2, in which the target is rotating about the x-axis at a nominal distance L away from the stationary radar. In what follows within this section, we will drop, without any loss of generality, the beam-intensity pattern on the target. Physically, this corresponds to having a uniform illumination power-density on the target, i.e., the target is spatially unresolved. Then, the IF complex envelope of the target return component is (cf. Eq. (3.2.4))

$$\underline{y}(t) = (-k^2 a_x a_y/2\pi L^2)\exp[-\alpha L] \int_\Sigma d\bar{s}_o \, \underline{T}(x_o, y(t), z(t))$$

$$\cdot \exp[j2k(L-z(t))] \, \exp[jk(y^2(t)+x_o^2)/L]$$

$$\cdot \sqrt{P_T} \, \underline{s}_n(t-2(L-z(t))/c) \quad , \tag{3.3.1}$$

where

$$z(t) = z_o\cos(\Omega t) + y_o\sin(\Omega t) \quad ,$$

$$y(t) = -z_o\sin(\Omega t) + y_o\cos(\Omega t) \quad ,$$

$$\underline{s}_n(t) = \text{normalized transmitted waveform}$$

$$[\, \underline{s}(t) = \sqrt{P_T} \, \underline{s}_n(t) \,].$$

In (3.3.1), Σ denotes the illuminated region of the target, and the subscript o denotes the target's coordinate at time $t = 0$. We have assumed that the transmitted beam is still the elliptical-Gaussian beam of (3.2.3) and that the target rotates slowly with rate Ω. The complex reflection coefficient $\underline{T}(x_o, y(t), z(t))$ now embodies the scattering statistics - at time t - of the region whose coordinates at time $t = 0$ are (x_o, y_o, z_o).

An iso-range contour on the target is given by the locus of points equidistant from the transmitter. The equation governing the iso-range contour is

$$(L-z(t)) + (y^2(t) + x_o^2)/2L = R. \tag{3.3.2}$$

By the same token, an iso-Doppler contour on the target is given by the locus of points with equal Doppler shift values; it obeys the equation

$$2\Omega y(t)[1 + z(t)/L]/ \lambda = v_D \ ,$$
(3.3.3)

In both equations, the second term arises from the finite curvature of the incident wavefront, and is quite small compared to the first term. Thus, it will be neglected in our analysis.

For a short time interval t such that $\Omega t \ll 1$, we can make the following approximations that basically amount to linearizing the point scatterers' trajectories.

$$z(t) \simeq z_0 + (\Omega t)y_0 \ ,$$
$$y(t) \simeq y_0 - (\Omega t)z_0 \ ,$$
$$y^2(t) \simeq y_0^2 - 2(\Omega t)z_0 y_0 .$$
(3.3.4)

This implies that the Doppler shift associated with a particular point scatterer is nearly constant over the coherent integration time. It follows that, for a small enough t, the z_0- and y_0- planes constitute iso-range and iso-Doppler planes, respectively, and through range-Doppler processing, z_0 (range)- and y_0 (cross-range) -coordinates of a scatterer can be resolved within reasonable accuracy. However, there is almost a complete ambiguity in the x-direction: x_0 does not enter into either the range or Doppler shift calculations, except through the curvature of the incident wavefront, which is a very weak effect. Therefore, some apriori knowledge of the object's shape is essential in pairing range-Doppler components of the target return with the corresponding parts of the target. In some

cases, a target may have more than one location with an identical set of range and Doppler values, in which case an interferometric technique may be used to separate the contributions from these range-Doppler degenerate locations [21,22]. We now proceed to discuss the specifics of how to resolve various range-Doppler components.

3.3.1. RD Radar: Processor A

One way to sort out different Doppler components is to use a bank of bandpass filters instead of a single IF filter (see Fig. 3.9). [For off-line processing, serial operation with one frequency-agile bandpass filter suffices.] Each filter is matched to the transmitted waveform which may consist of a single pulse or a train of pulses, and has a center frequency which is shifted from ν_{IF} by its own characteristic parameter ν_D'.

$$\underline{h}(t; \nu_D') = \underline{s}_n^*(-t)\exp[-j2\pi\nu_D't] \ . \tag{3.3.5}$$

So, the output of a filter with parameter value ν_D' at time t is comprised of components with Doppler shift and range-delay values in the vicinity of ν_D' and t, respectively.

We now compute the average intensity of the target return component. The target return contribution to the complex envelope and the average intensity of the filtered output are:

$$\underline{l}_y(t; \nu_D') = \underline{y}(t) * \underline{h}(t; \nu_D') \ \text{ and } \ <I_y(t; \nu_D')> = <| \ \underline{l}_y(t; \nu_D'')|^2>,$$
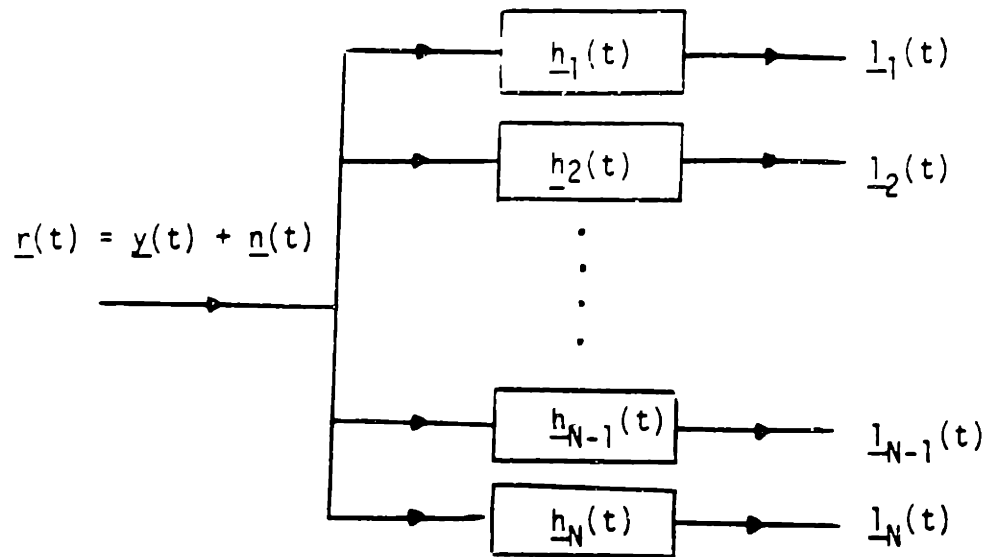
$$\underline{h}_i(t) = \underline{s}_n^*(-t) \, \exp(-j2\pi \nu_{D_i}' t)$$

$\underline{l}_i(t)$: CONTAINS INFORMATION ABOUT THE TARGET REGION WITH DOPPLER VALUE ν_{D_i}' (ISO-DOPPLER CONTOUR). t INDEXES THE RANGE-DELAY.

Fig. 3.9 A RD Processor Utilizing a Bank of Matched-Filters
(Type A)

respectively, where ν_D' is the parameter value of the filter. Calculations yield

$$
\begin{aligned}
\underline{1}_y(t; \nu_D') = (-k^2 a_x a_y/2\pi L^2)\sqrt{P_T} \; & \exp[-\alpha L] \int d\bar{s}_o \; \underline{T}(x_o, y_o, z_o) \\
& \cdot \exp[j2k(L-z_o)] \; \exp[jk(y_o^2 + x_o^2)/L] \\
& \cdot \underline{X}(z_o, Y_o, t; \nu_D'),
\end{aligned} \tag{3.3.6}
$$

$$
\begin{aligned}
<I_y(t; \nu_D')> = (-k^2 a_x a_y/2\pi L^2)^2 P_T \; \lambda^2 \exp[-2\alpha L] & \tag{3.3.7} \\
\cdot \int d\bar{s}_o \; \mathcal{J}(x_o, y_o, z_o) \; | \; \underline{X}(z_o, Y_o, t; \nu_D') \; |^2, &
\end{aligned}
$$

where

$$
\begin{aligned}
\underline{X}(z_o, Y_o, t; \nu_D') \equiv \{ \int_{-\infty}^{\infty} du \; \underline{s}_n^*(u+\tau) \; \underline{s}_n(u) \; \exp[-j2\pi u \, \Delta\nu_D] \} \\
\exp[-j2\pi\nu_D' t - j2\pi\Delta\nu_D \cdot 2(L-z_o)/c] \;,
\end{aligned}
$$

$$
\begin{aligned}
\nu_D & \equiv 2\Omega y_o / \lambda \;, \\
\Delta\nu_D & \equiv \nu_D - \nu_D' \;, \tag{3.3.8} \\
\tau & \equiv 2(L-z_o)/c - t.
\end{aligned}
$$

In deriving the above equations, we have employed the quasi-static approximation given by (3.3.4).

We introduce one more notation which will be useful for future discussions.

$$
\begin{aligned}
T(\tau, \Delta\nu_D) & \equiv | \; \underline{X}(z_o, Y_o, t; \nu_D') \; |^2/| \; \underline{X}_o \; |^2 \\
& = | \; \underline{X}(\tau, \Delta\nu_D) \; |^2/| \; \underline{X}_o \; |^2, \tag{3.3.9}
\end{aligned}
$$

where

$$
\begin{aligned}
| \; \underline{X}_o \; |^2 & \equiv | \; \underline{X}_\infty(\tau=0, \Delta\nu_D=0) \; |^2 \\
& = | \int_{-\infty}^{\infty} du \; | \; \underline{s}_n(u) \; |^2 |^2. \tag{3.3.10}
\end{aligned}
$$

$T(\tau, \Delta\nu_D)$, **which has a peak value of one at (0,0), is the ambiguity function of** $\underline{s}_n(t)$ **(see [1,8]). The notion of ambiguity function usually appears in the parameter - range, Doppler - estimation and target detection analysis. Here, it determines the spatial resolution of target images. In fact,** $T(\tau, \Delta\nu_D)$ **is essentially the envelope function** $g(\bar{s},t)$ **of (3.1.8).**

We define the range-delay and Doppler resolutions, denoted by τ_{res} and $\Delta\nu_{res}$, respectively, to be the fullwidths between the e^{-1} attenuation points of the ambiguity function along the τ and $\Delta\nu_D$ axes. They are given by the following equations:

$$T(\tau_{res}/2, 0) = |\int_{-\infty}^{\infty} du \; \underline{s}_n^*(u+\tau_{res}/2) \; \underline{s}_n(u)|^2 / |\underline{X}_0|^2$$
$$= e^{-1}, \tag{3.3.11}$$

and

$$T(0, \Delta\nu_{res}/2) = |\int_{-\infty}^{\infty} du \; |\underline{s}_n(u)|^2 \; \exp[-j2\pi u(\Delta\nu_{res}/2)]|^2$$
$$/ |\underline{X}_0|^2$$
$$= e^{-1}. \tag{3.3.12}$$

Furthermore, via relation (3.3.8), the cross-range resolution y_{res} and range resolution z_{res} are related to $\Delta\nu_{res}$ and τ_{res} by

$$y_{res} = \lambda \; \Delta\nu_{res}/2\Omega$$
$$z_{res} = c\tau_{res}/2. \tag{3.3.13}$$

From examining (3.3.12), it is clear that a long waveform duration is desired for a good Doppler resolution as $\Delta\nu_{res}$ is

inversely proportional to the pulse duration, whereas a waveform with large bandwidth is needed for a good range resolution [since τ_{res} is inversely proportional to the bandwidth]. The second point is made more obvious by rewriting (3.3.11) in terms of $S_n(f)$, the Fourier transform of $\underline{s}_n(t)$, as follows:

$$T(\tau_{res}/2,0) = |\int_{-\infty}^{\infty} df \ |S_n(f)|^2 \ \exp[-j2\pi f(\tau_{res}/2)]|^2 \ / \ | \ \underline{x}_o |^2$$
$$= e^{-1}. \qquad (3.3.14)$$

At this point, we should be aware that, despite our first inclination to think otherwise, the preceding range-delay and Doppler resolutions alone do not fully represent the overall spatial resolution of RD images in some cases. A well-known property of ambiguity functions, often called "volume-invariance property" [8], states that

$$\int_{-\infty}^{\infty}\int_{-\infty}^{\infty} d\Delta\nu_D \ d\tau \quad T(\tau, \Delta\nu_D) = 1, \qquad (3.3.15)$$

for all waveforms. Since τ and $\Delta\nu_D$ are tied directly to z_o and y_o, the volume-invariance property implies that when the target dimensions are sufficiently large, the effective area of the target contributing to the output of the filter remains the same, regardless of the waveform being used. This means that if some waveforms have better range-delay and Doppler resolutions (as defined earlier) than others, they inevitably suffer from having subsidiary peaks (ripples), etc.

As an example, let us consider the chirped Gaussian pulse of (3.2.25):

$$\underline{s}_n(t) = \exp[-j\pi W_o t^2/T_o - 4t^2/T_o^2].$$

The corresponding ambiguity function is

$$T(\tau, \Delta\nu_D) = \exp[-(\pi/2)^2(W_o\tau - T_o \Delta\nu_D)^2 - 4(\tau/T_o)^2].$$

$$(3.3.16)$$

In this instance, because of the coupling between τ and $\Delta\nu_D$ in the ambiguity function, its e^{-1}-contour in the $\tau - \Delta\nu_D$ plane is a tilted ellipse which is very much lopsided (see Fig. 3.10). Thus, y_{res} and z_{res} alone give a distorted picture of the true resolution cell in the sense that they represent only a small portion of the area enclosed by the e^{-1}-ellipse; furthermore, they give a false impression that the resolution cell is a rectangular grid instead of an ellipse as shown by the e^{-1}-contour.

Although we have worked out only one explicit example here, it is clear that under the present processing scheme we cannot have arbitrarily fine Doppler and range-delay resolutions at the same time in the true sense because of the volume-invariance property of ambiguity functions. This is in stark contrast to the 2D SAR case. In the 2D SAR case, under proper conditions, the along-track resolution depends only on the beam dimension a_x while the cross-track resolution is determined mainly by the
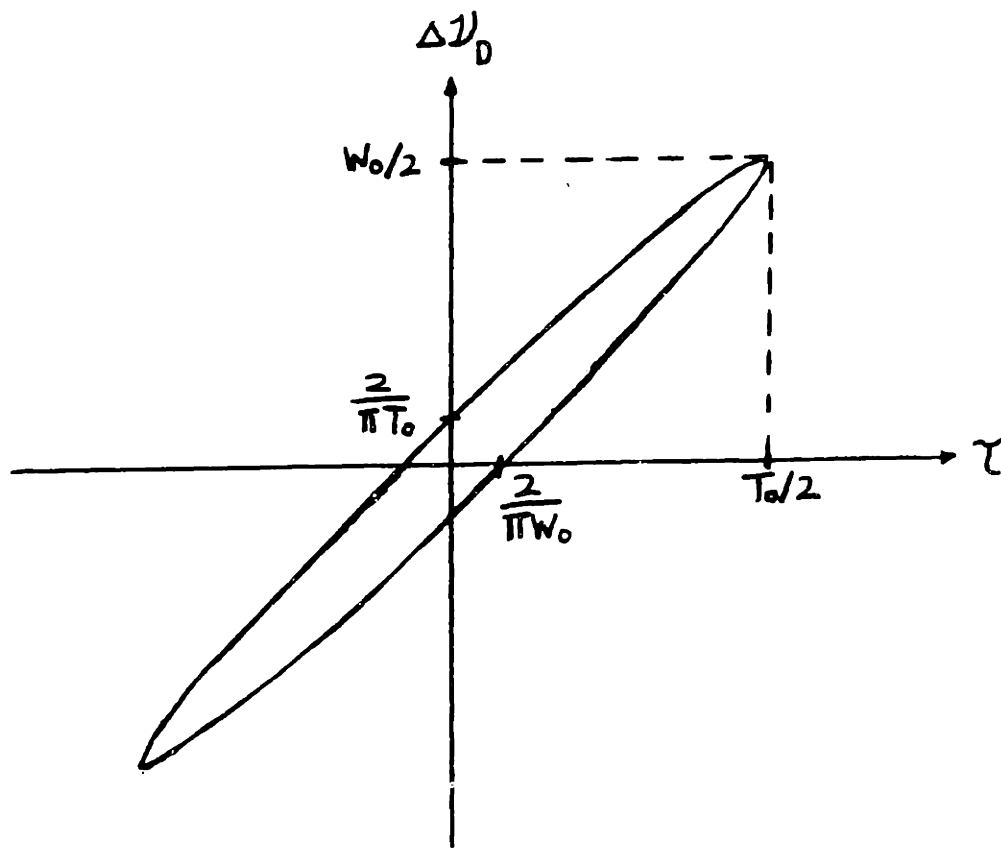
Fig. 3.10 e^{-1} Contour of the Ambiguity Function
for a Chirped-Gaussian Pulse

transmitted waveform's bandwidth; thus, there is no coupling or tradeoff between the two resolutions. This deficiency in our present processing scheme can be remedied, to a large extent, by periodically transmitting wideband pulses, much like in the 2D SAR case. We will discuss this in more detail later.

We now turn our attention to the issue of CNR. First, we need to compute $< I_n(t; \nu_D') >$. From (3.3.5) and (3.3.10), we have

$$
\begin{aligned}
< I_n(t; \nu_D') > &= (h \; \nu_0/ \eta) \int_{-\infty}^{\infty} du \; | \underline{s}_n(u) |^2 \\
&= (h \; \nu_0/ \eta) \; | \underline{X}_0 |.
\end{aligned}
\tag{3.3.17}
$$

Combining Eqs. (3.3.7), (3.3.9), and (3.3.17), we obtain the CNR as follows:

$$
\begin{aligned}
\text{CNR} \; (t; \nu_D') &= (P_T \; \eta /h\nu_0)(k^2 a_x a_y/2\pi L^2)^2 \; \lambda^2 \; \exp[-2\alpha L] \\
&\quad \cdot | \; \underline{X}_0 \; | \int d\bar{s}_0 \; \mathcal{J}(\bar{s}_0) \; T \; (\tau, \Delta\nu_D)
\end{aligned}
\tag{3.3.18}
$$

It is evident from (3.3.18) that CNR is directly proportional to the transmitted waveform's duration ($| \underline{X}_0 |$), a result not unexpected since a longer waveform duration has more energy in its target return. As with 2D SAR, one consideration we need to take into account when choosing a waveform is the peak power constraint of the laser; if the peak power is not sufficiently high, it may be necessary to transmit a longer waveform to achieve the desired CNR value.

For a sufficiently large target, i.e., a target whose range and Doppler dimensions greatly exceed the e^{-1}-contour of the ambiguity function, the above expression for CNR may be rewritten as follows by using (3.3.8) and (3.3.15):

$$CNR(t; \nu_D') \simeq (P_T \eta /h\nu_0)(k^2 a_x a_y /2\pi L^2)^2 \lambda^2 \exp[-2\alpha L] \mid \underline{X}_0 \mid$$
$$\cdot (c\lambda /\Omega) \, \mathcal{J}_{ave}(t; \nu_D') \, , \qquad (3.3.19)$$

where $\mathcal{J}_{ave}(t; \nu_D')$ is the spatial average of $\mathcal{J}$ in the vicinity of $(y_0, z_0) = (\lambda \nu_D' /2\Omega, L-ct/2)$.

3.3.2. RD Radar: Processor B

In Section 3.3.1, we found out that processing the target return with IF filters whose impulse responses match - within some offset frequencies - the entire transmitted waveform poses a contraint on the range-delay and Doppler resolutions. In this section, we explore a processing scheme that removes this constraint. This scheme involves transmitting a series of wideband pulses and processing the return in two sequential steps, in a manner analogous to the 2D SAR processing, and is commonly used with most microwave RD radars [19-21].

Let us start with the transmitter. The transmitter transmits a series of pulses, usually wideband, for a finite period of time.

$$\underline{s}_n(t) = \sum_{m=-(N-1)/2}^{(N-1)/2} \underline{f}(t - mT_s + 2L/c),$$

where (3.3.20)

$\underline{s}_n(t)$ = normalized transmitted waveform

$\underline{f}(t)$ = individual pulse

T_s = interpulse period,

Thus, the overall waveform duration is approximately NT_s ($\equiv T_N$) for a large N. As with 2D SAR, duration of the individual pulses and the interpulse period T_s should be chosen to ensure that there is no overlap between returns associated with different transmitted pulses. Under this condition, the return at any

given time can be regarded as coming from a single transmitted pulse, and the return can be stored in the two-dimensional storage format introduced in Section 3.2.2 (see Fig. 3.7). The target return due to the mth transmitted pulse can then be written as follows:

$$\underline{y}(m,\tau) = -\sqrt{P_T}(k^2 a_x a_y/2\pi L^2) \exp[-\alpha L] \int d\bar{s}_o \ \underline{T}(x_o, y_o, z_o)$$
$$\cdot \exp[2jk(L-z_o)] \ \exp[jk(y_o^2 + x_o^2)/L] \qquad (3.3.21)$$
$$\cdot \exp[-j2\pi \ \nu_D(mT_s+\tau)] \ \underline{f}(\tau + 2z_o/c) \ ,$$

where

$$\nu_D \ \equiv \ 2\Omega y_o/\lambda$$
$$= \text{Doppler shift associated with } y_o,$$

$2z_o/c$ = range-delay associated with z_o,

$-T_s/2 \le \tau \le T_s/2$.

The quasistatic approximation of Section 3.3.1 has been used in (3.3.21).

The sum of target return and LO shot noise components stored in the 2D format is then processed in two sequential steps as follows. First, the return associated with each transmitted pulse is passed through a continuous-time matched-filter of impulse response $\underline{f}^*(-t)$. Then a discrete-time Fourier-transform (DTFT) operation is performed on the matched-filter output sequence (see Fig. 3.11). [In real applications, a discrete Fourier transform (DFT) would be used instead of DTFT]

Several remarks are in order at this juncture. The matched-

filter in the Fig. 3.11 architecture is matched to a single pulse $\underline{f}(t)$ rather than the entire waveform $\underline{s}_n(t)$, as was the case in the earlier scheme. Thus, unlike what transpires in the earlier scheme where separation of various Doppler and range components is done simultaneously (via ambiguity function), here it is done sequentially: first the range-coordinate is resolved via the CT filtering and then the Doppler-coordinate is resolved via the DTFT operation. Moreover, because the continuous-time (CT) matched filter and DTFT are linear operations, the order in which they are performed may be interchanged. So we can construct an equivalent alternative architecture of Fig. 3.11 in which the Doppler coordinate is resolved before the range coordinate.

We should also comment on the differences between the this RD processing and the 2D SAR processing. The first obvious difference is that the coherent summation for the former (DTFT) has to be performed over a finite duration because of the time constraint on the transmitted waveform, whereas for the latter there is no such constraint. The second difference is in the type of coherent summation performed: whereas the DTFT operation constitutes the second step of the RD processing, a 2D SAR's second processing step involves a discrete-time filtering with a chirped Gaussian. This difference is due to the different ways the target/radar motion affect the target return in each case. The SAR configuration produces target return - for a point scatterer - whose Gaussian amplitude time dependence derives from the Gaussian beam pattern on the target, and whose linear Doppler

$\underline{r}(m,\tau) \rightarrow$ | CONTINUOUS-TIME FILTER $\underline{h}(\tau) = f^*(-\tau)$ | $\rightarrow$ | DISCRETE-TIME FOURIER TRANSFORM (DTFT) | $\rightarrow \left\{ \underline{\ell}(\nu_D',\tau) \right\}$
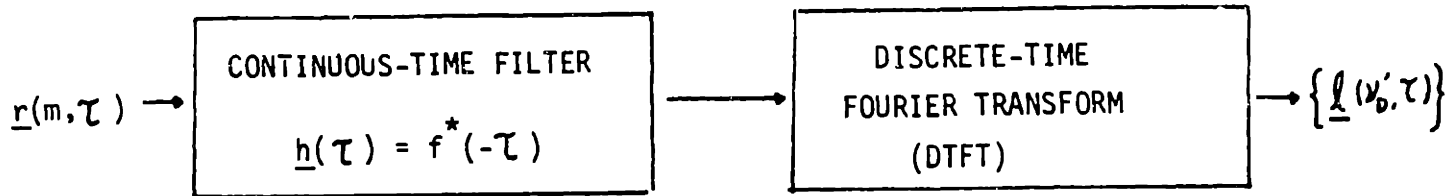
Fig. 3.11   A RD Processor Utilizing a Matched-Filter
and a Discrete-Time Fourier Transformer (Type B)

$4/\pi NT_S$

$\nu_D'- 2/T_S$ $\nu_D'- 1/T_S$ ν_D' $\nu_D'+ 1/T_S$ ν_D

(q = -2)   (q = -1)   (q = 0)   (q = 1) $(= 2\Omega y_0/\lambda)$
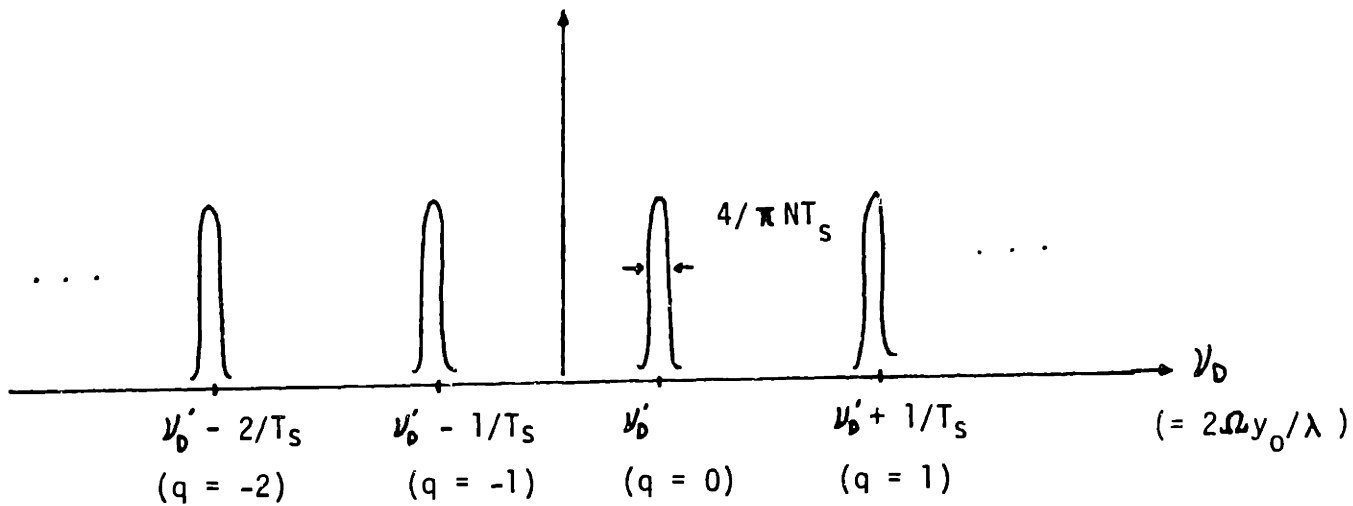
Fig. 3.12   DTFT Output As a Function of Target Coordinate y_0
for a Fixed Frequency ν_D'

shift time dependence is due to the translational motion of the radar. On the other hand, the target return from a point scatterer in our RD configuration has no amplitude variation with time - because the target is assumed to be spatially unresolved - and it has a constant Doppler shift on the time scale we are working with.

One final note, before fleshing out analysis of Fig. 3.11 architecture. It should be clear that unless the amplitudes of the transmitted pulses are tapered over the transmission time T_N, the Fourier transform operation will produce undesirable ripples (sidelobes) in the frequency domain because of the sudden termination of the target return after N pulses. This ill effect can be reduced at the cost of adding another processing step and a degradation of main-lobe Doppler resolution, by tapering the target return's strength over N pulses. This technique can be applied either to the amplitude of transmitted pulses themselves or to the target return output sequence from the matched-filter. In the analysis to follow, we will apply a Gaussian taper to the return that matches the transmission time T_N.

Let us now compute the target return and shot noise components of the output intensity. By applying the Gaussian taper $\exp[-8(m/N)^2]$, we can approximate $\underline{y}(t)$ by

$$\underline{y}(t) \simeq \sum_{m=-\infty}^{\infty} \underline{y}(m,\tau),$$

where

$$\underline{y}(m,\tau) \simeq -\sqrt{P_T}(k^2 a_x a_y/2\pi L^2)\exp[-\alpha L]\int d\bar{s}_o \ \underline{T}(x_o,y_o,z_o)$$

(3.3.22)

$$\cdot \exp[2jk(L-z_0)] \ \exp[jk(y_0^2 + x_0^2)/L]$$

$$\cdot \exp[-j2\pi \nu_D (mT_s+\tau)] \ \underline{f}(\tau + 2z_0/c)$$

$$\cdot \exp[-8(m/N)^2].$$

It then follows that

$$< I_y(\nu_D' ,\tau) > \equiv < \left| \underline{1}_y(\nu_D' ,\tau) \right|^2 > \quad \text{(cf. Fig. 3.11)}$$

$$= P_T(k^2 a_x a_y/2\pi L^2)^2 \exp[-2\alpha L]$$

$$\cdot \lambda^2 \int d\bar{s}_0 \ \mathcal{J}(x_0,y_0,z_0) \qquad (3.3.23)$$

$$\cdot (\pi N^2/8) \ \left| \sum_{q=-\infty}^{\infty} \exp[-N^2(2\pi(\nu_D - \nu_D')T_s - 2\pi q)^2/32] \right|^2$$

$$\cdot \left| \int_{-\infty}^{\infty} d\tau' \ \underline{f}(\tau'+ 2z_0/c) \ \underline{f}^*(\tau'-\tau)\exp[-j2\pi\nu_D \ \tau'] \right|^2,$$

where

$$\nu_D = 2\Omega Y_0/ \lambda$$

$$\nu_D' = \text{Fourier transform variable.}$$

The τ'-integral is the result of CT filtering and the q-summation is the result of DTFT. We will examine the τ'-integral first.

The τ'-integral is nothing more than a scaled ambiguity function of individual pulses, i.e., of $\underline{f}(t)$. Thus, the range-delay resolution in this processing scheme is determined by the bandwidth of $\underline{f}(t)$. However, because the pulses tend to be very short, the Doppler resolution based on the ambiguity function is quite poor; as will be seen shortly, overall Doppler resolution is determined by the total transmission time T_N instead.

Whereas range resolution is related to the τ'-integral, Doppler resolution is derived from the q-summation. The terms

inside the summation have been sketched in Fig. 3.12 as a function of the Doppler shift $\nu_D = 2\Omega y_o/\lambda$ for a particular Fourier transform frequency ν_D'. Two things are noteworthy about this figure. One of them is that the width of the lobes in Fig. 3.12 is $4/\pi NT_s$ ($= 4/\pi T_N$), and thus clearly much narrower than the Doppler resolution based on the τ'-integral alone. As a result, the overall Doppler resolution $\Delta\nu_{res}$ is $4/\pi NT_s$; it improves with the total waveform duration.

The other interesting point about the Fig. 3.12 is that, as in the 2D SAR case earlier, aliasing could be a problem; thus, we need a sufficiently high PRF so that there is contribution from only one part of the target (one lobe in Fig. 3.12). As the target is spatially unresolved in our RD configuration, it is not the diffraction-limited beam size that places an upper bound on the number of lobes included in the output - as in the SAR case - but rather the size of the target itself. The requirement on the PRF to avoid aliasing is then $1/T_s$ needs to be at least twice the Doppler bandwidth (bandwidth due to target rotation) which we may take to be roughly $\Omega D_y/\lambda$, where D_y is the target dimension in the y-direction and Ω is the rotating target's angular velocity. One important consideration from a practical standpoint is that the Doppler bandwidth from a rotating target could be significantly greater than the translation-induced Doppler bandwith under equivalent conditions. As a result, the RD radars may place a tougher requirement on their transmitter lasers than the SAR's in terms of the required PRF's.

In summarizing our results thus far, we have shown that with the two-step processing it is possible to obtain good range-delay and Doppler resolutions without encountering the tradeoff problem seen in the previous RD processing scheme. In other words, the range-delay and Doppler resolutions become decoupled in our present scheme.

Let us now compute $< I_n(v_D', \tau) >$ ($= < | \underline{1}_n(v_D', \tau)|^2 >$). Using the statistics given by (3.2.29) for $\underline{n}(m,\tau)$, we easily obtain:

$$
\begin{aligned}
< I_n(v_D', \tau) > &= (h v_0 / \eta)(\int_{-\infty}^{\infty} d\tau' | \underline{f}(\tau')|^2)(\sum_{m=-\infty}^{\infty} \exp[-16(m/N)^2]); \\
&= (h v_0 / \eta)(\sqrt{\pi} N/4)(\int_{-\infty}^{\infty} d\tau' | \underline{f}(\tau')|^2).
\end{aligned}
$$

$$(3.3.24)$$

We will now let $\underline{f}(t)$ be a chirped Gaussian pulse given by (3.2.25) and compute the system performance that goes with it. If we assume that there is no aliasing so that only the $q = 0$ term in the q-summation contributes (cf. (3.3.23), $< \bar{I}_y(v_D', \tau) >$ becomes

$$
\begin{aligned}
< I_y(v_D', \tau) > = &\; P_T(k^2 a_x a_y / 2\pi L^2)^2 \exp[-2aL] \\
&\cdot \lambda^2 \int d\bar{s}_0 \; \mathcal{J}(x_0, y_0, z_0) \qquad (3.3.25) \\
&\cdot (\pi N^2/8) \exp[-(2\pi(v_D - v_D')NT_s)^2/16] \\
&\cdot (\pi T_0^2/8) \exp[-(\tau + 2z_0/c)^2((\pi W_0/2)^2 + (2/T_0)^2)]
\end{aligned}
$$

and $< I_n(\nu_D' , \tau) >$ becomes

$$< I_n(\nu_D' , \tau) > = (h\nu_0 / \eta)(\pi NT_0/8\sqrt{2}) . \qquad (3.3.26)$$

The corresponding y- and z-resolutions are

$$Y_{res} = 2 \lambda /\pi\Omega NT_s , \qquad (3.3.27)$$

$$Z_{res} = (2c/\pi W_0)/[1 + (4/\pi W_0 T_0)^2]^{1/2}$$

$$\simeq 2c/\pi W_0 , \qquad \text{for } W_0 T_0 >> 1. \qquad (3.3.28)$$

Advantages of laser radars - over microwave radars - stemming from their short wavelengths and their ability to generate wideband pulses are evident in the Y_{res} and Z_{res} expressions above. Finally, the CNR is

$$CNR(\nu_D' , \tau) = (P_T \eta /h \nu_0)(k^2 a_x a_y/2\pi L^2)^2 \lambda^2 \exp[-2\alpha L](\sqrt{2} \, \pi NT_0/8)$$

$$\cdot \int d\bar{s}_0 \, \mathcal{J}(x_0,y_0,z_0) \quad \exp[-(2\pi(\nu_D - \nu_D')NT_s)^2/16]$$

$$\cdot \exp[-(\tau+2z_0/c)^2((\pi W_0/2)^2 + (2/T_0)^2)] ,$$

$$(3.3.29)$$

which, for Y_{res} and Z_{res} much less than the target dimensions, reduces to

$$CNR(\nu_D' , \tau) \simeq (P_T \eta /h\nu_0)(k^2 a_x a_y/2\pi L^2)^2 \lambda^2 \exp[-2\alpha L](\sqrt{2} \, \pi NT_0/8)$$

$$\cdot \mathcal{J}_{ave}(\nu_D' , \tau) \, (c \lambda /\Omega) /((\pi W_0 NT_s)[1+(4/\pi W_0 T_0)^2]^{1/2})$$

$$(3.3.30)$$

where $\mathcal{J}_{ave}(\nu_D , \tau)$ is the spatial average of $\mathcal{J}$ in the target area accessed by (ν_D' , τ).

CHAPTER IV

PERFORMANCE UNDER NONIDEAL OPERATING CONDITIONS

To this point, we have analyzed the performance of high-resolution laser radars, assuming that the imaging is to be performed in an ideal environment. That is to say, we have assumed that: there is no atmospheric turbulence; the transmitter laser produces a beam without random frequency instability; and the radar and target trajectories do not deviate from their nominal courses. Therefore, the performance level found in Chapter III represents the upper bound on the performance that can be achieved.

Of course, in a real operating environment, we cannot expect such benign conditions: the carrier frequency of the laser will tend to wander around the desired value, due to thermal fluctuations within the laser, structural vibrations, etc.; the temperature gradients in the atmosphere will give a rise to (atmospheric) turbulence; and there will be random motions involving the target and radar-carrying vehicle. These, which represent some of the most serious problems we face, will degrade the system performance of high-resolution imagers to varying degrees.

The problems of frequency instability, atmospheric turbulence, and target/radar platform motions also impact microwave high-resolution systems. However, they are potentially much more damaging to the optical and infrared systems because of

the shorter wavelenths involved. Moreover, it is not immediately obvious whether the detrimental effects brought on by the aforementioned perturbations are enough to negate the advantages gained from combining the features of angle-angle laser radars with those of high-resolution microwave radars.

It is the goal of this chapter to quantify the effects of these non-idealities on the system performance. In that regard, we are especially interested in examining the effect on spatial resolution, since these high-resolution imagers need temporal coherence of the target return over the coherent processing time to achieve fine resolutions and these perturbations disrupt the coherence of the return. In addition, we will also examine their effect on CNR.

Some work has been done in the past [17,33,34] on analyzing the effects of phase errors on the performance of high-resolution microwave radars, primarily with SAR's. However, they have largely been limited to either deterministic error analysis for very specific cases or random phase error analysis with mathematically intractable end results [making it necessary to resort to numerical methods to obtain useful results]. More importantly, there was no direct link to the actual physical processes responsible for the phase errors in these analyses. As a result, there has been a lack of physical insight in regards to how a particular type of random error degrades high-resolution radar's system performance.

There also have been some studies on the effects of

atmospheric turbulence on microwave SAR's [35,36], but their scope has been quite limited. And to our understanding, there has not been any analytical work on the effects of either the random transmitter aim error or the target/radar platform vibrations on SAR or RD radar. Our analyses in this chapter rectify these deficiencies in the laser radar context.

Chapter IV is divided into three sections: the first section deals with transmitter/LO laser frequency instability; the second section examines the effects of atmospheric turbulence; and the last section studies the effects of two types of motion errors, target/radar platform vibration and transmitter aim error. In each section, we first present a model which, with minimal amount of complexity, represents the physical process whose effects we are investigating. Then, with the model, we derive the performance for SAR and/or RD radar. The results are then discussed and compared with those of the ideal case from Chapter III.

4.1. Effects of Laser Frequency Instability

In this section, we investigate how random frequency instability of the transmitter laser interferes with the coherent processing of the target return, resulting in inferior resolution and CNR compared to the ideal case of perfect frequency stability. First, the instantaneous frequency deviation from the nominal carrier frequency ν_0 is modelled as a stationary random process. Then, several scenarios are examined, based on the coherence time of the laser frequency, the extent of the frequency deviation, and the target range. In deriving the analytical results, we consider both frequency-modulated (FM) waveforms and amplitude-modulated (AM) waveforms. The SAR case will be analyzed first, followed by the RD radar case.

One remark before we proceed: we shall assume throughout the analysis that the LO laser is perfectly coherent with the transmitter laser, i.e., they share the same temporal characteristics except for the nominal frequency offset ν_{IF}. In practice with CO_2 laser radars, the best way of getting this coherence between the two is to use a single laser. This would be done by diverting some of the power from the transmitter laser and then introducing the IF shift via external acousto-optic modulation.

4.1.1. Frequency Instability Model

As stated in Chapter II, frequency instability of the transmitter/LO laser can be represented by including the phase error term (cf. Section 2.1) $\exp[-j\Phi(t)]$ in the target return model where

$$\Phi(t) = 2\pi \int_{-\infty}^{t} du \; \overset{\curvearrowright}{f}(u),$$

and $\overset{\curvearrowright}{f}(t)$ = instantaneous frequency deviation (from ν_0).

We indirectly characterize the phase error $\Phi(t)$ by characterizing $\overset{\curvearrowright}{f}(t)$. $\overset{\curvearrowright}{f}(t)$ will be modelled as a stationary, Gaussian random process. Thus, $\overset{\curvearrowright}{f}(t)$ is completely characterized by its mean and covariance. Following [37], we will assume that $\overset{\curvearrowright}{f}(t)$ has zero as its mean and a double-sided exponential as its covariance function:

$$m_{\overset{\curvearrowright}{f}}(t) = <\overset{\curvearrowright}{f}(t)> = 0,$$
$$K_{\overset{\curvearrowright}{f}\overset{\curvearrowright}{f}}(\tau) = <\overset{\curvearrowright}{f}(t)\overset{\curvearrowright}{f}(t+\tau)> \qquad\qquad (4.1.1)$$
$$= \sigma_f^2 \exp[-|\tau|/t_f],$$

where

t_f = coherence time of the instantaneous frequency
fluctuation $\overset{\curvearrowright}{f}(t)$: $1/t_f$ = short-term bandwidth
of the laser,

σ_f = rms frequency error: long-term bandwidth
of the laser.

Our frequency instability model is based on the assumption that the instantaneous laser frequency drifts randomly. t_f characterizes how rapidly $\tilde{f}(t)$ tends to change, and σ_f represents the extent of frequency drifting. We shall assume $\sigma_f t_f \gg 1$ throughout our analysis.

It follows from the characterization of $\tilde{f}(t)$ that $\Phi(t)$ is also a zero-mean, Gaussian random process (but no longer stationary):

$$m_\Phi(t) = \langle \Phi(t) \rangle = 0,$$

$$K_{\Phi\Phi}(t,u) = \langle \Phi(t) \Phi(u) \rangle \qquad (4.1.2)$$

$$= (2\pi)^2 \int_{-\infty}^{t}\int_{-\infty}^{u} ds_1 ds_2 \; K_{\tilde{f}\tilde{f}}(s_1-s_2).$$

Since we have assumed that a single laser provides both the LO and the transmitter beams, the frequency instability of the laser manifests itself in the beat-frequency component, i.e., the heterodyne-detected target return, as follows:

$$\underline{y}(t;\sigma_f\neq0) = \underline{y}(t;\sigma_f=0) \cdot \underline{w}(t), \qquad (4.1.3)$$

where

$$\underline{w}(t) = \text{frequency-instability-induced term}$$

$$= \exp[-j(\Phi(t-2L/c)-\Phi(t))]. \qquad (4.1.4)$$

$\underline{y}(t;\sigma_f\neq0)$ and $\underline{y}(t;\sigma_f=0)$ correspond to the target returns in the presence of frequency jitter and in the absence of jitter, respectively. Physically, the first factor $\Phi(t-2L/c)$ of $\underline{w}(t)$

represents the cumulative phase error - due to the frequency jitter - of the transmitter beam at the time when the signal was transmitted, while the second factor $\Phi(t)$ represents the phase error of the LO beam when the transmitted beam has come back from the target. In other words, $\underline{w}(t)$ represents the phase error accumulated during the roundtrip time $2L/c$ due to the frequency drifting, where L is the target range and c the speed of light.

By writing the target return in the presence of frequency jitter as a product of $\underline{y}(t;\sigma_f=0)$ and $\underline{w}(t)$, we have implicitly assumed that the discrepancy in the range for various parts of the illuminated target area is negligible compared to the nominal range L.

In light of the discussion thus far and what is to follow, it is clear that we need to characterize $\underline{w}(t)$. In particular, we will need to know the correlation function of $\underline{w}(t)$, $R_{ww}(\tau) = < \underline{w}(t+\tau)\ \underline{w}^*(t) >$. When we evaluate $R_{ww}(\tau)$, we obtain the following exact expression:

$$
\begin{aligned}
R_{ww}(\tau) = \exp[-2(2\pi\sigma_f t_f)^2 \cdot \{\ & 2L/ct_f - 1 + \exp[-2L/ct_f] \\
& - (\ -|\tau|/t_f + |\tau+2L/c|/2t_f + |\tau-2L/c|/2t_f \\
& - \exp[-|\tau|/t_f] + 0.5\exp[-|\tau+2L/c|/t_f] \\
& + 0.5\exp[-|\tau-2L/c|/t_f]\ )\ \}],
\end{aligned}
\qquad (4.1.5)
$$

which reduces to the following special cases for $\sigma_f t_f \gg 1$ [37]:

$$
R_{ww}(\tau) \simeq
\begin{cases}
[1-(4\pi\sigma_f L/c)^2] + (4\pi\sigma_f L/c)^2 \exp[-|\tau|/t_f] \\
\qquad\qquad \text{for } 2L\sigma_f/c \ll 1 , \qquad\qquad\qquad (4.1.6a) \\[4pt]
\exp[-8(\tau/t_{\Theta_1})^2] \\
\qquad\qquad \text{for } 2L/ct_f \ll 1 \ \& \ 2L\sigma_f/c \gg 1 , \quad (4.1.6b) \\[4pt]
\exp[-8(\tau/t_{\Theta_2})^2] \\
\qquad\qquad \text{for } 2L/ct_f \gg 1, \qquad\qquad\qquad (4.1.6c)
\end{cases}
$$

where

$$
t_{\Theta_1} \equiv (ct_f/L)^{1/2}/\,\pi\sigma_f ,
$$
$$
t_{\Theta_2} \equiv \sqrt{2}\,/\pi\sigma_f .
$$

In the above, we have categorized $R_{ww}(\tau)$ into three separate cases: a) short-range; b) medium-range; and c) long-range, according to the roundtrip delay $2L/c$ and the frequency instability parameters t_f and σ_f.

The short-range case represents those situations where $2L\sigma_f/c$, a typical phase error incurred during the roundtrip delay, is negligible. The medium range case applies to those where the typical phase error is large but the roundtrip delay is still much shorter than the laser coherence time so that during the roundtrip delay time, the frequency is more or less constant. Finally, we have the long-range case for which the frequency is apt to change quite significantly and quite often during the roundtrip delay. In most practical situations, we will probably be concerned with the medium- and the long-range cases. Thus we will concentrate on these cases in our analyses.

Before we start the actual analysis, we note that the random

phase $\Phi(t)$ induced by the frequency instability only affects the target return component $\underline{y}(t)$. The noise component $\underline{n}(t)$, characterized by Gaussian white-noise with spectral density $h\nu_0 / \eta$, as we recall, is really a normalized quantity that represents the LO shot noise. Since any phase fluctuation on the part of the LO laser output does not affect the power of the LO beam and photodetectors are sensitive only to power, the phase fluctuation does not show up in the LO shot noise term $\underline{n}(t)$. As a result, we can write

$$< I_y(t;\sigma_f,t_f) > = \int d\bar{s}\; \mathcal{J}(\bar{s})\; g(\bar{s},t;\sigma_f,t_f), \qquad (4.1.7)$$

$$< I_n(t;\sigma_f,t_f) > = \int_{-\infty}^{\infty} du \;\; | \underline{h}(u) |^2 \; (h\nu_0 / \eta), \qquad (4.1.8)$$

where the resolution-determining function $g(\bar{s},t;\sigma_f,t_f)$ is now a quantity averaged over the frequency fluctuation and $\underline{h}(t)$ is the impulse-response of the IF filter.

4.1.2. SAR

In this section, we investigate the performance of SAR's in the presence of frequency instability, using the model derived in the last section. We examine the CW SAR case first, and then generalize to the 2D SAR.

CW SAR

The key quantity we need to compute is $<I_y(t)>$ [We shall not explicitly carry the σ_f, t_f dependences from here on unless they are necessary.] Using the optimal filter $\underline{h}(t)$ we derived in Section 3.2, we get

$$<I_y(t)> = (P_T \pi a_x a_y \lambda /2\sqrt{2} \, Lv^2) \, \exp[-2\alpha L] \, (4/\pi y_{res}^2)^{1/2}$$
$$\cdot \int d\bar{p} \; \mathcal{J}(\bar{p}) \; g_x(x-vt) g_y(y) \, , \qquad (4.1.9)$$

where
$$z=L$$

$$g_x(x) = (4v/\lambda L) \, \exp[-(ka_x x/L)^2/2] \, G_x(4kvx/L), \qquad (4.1.10)$$

$$g_y(y) = \exp[-(2y/y_{res})^2], \qquad (4.1.11)$$

$$G_x(f) \equiv \text{Fourier transform of}$$
$$R_{ww}(2\tau) \cdot \exp[-32(\tau/T)^2]. \qquad (4.1.12)$$

In the expressions above, R_{ww} is the correlation function given by Eqs. (4.1.5) and (4.1.6). All other notations are same as in Section 3.2.1, including y_{res} (the cross-track resolution in the absence of frequency instability) and T (the optimal coherent

prcessing time - cf. (3.2.14)).

The first thing we note from the above is that $g_x(x)$ and $g_y(y)$ determine the along-track and cross-track resolutions, respectively, in the presence of frequency instability. Not surprisingly, we find that the cross-track resolution is unaltered by the frequency jitter since it is derived from the laser beamwidth on the target in y-direction and the beamwidth is not affected by frequency jitter.

When there is no frequency instability, $R_{ww}(2\tau) = 1$ for all τ, and (4.1.9) reduces to the ideal-case result (3.2.15), as it should. With frequency instability, the along-track resolution is now given by the fullwidth between the e^{-1} attenuation points of the function $g_x(x)$. To quantify the resolution loss due to frequency instability, we present $g_x(x)$ results obtained by using the $R_{ww}(\tau)$ of Section 4.1.1:

$$
g_x(x) \simeq
\begin{cases}
\begin{aligned}
&(4/\pi x_{res}^2)^{1/2} \exp[-(ka_x x/L)^2/2)] \\
&\cdot \{ [1-(4\pi\sigma_f L/c)^2] \exp[-2(x/a_x)^2] \\
&+ (4\pi\sigma_f L/c)^2 t_f / [(1 + (4kvt_f x/2L)^2)\sqrt{2\pi} (T/8)] \}, \\
&[\text{for } t_f \ll T] \qquad :\text{short-range} \qquad (4.1.13) \\
\\
&(1/\varepsilon_1)(4/\pi x_{res}^2)^{1/2} \exp[-(ka_x x/L)^2/2] \\
&\cdot\exp[-2(x/\varepsilon_1 a_x)^2], \quad :\text{medium-range} \qquad (4.1.14) \\
\\
&(1/\varepsilon_2)(4/\pi x_{res}^2)^{1/2} \exp[-(ka_x x/L)^2/2] \\
&\cdot\exp[-2(x/\varepsilon_2 a_x)^2], \quad :\text{long-range} \qquad (4.1.15)
\end{aligned}
\end{cases}
$$

where

$$\varepsilon_1 \equiv [1 + (T/t_{\theta_1})^2]^{1/2},$$

$$\varepsilon_2 \equiv [1 + (T/t_{\theta_2})^2]^{1/2}, \hspace{2cm} (4.1.16)$$

$$x_{res} = \text{x-resolution in the absence of instability}$$

$$= \sqrt{2}\, a_x \quad (\text{cf. Eq. (3.2.14)}).$$

t_{θ_1} and t_{θ_2} are the characteristic correlation time for $\underline{w}(t)$ in the medium- and long-range cases, respectively, as given by (4.1.6). These results are to be compared with the behavior of $g_x(x)$ in the absence of frequency instability:

$$g_x(x) = (4/\pi x_{res}^2)^{1/2} \exp[-(ka_x x/L)^2/2]$$
$$\cdot \exp[-(2x/x_{res})^2]. \hspace{2cm} (4.1.17)$$

We can interpret our results as follows.

For the short-range case, effect of the frequency instability should be minimal since the typical phase error incurred during the roundtrip delay time $2\pi\sigma_f(2L/c)$ is very small in this regime. A small phase error means that even with frequency drifting, temporal coherence of the return signal is likely to be maintained throughout the coherent integration time. Our expectation is verified by (4.1.13) [where we have assumed the coherent integration time T to be much greater than the coherence time of the laser t_f]: the frequency instability-induced terms involving $(4\pi L\sigma_f/c)^2$ are seen to be relatively small.

In the medium-range case, t_f is still much longer than $2L/c$, but now a typical phase deviation during $2L/c$ greatly exceeds unity. Therefore, we would expect that when T is sufficiently long compared to t_f, the random frequency drifting during the coherent integration process will give rise to a partial loss of target return's temporal coherence, and thus a loss of spatial resolution. This can be seen in the broadening of the width of $g_x(x)$ by factor $\varepsilon_1 = [1 + (T/t_{\Theta_1})^2]^{1/2}$.

In the long-range case, we have the condition $2L/c \gg t_f$ in addition to $4\pi L\sigma_f/c \gg 1$, implying a random frequency drifting during the roundtrip time $2L/c$ itself. This, of course, means even worse degradation of resolution than the medium-range case: $g_x(x)$ broadens out by factor $\varepsilon_2 = [1 + (T/t_{\Theta_2})^2]^{1/2}$ where t_{Θ_2} is independent of the range L.

One thing we should keep in mind is that the along-track resolution cannot get worse indefinitely as t_Θ decreases because of the limiting exponential factor $\exp[-(ka_x x/L)^2/2]$; this point is illustrated in Fig. 4.1 where x-resolution is plotted as a function of t_Θ for the medium- and long-range cases [with T fixed]. Physically, this bound on the resolution exists because the finiteness of the coherent processing time and the on-target beamwidth place an upper bound on the target area which contributes to the output of the IF filter at any given time, and frequency instability, no matter how severe it may be, cannot change that fact.

Let us define a resolution-breakpoint as the t_Θ value at
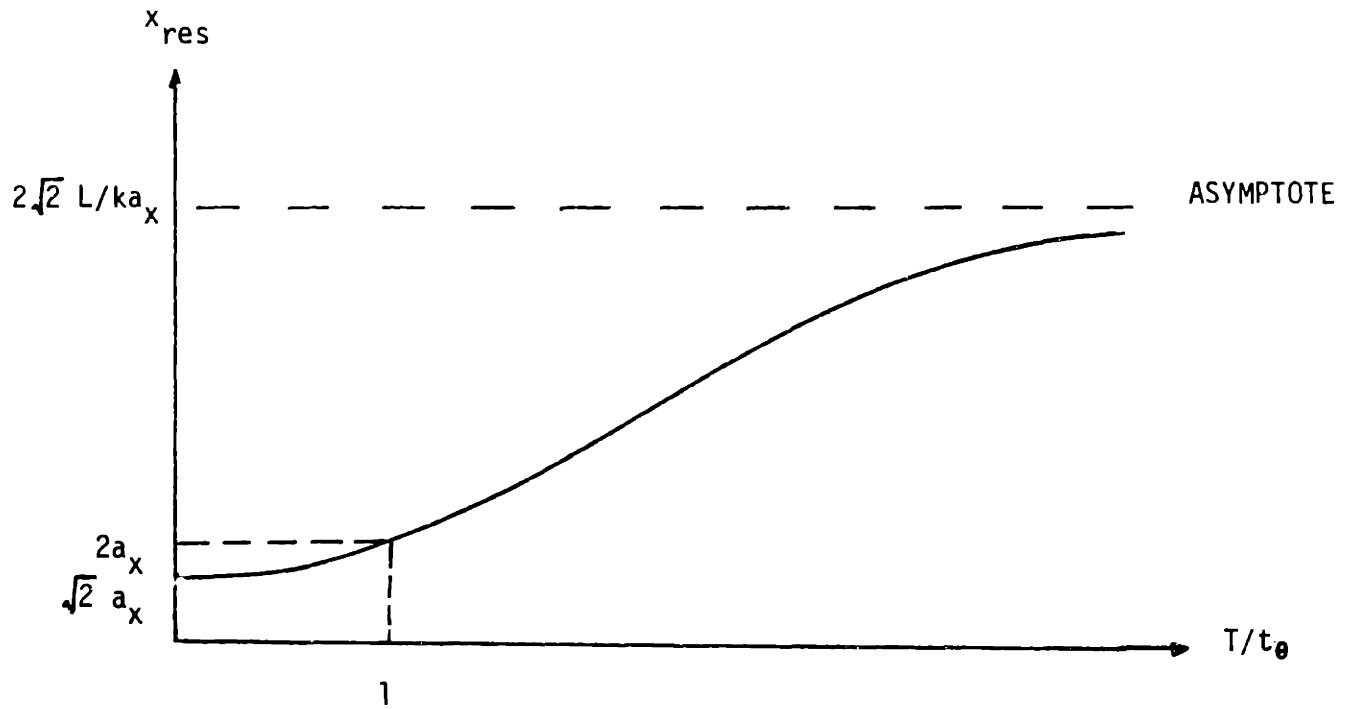
Fig. 4.1   SAR's Along-Track Resolution x_{res} vs. T/t_θ
(for a Fixed Value of T)

which the x-resolution becomes $2a_x$, i.e., $\sqrt{2}$ times its value without frequency instability. Then, for the medium- and long-range cases, this breakpoint occurs when $t_\theta = T$. In Chapter V, we will work out some numerical examples.

We now examine the effect frequency instability has on CNR for the medium- and the long-range cases. For the sake of simplicity, we will assume a uniform target reflectivity. We find that

$$CNR_{CW\ SAR}(\sigma_f \neq 0) = CNR_{CW\ SAR}(\sigma_f=0) \cdot \varepsilon_{instab}, \qquad (4.1.18)$$

where

$$CNR_{CW\ SAR}(\sigma_f=0) = \text{CNR result of (3.2.17) for the ideal}$$
$$\text{case (no frequency jitter),} \qquad (4.1.19)$$

$$\varepsilon_{instab} = \text{CNR loss factor due to instability}$$
$$= 1/[1 + (ka_x^2/2L)^2 \varepsilon_i^2]^{1/2}, \quad i = 1,2$$

ε_1, ε_2 are as defined in (4.1.16). A quick glance at (4.1.19) reveals that we have a 3-dB CNR loss when $\varepsilon_i = [1 + (T/t_{\theta_i})^2]^{1/2} = 2L/ka_x^2$. Because we are in the far-field ($L/ka_x^2 \gg 1$), this implies that a significant CNR loss occurs only when $t_\theta \ll T$. In terms of t_θ, the condition for a 3-dB loss is

$$1/t_\theta \simeq (2L/ka_x^2)/T$$
$$= \sqrt{\pi/32}\ B_{CW\ SAR}, \qquad (4.1.20)$$

where $B_{CW\ SAR}$ is the effective receiver bandwidth of (3.2.20).

Some physical insight into (4.1.20) can be gained by keying on what frequency instability does to the target return from a single scatterer. As the laser frequency becomes more unstable, the phase history of the return gets more distorted, and as a result, the target return spectrum broadens. Since the amount of energy in the return is unaffected by the frequency jitter, the target return spectrum broadening means there is now less energy within the receiver bandwidth. This mechanism, combined with the fact that LO shot noise is not affected by frequency instability, reduces the CNR. Equation (4.1.20) represents the situation where the extent of spectrum broadening due to the frequency instability becomes comparable to the filter (receiver) bandwidth itself. In fact, $1/t_\theta$ is roughly the bandwidth of the instability-induced term $\underline{w}(t)$ (cf. (4.1.6)).

It is interesting to note that at the breakpoint of the resolution as previously defined, we have $\varepsilon_i = \sqrt{2}$, and thus, $\varepsilon_{instab} = 1/[1 + 2(ka_x^2/2L)^2]^{1/2} \simeq 1$. In other words, there is little CNR-loss from the perfectly stable case. So, we get a resolution loss long before we incur a CNR-loss. This is consistent with the findings in [37] for a conventional Doppler imager.

2D SAR

We now turn our attention to 2D SAR. In trying to understand the 2D SAR case, we immediately confront some issues we did not need to consider in the CW SAR analysis. The first and perhaps the most important new issue concerns how the loss of target return temporal coherence, measured against both the coherent integration time T and the duration of single (transmitted) pulse, degrades both along-track and cross-track resolution. We shall deal with the medium- and long-range cases only, as the short-range case is rather uninteresting. [Recall that there was little along-track resolution loss in the CW SAR analysis for the short-range case. We expect even less loss for the cross-track resolution in the 2D SAR case because of shorter integration time required in resolving the cross-track coordinates.]

The second new issue we face is the question of periodic sampling. In particular, what are the consequences of sampling at the rate $\sim v/a_x$ as prescribed by our earlier analysis (cf. (3.2.34) of Section 3.2.2) when the target return spectrum is broader than $\sim v/a_x$ because of frequency instability?

Finally, there is a modelling issue regarding the phase error term $\underline{w}(t)$: can we continue to model it as $\exp[-j(\Phi(t)-\Phi(t-2L/c))]$ and leave out the transverse coordinate dependence from the roundtrip delay $2L/c$? This question is pertinent for the 2D case, given the fact that we

have a range-delay spread of $\sim(\lambda L/a_\perp \cot \psi)/c$, which is appreciably larger than the range-delay spread of the CW SAR case, viz. $(\lambda L/a_x)^2/Lc$. It is possible that the spread of the range-delay is large enough to warrant introducing a coordinate-dependent correction term into the roundtrip delay: we would then have $\Phi(t-2L/c-\tau(\bar{p}))$ instead of $\Phi(t-2L/c)$, where $\tau(\bar{p})$ is the correction term. However, in most practical situations, the nominal range L is much larger than the beamwidth, and we really need not worry about the coordinate-dependent correction term since it is doubtful that this small correction will change the overall character of the problem. We now proceed with the analysis.

If we assume that the range spread of the target is much smaller than the nominal range itself, then we may write the complex envelope of the target return in 2D format as follows:

$$\underline{y}(m,\tau) = \underline{y}_o(m,\tau) \cdot \underline{w}(m,\tau), \qquad (4.1.21)$$

where

$\underline{y}_o(m,\tau)$ = target return in the absence of frequency
  instability: given by (3.2.27) and (3.2.28),

$\underline{w}(m,\tau)$ = frequency instability term introduced in (4.1.4)
  $= \exp[-j(\Phi(mT_s+\tau-2L/c) - \Phi(mT_s+\tau))].$ (4.1.22)

When $\underline{y}(m,\tau)$ is passed through the two-stage IF filter described in Section 3.2.2, we have the following output:

$$\underline{1}_y(m,\tau) = \underline{B} \int d\bar{p}\ \underline{T}(\bar{p})\ \exp[2jkycos\ \psi\ +\ jk(ysin\ \psi\ )^2/L$$
$$-(ka_\perp ysin\ \psi\ /L)^2/2]\ \underline{Q}'(x,y,m,\tau),\qquad (4.1.23)$$

where

$$\underline{Q}'(x,y,m,\tau)\ \equiv\ \int_{-T_s/2}^{T_s/2} d\tau'\ \underline{f}^*(\tau-\tau')\ \underline{f}(\tau'-2ycos\ \psi\ /c)$$
$$\cdot \sum_{m'=-\infty}^{\infty} \exp[(-jk/L\ -\ (ka_x/L)^2/2)(vT_s)^2(m-m')^2]$$
$$\cdot \exp[(jk/L\ -\ (ka_x/L)^2/2)(x-v(m'T_s+\tau'))^2]$$
$$\cdot\ \underline{w}(m',\tau').\qquad (4.1.24)$$

All the symbols and notations, unless defined differently in this section, are as established in Section 3.2.2. The corresponding average intensity $< I_y(m,\tau)\ > = <\ |\ \underline{1}_y(m,\tau)|^2\ >$ is given by

$$< I_y(m,\tau)\ >\ =\ |\ \underline{B}|^2\lambda^2 \int d\bar{p}\ \mathcal{J}(\bar{p})\ \exp[-(ka_\perp ysin\psi\ /L)^2]$$
$$\cdot<\ |\ \underline{Q}'(x,y,m,\tau)|^2\ >.\qquad (4.1.25)$$

The calculation of $<\ |\ \underline{Q}'(x,y,m,\tau)|^2\ >$ is rather tedious and omitted here. Interested readers are referred to Appendix A. Quoting the end result, we have

$$<\ |\ Q'(x,y,m,\tau)|^2\ >$$
$$=\ \{\ (\pi T_o^2/8\varepsilon_a)\ \exp[-((\pi W_o/\varepsilon_a)^2\ +\ (4/T_o)^2)\cdot(cos\ \psi\ /c)^2$$
$$\cdot(y-c\tau/2cos\ \psi\ )^2]\ \}\qquad (4.1.26)$$
$$\cdot\{\ S_1\ +\ S_2\ \},$$

where

$$S_1 = (\pi/4a_2\varepsilon_b) \cdot \exp[-a_2(m - \tilde{x})^2]$$

$$\cdot \{ \sum_{\ell'=-\infty}^{\infty} \exp[-(2\pi l')^2/16a_2] \exp[-j(m + \tilde{x})\pi l'] \}$$

$$\cdot \{ \sum_{\ell''=-\infty}^{\infty} \exp[-(a_1^2/\varepsilon_b^2 a_2) \cdot (\tilde{x} - m + \pi l''/2a_1 \qquad (4.1.27)$$

$$+ (\pi W_o/T_c)T_s(2y\cos\psi/c - \tau)/a_1(1 + (t_\Theta/T_o)^2/2))^2],$$

S_2 = same as (4.1.27) except that in the l'- and

l"-summations, there are extra factors of

$(-1)^{l'}$ and $(-1)^{l''}$, respectively, in the summands.

and

$$a_1 \equiv (k/L)(vT_s)^2$$

$$a_2 \equiv 2(ka_x/2L)^2(vT_s)^2$$

$$\tilde{x} \equiv x/vT_s \qquad\qquad (4.1.28)$$

$$\varepsilon_a \equiv [1 + 2(T_o/t_\Theta)^2]^{1/2}.$$

$$\varepsilon_b \equiv [1 + (2T_s/T_o)^2/a_2/(1 + (t_\Theta/T_o)^2/2)]^{1/2}$$

t_Θ = characterstic correlation time for frequency

instability [cf. Eq. (A.2)].

In deriving this result, we have let $\underline{f}(t)$ be the chirped Gaussian pulse of (3.2.25). Let us examine the result.

First, we note that the portion of the cross-track resolution c rived from frequency modulation has a loss factor of ε_a; this is obvious from the $(\pi W_o/\varepsilon_a)^2$ term in the first exponential of Eq. (4.1.26). Much like the along-track resolution in the CW SAR case earlier, extent of the cross-track resolution loss is seen to depend on the relative durations of the transmitted pulse (T_o) and the characteristic perturbation

time (t_Θ). Because the pulse duration in a typical application
is quite short, we expect very little cross-track resolution loss
even when the along-track resolution loss may be quite
significant. This is due to the enormous difference in the
coherent integration times required to resolve the along-track
and cross-track coordinates: $\sim \lambda L/a_x v$ for the along-track
coordinate as opposed to $\sim T_o$ for the cross-track coordinate.
There is no resolution loss when unmodulated pulses are
transmitted, i.e., when $W_o = 0$.

A few comments regarding S_1 and S_2 before we discuss the
along-track resolution loss. The exponential $\exp[-\alpha_2(m - \tilde{x})^2]$,
or equivalently $\exp[-2(ka_x/2L)^2(x-mvT_s)^2]$, corresponds to the
beam pattern on the target in the x-direction. As far as the
l'-summation is concerned, we need to keep only the l' = 0 term
for vT_s on the order of a_x or less because of the far-field
condition. In that case, the l'-summation collapses to unity.

The width of the exponential inside the l"-summation gives
the along-track resolution - that is based on coherent summation
of the target return - for 2D SAR in the presence of frequency
instability. Employing the expressions provided for α_1, α_2, and
$\tilde{x}$, we see that the along-track resolution is degraded by factor
of ε_b. It is interesting to note that the loss factor ε_b is
different from that of the CW case, which is $[1 + (T/t_\Theta)^2]^{1/2}$
(cf. Eq. (4.1.16)). However, when the frequency instability
correlation time t_Θ is much longer than the pulse duration T_o, ε_b
does reduce to the CW result.

A curious feature of the S_1 and S_2 expressions is the shift in the along-track coordinate of the target area that appears in the output image. This shift, represented by the term $(\pi W_o/T_o)T_s\ldots$ in Eq. (4.1.27), occurs as a result of the coupling between m and τ through the correlation function R_{ww}, and is small for $t_\Theta \gg T_o$.

We now address the issue of sampling rate (PRF) and aliasing, which was raised at the beginning of this section. It is clear from the structure of Eq. (4.1.27) that more than one isolated region of the target would contribute to the output intensity at any given time if the PRF is low enough (see Fig. 4.2a). As mentioned in Section 3.2.2, this type of aliasing arises from discrete nature of the 2D SAR's along-track processing and can be avoided by increasing the sampling rate beyond $\sim v/a_x$ (see Fig. 4.2b).

There is now, however, another type of aliasing to consider, which arises from the loss of along-track resolution caused by frequency instability. When there is significant frequency instability, pulses representing various 1" terms in the S_1 and S_2 expressions above broaden and start to overlap with the adjecent pulses (see Fig. 4.2c). Moreover, this overlapping could occur even when the PRF is sufficiently high to ensure that the first type of aliasing does not occur, i.e., the periodic interval $\lambda L/vT_s$ is greater than the beam pattern width $\lambda L/a_x$. This situation can be rectified to some degree by increasing the sampling rate even more. We say to some degree because even

BEAM PATTERN:
$\exp[-(ka_x/2L)^2(x-mvT_s)^2]$

$\sim a_x \epsilon_b$

$1^n = 3$ $1^a = 2$ $1^a = 1$ $1^a = 0$ $1^a = -1$ $1^a = -2$ $1^m = -3$

$x-mvT_s$

a) Undersampled Case

$2\pi/(2kvT_s/L)$

$1^a = 1$ $1^a = 0$ $1^a = -1$

$x-mvT_s$

b) Adequately-sampled Case

BROADENING DUE TO SEVERE
FREQUENCY INSTABILITY

$1^a = 1$ $1^a = 0$ $1^a = -1$

$x-mvT_s$

OVERLAP

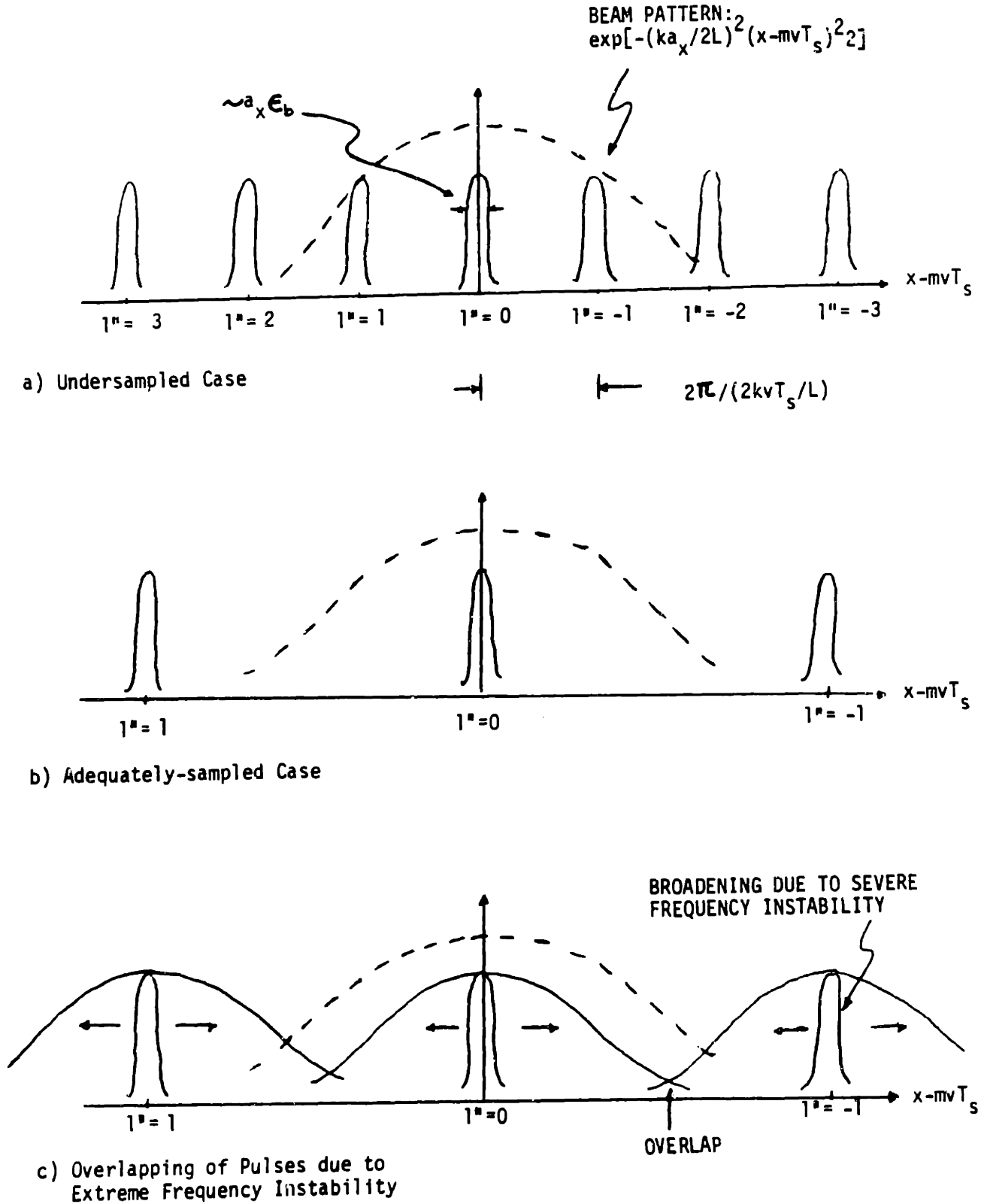c) Overlapping of Pulses due to
Extreme Frequency Instability

Fig. 4.2 Effect of Low Sampling Rate (PRF) and
Frequency Instability on 2D SAR's Along-Track Resolution

though a high sampling rate would solve the overlapping problem, it cannot alleviate the frequency-instability-induced pulse broadening itself. In fact, once the (broadened) pulse width becomes comparable to the beamwidth [this occurs when $vt_\Theta \sim a_x$], the sampling rate and aliasing issues become academic since the along-track resolution is then governed by the beamwdith.

We shall assume that the PRF is sufficiently high and that $t_\Theta \gg T_o$ prevails in what follows, so that the overlapping does not occur and the cross-track resolution loss is negligible. Then, we can simplify the expressions for S_1 and S_2 considerably by retaining only $l' = 0$ and $l'' = 0$ terms from the double summation, and $S_1 + S_2$ becomes

$$S_1 + S_2 = (\pi/2\alpha_2\varepsilon_b)\cdot\exp[-\alpha_2(m - \tilde{x})^2]$$
$$\cdot\exp[-(\alpha_1^2/\varepsilon_b^2\alpha_2)\cdot(\tilde{x} - m)^2] \qquad (4.1.29)$$

Moreover, in this regime, because only the along-track resolution is significantly affected, the CNR differs from the ideal case in a manner identical to the CW SAR case. We have

$$CNR_{2D\ SAR}(\sigma_f \neq 0) = CNR_{2D\ SAR}(\sigma_f = 0)\cdot\varepsilon_{instab}, \qquad (4.1.30)$$

where

$$\varepsilon_{instab} \simeq 1/[1 + (ka_x^2/2L)^2\varepsilon^2]^{1/2}, \qquad (4.1.31)$$

$$\varepsilon = [1 + (T/t_\Theta)^2]^{1/2}. \qquad (4.1.32)$$

Note that the ε_{instab} above is identical to the ε_{instab} of the CW

case (cf. (4.1.19)). This means that we once again have a loss

of along-track resolution long before the onset of CNR-loss.

4.1.3. RD Radar

In this section, we look at how RD radars perform in the presence of frequency instability. As there are a great deal of similarities between the 2D SAR imaging and the RD imaging with two-step processing (cf. Section 3.3.2), we will not dwell on the impact of frequency instability on that particular type of RD imaging. Instead, we will exclusively look at the effect an unstable laser has on the type of RD imaging introduced in Section 3.3.1. In particular, we shall be interested in learning how frequency instability affects the Doppler and range-delay resolutions of a system employing FM waveforms differently than those of a system employing AM waveforms. We would like to quantify these effects as well as the CNR behavior in terms of the waveform duration and the correlation time t_Θ.

Once again incorporating the effect of laser frequency instability with $\underline{w}(t)$, we modify the two-frequency correlation function $\underline{X}$ of (3.3.8) as follows [the other parts of the expression for $<I_y(t; \nu_D')>$ remain the same as before]:

$$| \underline{X}(\tau, \Delta \nu_D)| = | \int_{-\infty}^{\infty} du \, \underline{s}_n^*(u+\tau) \, \underline{s}_n(u) \, \underline{w}(u+2L/c) \, \exp[-j2\pi u \, \Delta \nu_D]|$$

$$(4.1.33)$$

The ensemble-averaged ambiguity function is then given by:

$$< T(\tau, \Delta \nu_D) > = <| \underline{X}(\tau, \Delta \nu_D)|^2> / | \underline{X}_o|_w^2$$

$$= \int_{-\infty}^{\infty} \int_{-\infty}^{\infty} du' du'' \; \underline{s}_n^*(u'+\tau) \; \underline{s}_n(u') \; \underline{s}_n(u''+\tau) \; \underline{s}_n^*(u'')$$

$$\cdot R_{ww}(u'-u'') \; \exp[-j2\pi(u'-u'') \; \Delta\nu_D \;]$$

$$\cdot (1/ \; | \; \underline{X}_o \; |_w^2) , \qquad (4.1.34)$$

where

$$| \; \underline{X}_o \; |_w^2 \quad \equiv \int_{-\infty}^{\infty} \int_{-\infty}^{\infty} du' du'' | \; \underline{s}_n(u') |^2 \cdot | \; \underline{s}_n(u'') |^2 \; R_{ww}(u'-u'') .$$

$$(4.1.35)$$

$R_{ww}(u'-u'')$ is the correlation function of $\underline{w}(t)$.

To be consistent with the previously adopted convention, the range-delay and Doppler resolutions τ_{res} and $\Delta\nu_{res}$ are defined by the following relations:

$$< T \; (\tau_{res}/2, 0) \; > \; = \; (1/| \; \underline{X}_o \; |_w^2) \int_{-\infty}^{\infty} \int_{-\infty}^{\infty} du' du'' \; \underline{s}_n^*(u'+\tau_{res}/2) \; \underline{s}_n(u')$$

$$\cdot \; \underline{s}_n(u''+\tau_{res}/2) \; \underline{s}_n^*(u'') \; R_{ww}(u'-u'')$$

$$= \; e^{-1} , \qquad (4.1.36)$$

$$< T \; (0, \Delta\nu_{res}/2) \; > \; = \; (1/| \; \underline{X}_o \; |_w^2) \int_{-\infty}^{\infty} \int_{-\infty}^{\infty} du' du'' | \; \underline{s}_n(u') |^2 | \; \underline{s}_n(u'') |^2$$

$$\cdot R_{ww}(u'-u'') \; \exp[-j2\pi(\Delta\nu_{res}/2)(u'-u'')]$$

$$= \; e^{-1} . \qquad (4.1.37)$$

We shall now consider two specific waveforms, one an FM waveform and the other an AM waveform. To facilitate the ease of comparison in the end, we adopt the following waveforms with which we are already familiar:

i) FM: $\underline{s}_n(t) = \exp[-j\pi W_o t^2/T_o - 4t^2/T_o^2]$,

$$(4.1.38)$$

ii) AM: $\underline{s}_n(t) = \exp[-4t^2/T_o^2]$.

For these waveforms, the modified ambiguity function takes on the following form:

i) $< T(\tau, \Delta\nu_D) > = \exp[-((W_o\tau - \Delta\nu_D T_o)\pi/2)^2/\varepsilon^2] \exp[-4\tau^2/T_o^2]$,

$$(4.1.39)$$

ii) $< T(\tau, \Delta\nu_D) > = \exp[-(\pi\Delta\nu_D T_o/2)^2/\varepsilon^2] \exp[-4\tau^2/T_o^2]$,

$$(4.1.40)$$

where

$$\varepsilon \equiv [1 + 2(T_o/t_\Theta)^2]^{1/2}, \qquad (4.1.41)$$

$$|\underline{X}_o|_W^2 = \pi T_o^2/8\varepsilon \quad \text{for both.} \qquad (4.1.42)$$

In the above, we have assumed

$$R_{WW}(u) = \exp[-8(u/t_\Theta)^2], \qquad (4.1.43)$$

where t_Θ represents the characteristic correlation time for either the medium- or long-range case (cf. (4.1.6) in Section 4.1.1).

From the expressions above, we can easily obtain the Doppler and range-delay resolutions: the results are conveniently summarized in the table below:

$$\Delta\nu_{res} \qquad\qquad \tau_{res} \qquad\qquad (4.1.44)$$

i) FM $\quad 4\varepsilon/\pi T_O \qquad\qquad 2/[(\pi W_O/2\varepsilon)^2 + (2/T_O)^2]^{1/2}$

$\qquad\qquad \{4/\pi T_O\} \qquad\qquad \{2/[(\pi W_O/2)^2 + (2/T_O)^2]^{1/2}\}$

ii) AM $\quad 4\varepsilon/\pi T_O \qquad\qquad T_O$

$\qquad\qquad \{4/\pi T_O\} \qquad\qquad \{T_O\}$

The expressions in the braces { } denote the resolutions under perfect frequency stability assumption.

The effect frequency instability has on the range-delay and Doppler resolutions may also be graphically illustrated on the τ - $\Delta\nu_D$ plane by plotting the contour of the e^{-1}-points of the modified ambiguity function. This is shown in Fig. 4.3, where we have plotted the results for the waveforms under consideration. The dashed lines represent the corresponding contours for the ideal case of perfect frequency stability. Note that the original e^{-1}-contours are expanded as a result of the resolution loss suffered from the instability. We will come back to this figure later.

We now interpret the results we have obtained. Although the results were obtained for two specific waveforms, they, nevertheless, exemplify the contrast in behaviors exhibited by range-delay and Doppler resolutions, and also by systems employing AM and FM waveforms.

We will comment on the Doppler resolution first. That the
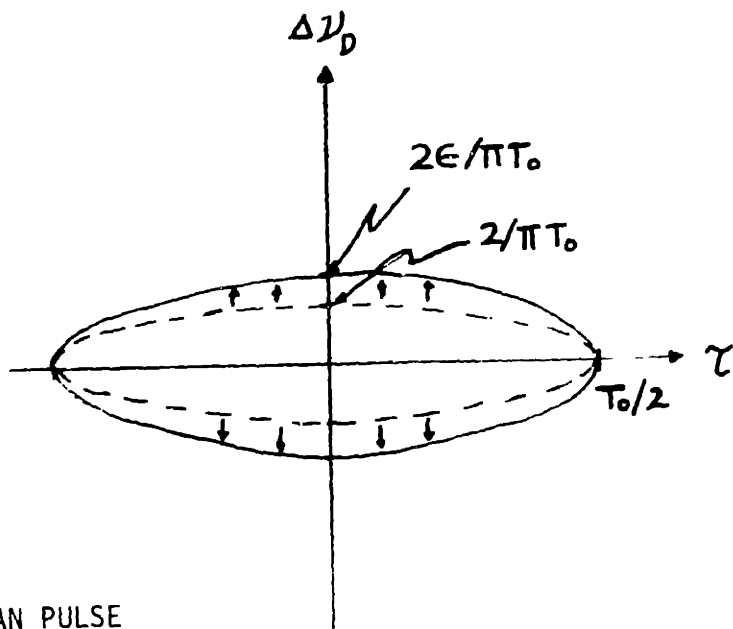
a) SIMPLE GAUSSIAN PULSE
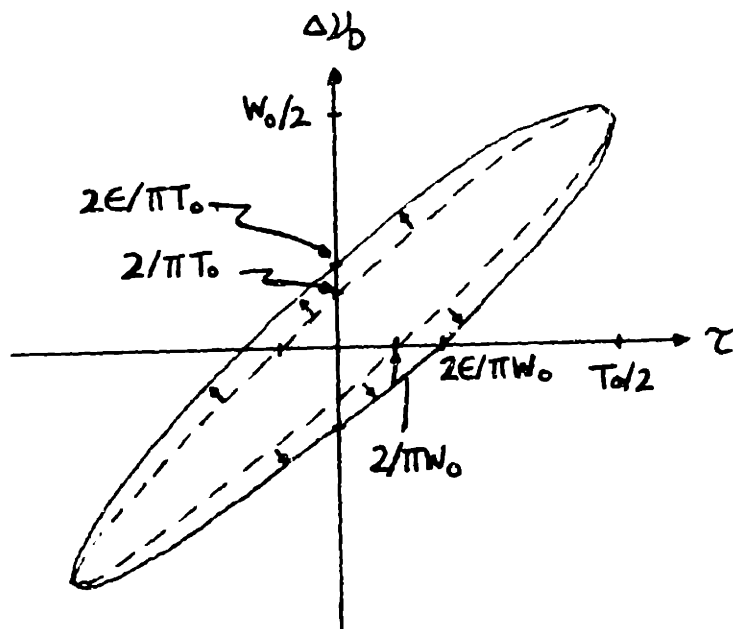
b) CHIRPED-GAUSSIAN PULSE

$- - -$ NO INSTABILITY

_____ INSTABILITY

Fig. 4.3 Expansion of Ambiguity Function's e^{-1}-Contour as a Result of Frequency Instability

Doppler resolution is degraded in the same manner - by the loss factor ε - for both AM and FM systems comes as no surprise to us. Looking at Eq. (4.1.37), we see that it is $|\underline{s}_n(u')|^2$, $|\underline{s}_n(u'')|^2$, and $R_{ww}(u'-u'')$ which figure in determining the Doppler resolution $\Delta\nu_{res}$ and therefore, only the amplitude of the transmitted signal $\underline{s}_n(t)$ is of any relevance. And since our two waveforms have the same type of amplitude history, their Doppler resolutions should have the same functional form.

In fact, we can make an even stronger statement about the relationship between Doppler resolution and frequency instability in general. Let us rewrite (4.1.37) in terms of the sum and difference coordinates $u_+ = u'+u''$ and $u_- = u'-u''$. We then have

$$< T (0, \Delta\nu_{res}/2) > = (1/|\underline{X}_o|^2_w) \int_{-\infty}^{\infty} du_- \, R_{ww}(u_-) s_+(u_-)$$
$$\cdot \exp[-j2\pi(\Delta\nu_{res}/2)u_-],$$

where (4.1.45)

$$s_+(u_-) = \int_{-\infty}^{\infty} du_+ |\, s_n((u_++u_-)/2)|^2 \cdot |\, \underline{s}_n((u_+-u_-)/2)|^2$$

(4.1.46)

In this form, we recognize that the integral of (4.1.45) is a Fourier transform, and $\Delta\nu_{res}$ measures the bandwidth of the product $R_{ww}(u_-)s_+(u_-)$, where the duration of $s_+(u_-)$ is roughly same as that of $\underline{s}_n(t)$. In the absence of frequency instability, i.e., with $R_{ww}(u_-) = 1$, the bandwidth of the product is $\sim 1/T_o$, where T_o is the waveform duration of $\underline{s}_n(t)$. However, with instability, the bandwidth is $\sim (1/T_o + 1/t_\Theta)$, where we have taken the bandwidth of $R_{ww}(u_-)$ to be $\sim 1/t_\Theta$, inverse of the

correlation time for R_{ww}. Thus, the Doppler resolution degrades by a factor $\sim 1 + (T_o/t_\Theta)$. Admittedly, this is a rather crude approximation; nevertheless, the general description of the $\Delta\nu_{res}$ behavior in relation to T_o and t_Θ is correct, as we can see from the Table (4.1.44) and Eq. (4.1.41)

Speaking in more physical terms, the manner in which the Doppler resolution suffers from frequency instability is a natural manifestation of the fact that our ability to sort out various Doppler components depends on the amount of time we have available to observe them. In our case, because the frequency instability introduces a time-varying random phase to the Doppler components, the coherence time of the Doppler components becomes the relevant quantity in determining the Doppler resolution. Thus, a long correlation time t_Θ - long compared to the signal duration - implies that the Doppler resolution is determined essentially by the full signal waveform and as a result, there is little Doppler resolution loss from the perfect stability case. On the other hand, if the correlation time is short, then it is the correlation time that effectively limits the extent of coherent processing that can be done and ultimately determines the Doppler resolution. In this case, the resolution loss would be significant.

We stated in the preceding paragraphs that there is no difference in Doppler resolution between the systems using FM waveforms and the systems using AM waveforms if the waveforms have the same amplitude history. The distinction between the two

occurs in the range-delay resolution. Unfortunately, we cannot give a simple, yet general mathematical treatment for range-delay resolution as we did with Doppler resolution. Therefore, we will primarily resort to physical arguments.

Achieving a fine range-delay resolution with a wideband FM waveform involves, much like attaining a good Doppler resolution, coherent processing of the target return and thus requires adequate temporal coherence on the part of the target return. Therefore, we expect the range resolution behavior to be similar to that of the Doppler resolution. Our assertion is substantiated by the fact that the range resolution loss behavior associated with our chirped Gaussian pulse is same as that of the Doppler resolution; they are both governed by ε.

With AM waveforms, however, a perturbation to the nominal laser frequency is inconsequential in determining the range-delay resolution. This is because the range-delay resolution is purely determined by the duration of the transmitted waveform [and the phase fluctuation due to the laser instability does not affect the waveform duration]. This point is illustrated in Fig. 4.4, where a typical target return from two point scatterers having different range values is matched-filtered. Note that despite the presence of frequency-instability-induced fluctuations within each output envelope, the envelope duration, i.e., the range-delay resolution, is still determined by the transmitted waveform duration.

As explained in Section 3.3.1, range-delay and Doppler

RANDOM PHASES DUE TO
FREQUENCY INSTABILITY

$\sim T_o$
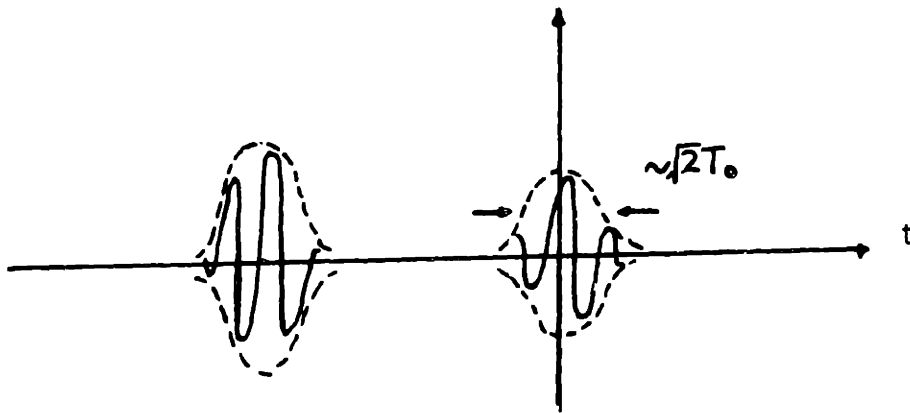
$h(t)$

$\sim T_o$

*

t

t
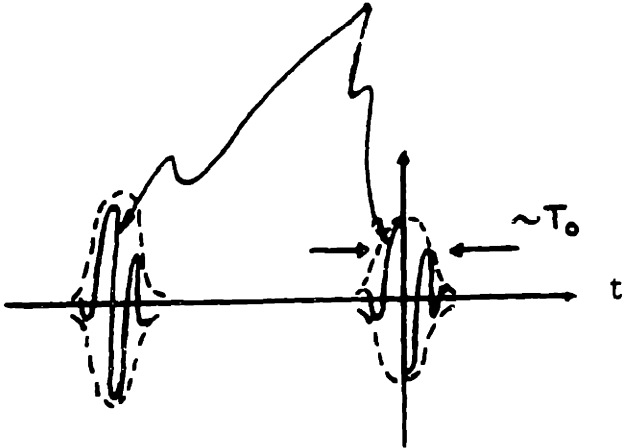
TARGET RETURN FROM POINT SCATTERERS
WITH DISTINCT RANGE VALUES

MATCHED-FILTER

$\sim \sqrt{2}T_o$

t
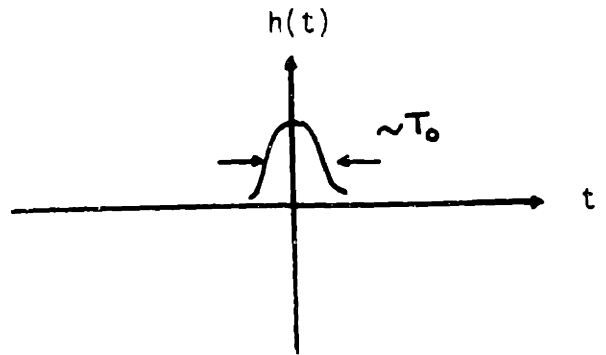
OUTPUT

Fig. 4.4   Illustration of the Invariance of Output Pulse Duration
with Respect to Frequency Instability

resolutions alone do not provide a complete picture in terms of the overall image resolution for the type of RD processing we are considering here. Thus, an appropriate question to ask at this time might be "how is the resolution cell, defined by the e^{-1}-contour of the ambiguity function, affected by the instability of the laser frequency?" Looking at Fig. 4.3, we see that in both the AM and FM cases analyzed earlier (cf. (4.1.38)-(4.1.40)), the resolution cell enclosed by the e^{-1}-contour is stretched along some particular direction, indicating the loss of resolution along that direction. For the simple Gaussian pulse, the stretching occurs along the Δv_D -axis since only the Doppler resolution is derived from coherent processing. On the other hand, the resolution loss occurs in a slanted direction for the chirped Gaussian pulse since both the Doppler and range resolutions are derived from coherent processing of the return.

Recall that under the perfect frequency stability condition, the volume-invariance property of the ambiguity function (cf. 3.3.15) ensures invariance of the effective target area which contributes to the output intensity at a given time regardless of what the transmitted waveform may be (for a large target). We would like to know whether that property still holds in the presence of frequency instability. The preliminary indication from our sample calculations - that the e^{-1}-contours are extended only along one particular direction in each case and by the same factor ε - hints such a possibility. Carrying out the calculation of $\int_{-\infty}^{\infty}\int_{-\infty}^{\infty} d\tau d \Delta v_D \; < T \, (\tau, \Delta v_D \;) >$, we obtain

$$\int_{-\infty}^{\infty}\int_{-\infty}^{\infty} dt\, d\Delta\nu_D \; < T(\tau, \Delta\nu_D) > \; = \; | \underline{X}_o |^2 / | \underline{X}_o |_W^2 \; ,$$

$$= \; [\int_{-\infty}^{\infty}\int_{-\infty}^{\infty} du'\, du'' \; | \underline{s}_n(u') |^2 \cdot | \underline{s}_n(u'') |^2 \;] \qquad (4.1.47)$$

$$/ \; [\int_{-\infty}^{\infty}\int_{-\infty}^{\infty} du'\, du'' | \underline{s}_n(u') |^2 \cdot | \underline{s}_n(u'') |^2 \; R_{WW}(u'-u'') \;] .$$

Eq. (4.1.47) tells us several things. One, the property of volume-invariance with respect to transmitted waveform is not preserved in the strictest sense because of the presence of R_{WW}. However, for a positive definite, smoothly-varying R_{WW}, as is assumed in our analysis, the $dt\, d\Delta\nu_D$ integral ought to be rather insensitive to the choice of $\underline{s}_n(t)$. Two, the value of the integral is always greater than one - as opposed to exactly one for the ideal case - reflecting the fact that frequency instability has increased the resolution cell size. And three, the manner in which the resolution cell size grows depends directly on the waveform duration and the correlation time of $\underline{w}(t)$.

Before we proceed to the CNR issue, we may comment on the similarity in the resolution loss behavior of RD radar and SAR; in both cases, the relative magnitude of the correlation time t_Θ compared to the coherent integration time - T for CW SAR and T_o for RD radar (cf. Eqs. (3.2.14) and (4.1.38)) - determines the extent of the resolution loss (cf. Eqs. (4.1.16), (4.1.17), and (4.1.41)).

Let us now examine the CNR behavior. The LO shot noise component, as explained in Section 4.1.1, is not affected at all by frequency fluctuation. Thus, the CNR for a RD imager with an

unstable laser differs from that of the stable case only through the target return term $< I_y(t; \nu_D') >$. Thus, we have

$$CNR(t; \nu_D') = (k^2 a_x a_y / 2\pi L^2)^2 P_T \lambda^2 \exp[-2\alpha L] (| \underline{X}_o |_w^2 / | \underline{X}_o |)$$
$$\cdot \int d\bar{s}_o \; \mathcal{J}(\bar{s}_o) < T(\tau, \Delta\nu_D) > / (h\nu_o / \eta).$$

$$(4.1.48)$$

In the limit of large target dimensions, $< I_y(t; \nu_D') >$ may be approximated by using the integral of (4.1.47) [by first converting the $d\bar{s}_o$ integral into a $d\tau d\Delta\nu_D$ integral]. The (approximate) result is

$$CNR(t; \nu_D') \simeq CNR(t; \nu_D', \sigma_f = 0)$$
$$= (P_T \eta / h\nu_o)(k^2 a_x a_y / 2\pi L^2)^2 \exp[-2\alpha L] \; | \underline{X}_o |$$
$$\cdot (c\lambda / \Omega) \; \mathcal{J}_{ave}(t; \nu_D'),$$

$$(4.1.49)$$

where $CNR(t; \nu_D', \sigma_f = 0)$ denotes the CNR in the absence of any frequency instability (cf. Eq. (3.3.19). In other words, for a large target, frequency instability produces little change in CNR. This result may be explained as follows. There are two effects at work. One is that a partial cancellation of the target return during coherent integration decreases the contribution to the output intensity by each point scatterer. The other is that because of reduced resolution, more scatterers contribute to the output at any given time. In the limit of large target dimensions, these two effects counterbalance and as a result, there is little change in the CNR from the perfect stability case.

4.2. Effects of Atmospheric Turbulence

Atmospheric turbulence refers to the phenomenon of spatio-temporal fluctuations of atmosphere's refractive index arising from mixing of air parcels with different temperatures [9,10,38-40]. Atmospheric turbulence can be a very serious problem in coherent laser radar imaging because even a slight temperature fluctuation of the air parcels can have a profound effect on the way optical beams propagate through the atmosphere [9,38,40-43]. Fig. 4.5 illustrates some of the effects atmospheric turbulence and low-visibility (turbid) weather have on beam propagation [44].

For angle-angle imaging, we are usually concerned with beam spreading (divergence of the laser beam beyond the usual diffraction limit) and scintillation (intensity fluctuation) [6,10,11,14]. These problems are still of concern to us in high-resolution imaging, but an even more immediate problem posed by atmospheric turbulence is the loss of target return coherence and the subsequent resolution loss. As will be seen shortly, there are two mechanisms that cause the loss of target return coherence: one, the spatial characteristics of atmospheric turbulence themselves change with time; and two, because of the relative motion between the radar and the target, the return from a given point scatterer propagates through different atmospheric channels over a period of time.

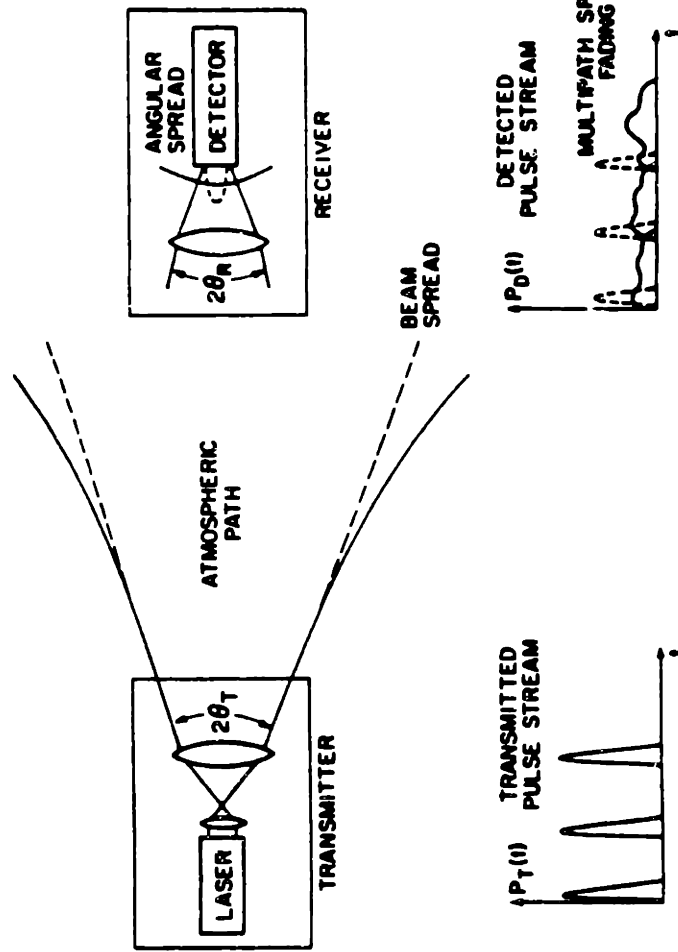It is the objective of this section to characterize the

-133-

Fig. 4.5 Some of the Consequences of Atmospheric Turbulence and
Low-Visibility Weather [44].
Dotted Contours Are Free-Space Behavior of Beam Size,
Receiver Angular Distribution, and Detected Pulse Stream;
Solid Contours Show Behavior in Turbulent, Low-Visibility
Weather Conditions.

performance behavior of our high-resolution imagers when they are subjected to atmospheric turbulence. The section is organized as follows. The first part is devoted to the modelling of atmospheric turbulence, where the notion of atmospheric coherence length plays a key role. Long- and short-range cases are discussed. The second part uses the model developed in the first part to derive the SAR's performance for both small and large aperture cases. Finally, the last part deals with issues of RD imaging in the presence of turbulence.

4.2.1. Atmospheric Turbulence Model

We incorporate the effect of atmospheric turbulence by modifying the existing deterministic Green's function as follows [6]:

$$\underline{h}(\bar{p}',\bar{p},t) = \underline{h}_o(\bar{p}',\bar{p}) \exp[\ \underline{\psi}(\bar{p}',\bar{p},t)\ ]$$
$$= \underline{h}_o(\bar{p}'-\bar{p}) \exp[\chi\ (\bar{p}',\bar{p},t) + j\Phi(\bar{p}',\bar{p},t)\ ],$$

$$(4.2.1)$$

where $\underline{h}_o(\bar{p}'-\bar{p})$ is the Green's function of (2.2.2). $\bar{p}$ and $\bar{p}'$ are transverse coordinates on the source (transmitter) and receiver (target) planes, respectively. $\chi\ (\bar{p}',\bar{p},t)$ and $\Phi(\bar{p}',\bar{p},t)$ are the turbulence-induced log-amplitude and phase terms at time t, respectively, and encompass all the information regarding the atmospheric turbulence, such as the profile of the turbulence layers. Within the region of validity of Rytov's approximation,

χ and Φ can be modelled as jointly Gaussian random processes
[38,42], and we will do so here. Here, we will not concern
ourselves with derivations of various statistics of $\underline{\psi}$ $(\bar{p}',\bar{p},t)$;
rather, we will make use of the results available from the
existing literature.

Realistically speaking, the atmospheric turbulence
distribution is not motionless; rather, it tends to evolve with
time - mainly due to winds and mixing of air parcels. As the
dominant effect in time evolution of the turbulence distribution
is usually the wind-induced translation, we will follow the
Taylor's frozen-flow hypothethis [38] and model the atmospheric
turbulence as a wide-sense stationary (WSS) distribution that
translates as a whole in some transverse direction. For a
stationary radar/stationary target arrangement, we have the
following representation of the model:

$$\exp[\ \chi\ (\bar{p}',\bar{p},t) + j\Phi(\bar{p}',\bar{p},t)\ ]$$
$$= \exp[\ \chi\ (\bar{p}'- \bar{u}t,\ \bar{p} - \bar{u}t) + j\Phi(\bar{p}'- \bar{u}t,\ \bar{p} - \bar{u}t)\ ], \quad (4.2.2)$$

where

$\bar{u}$ = velocity at which the turbulence

distribution moves (wind velocity) $\qquad$ (4.2.3)

$= \hat{x}\ u_x + \hat{y}\ u_y,$

$\left.\begin{array}{c} \chi(\bar{p}',\bar{p}) \\ \\ \Phi(\bar{p}',\bar{p}) \end{array}\right\}$ = turbulence-induced perturbations

$\qquad$ at t = 0. $\qquad\qquad$ (4.2.4)

We will need the mutual coherence function (MCF) of $\exp[\psi(\bar{p}',\bar{p})]$ for future calculations. With the assumption $m_\chi = -\sigma_\chi^2$, which is based on energy conservation requirement [45], where m_χ and σ_χ^2 are the mean and the variance of χ, respectively, we can obtain the following:

$$
\begin{aligned}
&< \exp[\ \psi(\bar{p}'+\bar{p}_2,\ \bar{p}+\bar{p}_1) + \psi^*(\bar{p}',\bar{p})]\ > \\
= \quad &< \exp[\ \chi(\bar{p}'+\bar{p}_2,\ \bar{p}+\bar{p}_1) + j\Phi(\bar{p}'+\bar{p}_2,\ \bar{p}+\bar{p}_1)] \\
&\cdot \exp[\ \chi(\bar{p}',\ \bar{p}) - j\Phi(\bar{p}',\ \bar{p})]\ > \qquad\qquad (4.2.5) \\
= \quad &\exp[-\ D(\bar{p}_2,\ \bar{p}_1)/2],
\end{aligned}
$$

where $D(\bar{p}_2,\ \bar{p}_1)$ is the wave structure function [6,10] defined by

$$
\begin{aligned}
D(\bar{p}_2,\ \bar{p}_1) \equiv\ &< [\ \chi(\bar{p}'+\bar{p}_2,\ \bar{p}+\bar{p}_1) - \chi(\bar{p}',\ \bar{p})]^2\ > \\
&+ < [\ \Phi(\bar{p}'+\bar{p}_2,\ \bar{p}+\bar{p}_1) - \Phi(\bar{p}',\ \bar{p})]^2\ >. \quad (4.2.6)
\end{aligned}
$$

The most often used structure function is based on Kolmogorov - spectrum model [6,40]:

$$
D(\bar{p}_2,\ \bar{p}_1) = 2.91\ k^2 \int_0^L dz\ c_n^2(z)\ (|\bar{p}_2 z + \bar{p}_1(L-z)|/L)^{5/3},
$$
$$(4.2.7)$$

where

$c_n^2(z) =$ turbulence strength profile $[m^{-2/3}]$ between

the transmitter plane at $z = 0$ and the target

plane at $z = L$.

From this, we can obtain the atmospheric coherence length at the transmitter and target planes by setting $\bar{p}_2$ and $\bar{p}_1$ to zero, respectively.

$$D(\bar{0}, \bar{p}_1) = (|\bar{p}_1| / p_o^T)^{5/3}, \qquad (4.2.8)$$

$$\text{and} \quad D(\bar{p}_2, \bar{0}) = (|\bar{p}_2| / p_o^t)^{5/3}, \qquad (4.2.9)$$

where

$p_o^T \equiv$ transmitter-plane coherence length

$$= (2.91 \ k^2 \int_0^L dz \ c_n^2(z) \ |(L-z)/L|^{5/3} \ )^{-3/5}, \qquad (4.2.10)$$

$p_o^t \equiv$ target-plane coherence length

$$= (2.91 \ k^2 \int_0^L dz \ c_n^2(z) \ |z/L|^{5/3} \ )^{-3/5}. \qquad (4.2.11)$$

Physically, significance of the transmitter-plane coherence length lies in that it determines - along with the transmitter aperture size - the extent of beam spreading as the laser beam propagates away from the transmitter. A short coherence length - small compared to the aperture size - leads to an appreciable beam spreading, whereas a long coherence length implies little beam spreading [38]. We will come back to this later in the section.

Because we have previously assumed a Gaussian beam profile for the transmitter beam, for the sake of mathematical convenience, we modify the existing structure function as follows:

$$D(\bar{0}, \bar{p}_1) = [\,|\bar{p}_1| \,/\, p_o^T]^2$$

$$D(\bar{p}_2, \bar{0}) = [\,|\bar{p}_2| \,/\, p_o^t]^2. \qquad (4.2.12)$$

This modification should not change the character of our solution too much so long as only the second-moment calculations (of ψ) are involved. [The square-law approximation does, however, lead to an incorrect result when it is used to calculate the fourth-moments [43], because it gives much too simple a picture of the actual turbulence.]

Next, we calculate the forward propagated transmitter beam and the backpropagated LO beam at the target plane. The forward propagated transmitter beam at the target plane can be expressed in terms of the following transmitter plane integral:

$$
\begin{aligned}
\underline{U}_L(\bar{p},t) &= \int_{z=0} d\bar{p}' \ \underline{U}_T(\bar{p}',t) \ \underline{h}(\bar{p},\bar{p}',t) \\
&= \int_{z=0} d\bar{p}' \ \underline{U}_T^O(\bar{p}'- \bar{p}_R(t)) \ \underline{h}_O(\bar{p} - \bar{p}') \qquad (4.2.13) \\
&\quad \cdot \exp[\psi\ (\bar{p} - \bar{u}t, \bar{p}'- \bar{u}t)],
\end{aligned}
$$

where

$\underline{U}_T^O(\bar{p}')$ = profile of the transmitter beam

$\bar{p}_R(t)$ = nominal transverse coordinates of

the transmitter (radar) at time t

= $(x_R(t), y_R(t))$.

In writing (4.2.13), we have used Eqs. (4.2.1)-(4.2.4). Substituting in the elliptical-Gaussian beam of (3.2.3) for $\underline{U}_T^O(\bar{p}')$ and using the paraxial and far-field approximations, we

arrive at the following:

$$\underline{U}_L(\bar{p},t) = (1/j\ \lambda L)\ \exp[-\alpha L/2]\ \exp[jkL + jk|\bar{p} - \bar{p}_R(t)|^2/2L]$$
$$\cdot\sqrt{2/\pi a_x a_y}\int_{z=0}d\bar{p}'\ \exp[-(x'/a_x)^2 - (y'/a_y)^2]$$
$$\cdot\exp[-j(k/L)\ \bar{p}'\cdot(\bar{p} - \bar{p}_R(t))]$$
$$\cdot\exp[\ \psi(\bar{p} - \bar{u}t,\ \bar{p}' + \bar{p}_R(t) - \bar{u}t)]. \qquad (4.2.14)$$

Similarly, we can write the backpropagated LO beam using the point-reciprocity property of turbulent medium [23] which states that the response registered at some point due to a point source at another is invariant when the locations of the receiver and the source are interchanged.

$$\underline{U}_B^*(\bar{p},t) = (1/j\ \lambda L)\ \exp[-\alpha L/2]\ \exp[jkL + jk|\bar{p} - \bar{p}_R(t)|^2/2L]$$
$$\cdot\sqrt{2/\pi a_x a_y}\int_{z=0}d\bar{p}''\ \exp[-(x''/a_x)^2 - (y''/a_y)^2]$$
$$\cdot\exp[-j(k/L)\ \bar{p}''\cdot(\bar{p} - \bar{p}_R(t))] \qquad (4.2.15)$$
$$\cdot\exp[\ \psi(\bar{p} - (t-2L/c)\bar{u},\ \bar{p}'' + \bar{p}_R(t-2L/c) - (t-2L/c)\bar{u}]$$

We have assumed, as we have been, that the LO beam pattern at the transmitter plane is matched to the transmitter beam pattern. The $2L/c$ time delay in the arguments of ψ is to account for the change in the turbulence distribution (due to wind) during the time the transmitter beam has propagated to the target and back to the radar.

The complex envelope of the target return is then given by

$$\underline{y}(t) = \int_{z=L} d\bar{p}\ \underline{T}(\bar{p})\ \underline{s}(t-2L/c)\ \underline{U}_L(\bar{p},t)\ \underline{U}_B^*(\bar{p},t)$$

$$= (2/\pi a_x a_y)(1/j\lambda L)^2\ \exp[2jkL - \alpha L] \qquad (4.2.16)$$

$$\cdot \int_{z=L} d\bar{p}\ \underline{T}(\bar{p})\ \underline{s}(t-2L/c)\ \exp[jk|\bar{p} - \bar{p}_R(t)|^2/L]\ \underline{F}(\bar{p},t),$$

where

$$\underline{F}(\bar{p},t) = \iint_{z=0} d\bar{p}'d\bar{p}''\quad \exp[-(x'/a_x)^2 - (y'/a_y)^2]$$

$$\cdot \exp[-j(k/L)\ \bar{p}'\cdot(\bar{p} - \bar{p}_R(t))]$$

$$\cdot \exp[-(x''/a_x)^2 - (y''/a_y)^2] \qquad (4.2.17)$$

$$\cdot \exp[-j(k/L)\ \bar{p}''\cdot(\bar{p} - \bar{p}_R(t))]$$

$$\cdot \exp[\ \underline{\psi}\ (\bar{p} - \bar{u}t,\ \bar{p}' + \bar{p}_R(t) - \bar{u}t)]$$

$$\cdot \exp[\ \underline{\psi}\ (\bar{p} - (t-2L/c)\bar{u}\ ,$$

$$\bar{p}'' + \bar{p}_R(t-2L/c) - (t-2L/c)\bar{u})].$$

The corresponding $< I_y(t) > (\ = <|\ \underline{1}_y(t)|^2 >$

$= <|\ \underline{y}(t) \star \underline{h}(t)|^2 >)$ is

$$< I_y(t) > = (2/\pi a_x a_y)^2(1/\lambda L)^4\ \exp[-2\alpha L]$$

$$\cdot \int_{z=L} d\bar{p}\ \lambda^2\ \mathcal{T}(\bar{p})\ \iint d\tau'd\tau''\ \underline{h}(t-\tau')\ \underline{s}(\tau'-2L/c)$$

$$\cdot\ \underline{h}^*(t-\tau'')\ \underline{s}^*(\tau''-2L/c)\ \exp[jk|\bar{p} - \bar{p}_R(\tau')|^2/L]$$

$$\cdot\ \exp[-jk|\bar{p} - \bar{p}_R(\tau'')|^2/L]\ 4 \qquad (4.2.18)$$

$$\cdot\ < \underline{F}(\bar{p},\tau')\ \underline{F}^*(\bar{p},\tau'') >.$$

The quantity $< \underline{F}(\bar{p},\tau')\ \underline{F}^*(\bar{p},\tau'') >$ is rather difficult to compute
for general cases because of the MCF calculation: in general the
fourth moment of $\underline{\psi}$ cannot be obtained in closed form [38,43].
In some special cases, however, the calculation may be
simplified. We now introduce two such limiting cases with which

we will be dealing.

The first is termed the short-range case. Here, the range is assumed to be short enough so that the combined displacement of the radar or the target and the turbulence distribution during the roundtrip time 2L/c is negligible compared to the appropriate atmospheric coherence length (either the transmitter-plane or the target-plane coherence length depending on the imaging configuration). This means that the transmitted beam and the scattered beam may be treated as though they were propagating through the same atmospheric channel. The opposite limit, which is our second case, is called the long-range case. Here, the range is assumed to be sufficiently long so that the transmitted beam and the scattered beam (from the target) effectively propagate through statistically independent atmospheric channels.

Commensurate with the assumption above, we drop the 2L/c dependence from $\underline{\psi}$ for the short-range case. The result is

$$
< \underline{F}(\bar{p},\tau') \; \underline{F}^*(\bar{p},\tau'') >
$$

$$
= \iiiint_{z=0} d\bar{p}_1 d\bar{p}_2 d\bar{p}_3 d\bar{p}_4 \; \{ \prod_{i=1}^{4} \exp[-(x_i/a_x)^2 - (y_i/a_y)^2] \}
$$

$$
\cdot \exp[-j(k/L)[(\bar{p} - \bar{p}_R(\tau'))\cdot(\bar{p}_1 + \bar{p}_2) - (\bar{p} - \bar{p}_R(\tau''))\cdot(\bar{p}_3 + \bar{p}_4)]]
$$

$$
\cdot < \exp[\; \underline{\psi}(\bar{p} - \bar{u}\tau', \; \bar{p}_1 + \bar{p}_R(\tau') - \bar{u}\tau')
$$

$$
+ \; \underline{\psi}(\bar{p} - \bar{u}\tau', \; \bar{p}_2 + \bar{p}_R(\tau') - \bar{u}\tau') \qquad\qquad (4.2.19)
$$

$$
+ \; \underline{\psi}^*(\bar{p} - \bar{u}\tau'', \; \bar{p}_3 + \bar{p}_R(\tau'') - \bar{u}\tau'')
$$

$$
+ \; \underline{\psi}^*(\bar{p} - \bar{u}\tau'', \; \bar{p}_4 + \bar{p}_R(\tau'') - \bar{u}\tau'') \;] >.
$$

This is still a formidable calculation. If we further assume a

small transmitter aperture, i.e., a transmitter beam whose dimensions are much smaller than the transmitter-plane coherence length, then the calculation becomes more manageable. Based on the earlier comment about the relationship between beam spreading and the aperture size, this small aperture assumption then implies negligible beam spreading. Bringing the fourth moment expectation term outside the integrals by setting $\bar{p}_1 = \bar{p}_2 = \bar{p}_3 = \bar{p}_4 = \bar{0}$ in the arguments of $\underline{\Psi}$, we obtain the small aperture result

$$< \underline{F}(\bar{p},\tau')\ \underline{F}^*(\bar{p},\tau'') >$$

$$= < \exp[2\underline{\psi}\ (\bar{p} - \bar{u}\tau',\ \bar{p}_R(\tau')-\bar{u}\tau') + 2\ \underline{\psi}^*(\bar{p} - \bar{u}\tau'',\ \bar{p}_R(\tau'')-\bar{u}\tau'')] >$$

$$\cdot (\pi a_x a_y)^4 \exp[-2(ka_x(x-x_R(\tau'))/2L)^2 - 2(ka_y(y-y_R(\tau'))/2L)^2]$$

$$\cdot \exp[-2(ka_x(x-x_R(\tau''))/2L)^2 - 2(ka_y(y-y_R(\tau''))/2L)^2],$$

$$(4.2.20)$$

where the expectation term can be evaluated using the Gaussian property of $\chi(\bar{p})$ and $\phi(\bar{p})$, the assumption of $m_\chi = -\sigma_\chi^2$, and Eq. (4.2.5):

$$< \exp[2\underline{\psi}\ (\bar{p} - \bar{u}\tau',\ \bar{p}_R(\tau')-\bar{u}\tau') + 2\ \underline{\psi}^*(\bar{p} - \bar{u}\tau'',\ \bar{p}_R(\tau'')-\bar{u}\tau'')] >$$

$$= \exp[4\sigma_\chi^2]\ \exp[-2D((\tau''-\tau')\bar{u},\ \bar{p}_R(\tau') - \bar{p}_R(\tau'') + (\tau'' - \tau')\bar{u})\ ].$$

$$(4.2.21)$$

In particular, if there is no turbulence motion, i.e., when $\bar{u} = \bar{0}$, the above reduces to

$$< \exp[2\,\underline{\psi}(\bar{p},\ \bar{p}_R(\tau')) + 2\underline{\psi}^*(\bar{p},\ \bar{p}_R(\tau''))] >$$

$$= \exp[4\sigma_\chi^2]\ \exp[-2D(\bar{0},\ \bar{p}_R(\tau') - \bar{p}_R(\tau''))\ ] \qquad (4.2.22)$$

$$= \exp[4\sigma_\chi^2]\ \exp[-2|\bar{p}_R(\tau') - \bar{p}_R(\tau'')|^2/\ (p_o^T)^2\ ],$$

where we have used (4.2.12) in the second step.

Let us now compute $< \underline{F}(\bar{p},\tau')\ \underline{F}^*(\bar{p},\tau'') >$ for the long-range case. In this case, we can write

$$< \underline{F}(\bar{p},\tau')\ \underline{F}^*(\bar{p},\tau'') >$$

$$= \iiint_{z=0} d\bar{p}_1 d\bar{p}_2 d\bar{p}_3 d\bar{p}_4\ \{ \prod_{i=1}^{4} \exp[-(x_i/a_x)^2 - (y_i/a_y)^2]\ \}$$

$$\cdot \exp[-j(k/L)[(\bar{p} - \bar{p}_R(\tau'))\cdot(\bar{p}_1 + \bar{p}_2) - (\bar{p} - \bar{p}_R(\tau''))\cdot(\bar{p}_3 + \bar{p}_4)]]$$

$$\cdot < \exp[\ \psi(\bar{p} - \bar{u}\tau',\ \bar{p}_1 + \bar{p}_R(\tau') - \bar{u}\tau')$$

$$+ \psi^*(\bar{p} - \bar{u}\tau'',\ \bar{p}_3 + \bar{p}_R(\tau'') - \bar{u}\tau'')] >$$

$$\cdot < \exp[\ \psi(\bar{p} - \bar{u}\tau',\ \bar{p}_2 + \bar{p}_R(\tau') - \bar{u}\tau') \qquad (4.2.23)$$

$$+ \psi^*(\bar{p} - \bar{u}\tau'',\ \bar{p}_4 + \bar{p}_R(\tau'') - \bar{u}\tau'')] >,$$

where expressing the overall average as a product of two averages is made possible via the assumption of independence between the forward and backpropagated beams for the long-range case. Physically, these averages represent the correlation between the forward propagated beams and the the correlation between the backpropagated beams, respectively. The expectation terms can be written, once again using (4.2.5), as

$$\exp[-(1/2)\cdot D((\tau''-\tau')\bar{u},\ \bar{p}_1 - \bar{p}_3 + \bar{p}_R(\tau') - \bar{p}_R(\tau'') + (\tau''-\tau')\bar{u})]$$

$$\cdot \exp[-(1/2)\cdot D((\tau''-\tau')\bar{u},\ \bar{p}_2 - \bar{p}_4 + \bar{p}_R(\tau') - \bar{p}_R(\tau'') + (\tau''-\tau')\bar{u})].$$

$$(4.2.24)$$

Note that in the long-range case, the integral in (4.2.23) can be evaluated without having to assume a small aperture. In the small aperture limit, however, (4.2.23) does reduce to the short-range small aperture result of (4.2.20) and (4.2.21) except for the missing factor of two in front of the structure function and the absence of the $\exp[4\sigma_\chi^2]$ term.

4.2.2. SAR

In this section, we examine the performance of SAR in a turbulent atmosphere. We will explore both the short- and long-range cases discussed in the previous section.

In the earlier analysis on the effects of frequency instability (cf. Section 4.1), we learned that a 2D SAR's cross-track resolution is much less prone to degradation from reduced target return temporal coherence than is its along-track resolution. Since propagation through turbulent atmosphere can be viewed - at least to the lowest order - as a process that introduces yet another form of phase fluctuation to the target return, we can then expect the 2D SAR's cross-track resolution to be weakly influenced by the turbulence as well. Consequently, we shall limit our analysis to CW SAR in this section.

Let us first consider the short-range, small transmitter aperture case. Using Eqs. (4.2.18), (4.2.20), and (4.2.21), we can write $< I_y(t) >$ as follows:

$$
\begin{aligned}
< I_y(t) > = \ & (2/\pi a_x a_y)^2 (1/\lambda L)^4 \exp[-2\alpha L] \\
& \cdot \int d\bar{p}\ \lambda^2\ \mathcal{J}(\bar{p})\ \iint d\tau' d\tau''\ \underline{h}(t-\tau')\ \underline{s}(\tau'-2L/c) \\
& \quad \cdot\ \underline{h}^*(t-\tau'')\ \underline{s}^*(\tau''-2L/c) \\
& \cdot\ \exp[j(k/L)|\bar{p} - \hat{x}\ v\tau'|^2 - j(k/L)|\bar{p} - \hat{x}\ v\tau''|^2] \\
& \cdot\ < \underline{F}(\bar{p},\tau')\ \underline{F}^*(\bar{p},\tau'') >,
\end{aligned}
\tag{4.2.25}
$$

with $z = L$.

where

$$\underline{h}(t) = \exp[-j(kv^2/L)t^2 - 2(ka_x v/2L)^2 t^2],$$

$$[\text{from } (3.2.6) \text{ and } (3.2.14)]$$

$$\underline{s}(t) = \sqrt{P_T} ,$$

$$\bar{p}_R(t) = (vt,0),$$

and

$$< \underline{F}(\bar{p},\tau') \ \underline{F}^*(\bar{p},\tau") > = (\pi a_x a_y)^4 \ \exp[4\sigma_x^2]$$

$$\cdot \exp[-2(ka_x/2L)^2((x-v\tau')^2 + (x-v\tau")^2)]$$

$$\cdot \exp[-(ka_y/L)^2 y^2]$$

$$\cdot \exp[-2D((\tau"-\tau')\bar{u},(\bar{u} -\hat{x} v)(\tau"-\tau'))].$$

$$(4.2.26)$$

Note that we have let $\bar{p}_R(t) = (vt, 0)$ to indicate that the radar is moving with velocity $\hat{x} v$ in the SAR configuration. Using the square-law version of structure function (4.2.7), we obtain

$$D(\bar{u} \Delta\tau,(\bar{u} - \hat{x} v)\Delta \tau) = 2.91 \ k^2 \int_0^L dz \ C_n^2(z)$$

$$\cdot [|(\bar{u} \Delta\tau)z + (\bar{u} - \hat{x} v) \ \Delta\tau(L-z)|/L]^{5/3},$$

$$\simeq (2 \Delta \tau/t_o)^2, \qquad (4.2.27)$$

where

$$\Delta \tau = \tau" - \tau'$$

$$t_o \equiv 2[2.91 \ k^2 \int_0^L dz \ C_n^2(z) [|\bar{u}L - \hat{x} v(L-z)|/L]^{5/3}]^{-3/5}.$$

$$(4.2.28)$$

As far as the SAR application is concerned, we may consider t_o and vt_o as the effective (atmospheric) coherence time and coherence length, respectively. Note from (4.2.28) that both the radar's motion and the motion of the turbulence distribution

contribute to the decorrelation of the target return over time.

From a quick glance at (4.2.28), we see that a codirectional motion of the turbulence and the radar, i.e. the turbulence moving in the same direction as the radar, results in a longer coherence time t_o. This is because when the radar is moving in the same direction as the frozen turbulence, the latter motion partially compensates for some of the former, allowing the laser beam from the radar to "see" the same atmospheric propagation channel for a longer period of time. However, even in the event that $\bar{u} \simeq \hat{x} v$, the effective coherence time has an upper bound because the target is stationary and cannot negate the effects of the radar and the turbulence motion (see Fig. 4.6). As a result, the effective coherence length in that case is the usual target-plane coherence length given by (4.2.11).

By similar reasoning, if the turbulence motion and the radar motion are in the opposite direction, it is easy to see that the coherence time will decrease compared to the stationary (frozen) turbulence case.

At this point, it is clear that there is a great deal of similarity between the frequency instability case and this atmospheric turbulence case from a mathematical standpoint, even though the physical origins of frequency instability and atmospheric turbulence are unrelated. Recall that in the frequency instability analysis, the effect of laser frequency jitter was lumped into the correlation term $R_{ww}(\tau) = < \underline{w}(t+\tau) \underline{w}^*(t) >$ which, for medium- and long-range cases (cf. (4.1.5),

RADAR $\longrightarrow$ $\hat{x}$ v

TURBULENCE $\longrightarrow$ $\bar{u} \approx \hat{x}$ v

STATIONARY TARGET

$\Updownarrow$ EQUIVALENT

RADAR

TURBULENCE   }   STATIONARY

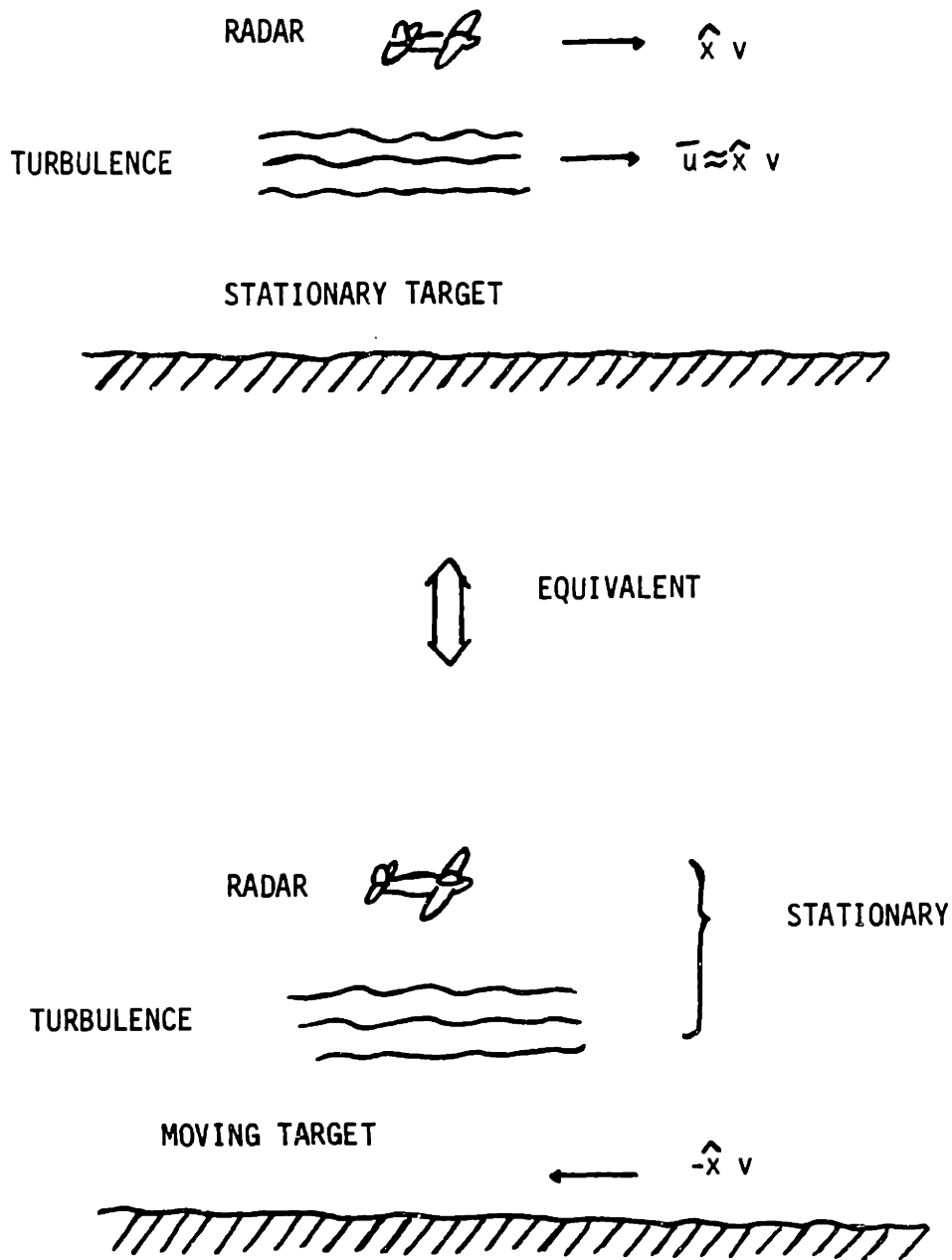MOVING TARGET

$\longleftarrow$ $-\hat{x}$ v

Fig. 4.6   Equivalent Ways of Viewing the Moving Turbulence/
Moving Radar Problem when $\bar{u} \approx \hat{x}$ v

(4.1.6)), is given by $\exp[-8(\tau/t_\Theta)^2]$, t_Θ being the
characteristic correlation time in each case. In the atmospheric
turbulence analysis of the small aperture, short-range case [note
that the short-range case here is different from the short-range
case of the frequency instability section], $\exp[-8(\tau/t_0)^2]$ and t_0
fill the respective roles of R_{ww} and t_Θ for the frequency
instability analysis. Thus, we can readily make use of the
results from the frequency instability analysis, by adding the
$\exp[4\sigma_\chi^2]$ factor and replacing t_Θ by t_0.

We write down the expression for $< I_y(t) >$ with the aid of
Eqs. (4.1.9) and (4.1.14)-(4.1.16).

$$< I_y(t) > = (P_T \pi a_x a_y \lambda /2\sqrt{2} \, Lv^2) \, \exp[-2\alpha L] \, \exp[4\sigma_\chi^2]$$
$$\cdot (4/\pi y_{res}^2)^{1/2} \int_{z=L} d\bar{p} \; \mathcal{J}(\bar{p}) \; g_x(x-vt) \; g_y(y), \quad (4.2.29)$$

where

$$g_x(x) = (1/\epsilon)(4/\pi x_{res}^2)^{1/2} \exp[-2(ka_x/2L)^2] \exp[-2(x/\epsilon a_x)^2],$$
$$g_y(y) = \exp[-(2y/y_{res})^2],$$
$$\epsilon \equiv [1 + (T/t_0)^2]^{1/2}, \quad (4.2.30)$$

x_{res}, y_{res} = x- and y-resolutions in the absence of
atmospheric turbulence (cf. Eq. (3.2.14)).

Surveying this result, we see once again that the key quantity in
determining the along-track resolution loss is the ratio of the
coherent integration time T over the characteristic correlation
time of the perturbation, in this case t_0. As the atmospheric
turbulence increases, target returns received at different times

from the same point scatterer become increasingly uncorrelated, having gone through atmospheric channels which become more uncorrelated. This loss of temporal coherence in the target return interferes with the focussing action of the IF filter, thereby reducing the along-track resolution. The upper bound on the along-track resolution, as before, is set by the beamwidth on the target, which, for our small aperture regime, is essentially unchanged from the ideal case.

The cross-track resolution, unlike the along-track resolution, is unaffected by atmospheric turbulence - at least for the small aperture limit. The translational motion of the turbulence, uniform in our model, becomes coupled only to the along-track coordinate via IF filtering and has no effect on the cross-track coordinate. As we shall see in the large aperture analysis, cross-track resolution loss depends mainly on the extent of beam spreading.

As turbulence cannot affect the LO beam power that falls on the surface of a photodetector, the average intensity of the LO shot noise component $< I_n(t) >$ is same as in the ideal case (cf. (3.2.16)). It then follows that

$$CNR_{CW\ SAR}(C_n^2 \neq 0) = CNR_{CW\ SAR}(C_n^2 = 0) \cdot \varepsilon_{turb},$$

where
(4.2.31)

$$CNR_{CW\ SAR}(C_n^2 = 0) = \text{CNR for no-turbulence situation},$$

$$\varepsilon_{turb} = \text{CNR-loss factor due to turbulence}$$

$$= \exp[4\sigma_\chi^2] / [1 + (ka_x^2/2L)^2 \cdot \varepsilon^2]^{1/2}$$

ε = resolution loss factor of (4.2.30),

for the small aperture, short-range case. Except for the exponential factor in its numerator, ε_{turb} has exactly same form as its counterpart for the frequency instability result (cf. (4.1.19)), and can be explained in the following manner. The atmospheric turbulence, coupled with the radar's motion, reduces the temporal coherence of the target return, which in turn increases the target return bandwidth. This directly translates into less signal energy being passed through the IF filter and thus a lower CNR. However, as in the frequency instability case, SAR suffers little CNR loss from atmospheric turbulence in the vicinity of the resolution breakpoint. $\exp[4\sigma_\chi^2]$ is a consequence of the atmospheric turbulence model we have adopted and, for weak turbulence [$\sigma_\chi^2 \ll 1$], is negligible [6].

We now discuss the long-range case. We begin by reproducing the results of (4.2.23) and (4.2.24) for $< \underline{F}(\bar{p},\tau') \ \underline{F}^*(\bar{p},\tau ") >$ for reference purposes.

$$
\begin{aligned}
< \underline{F}&(\bar{p},\tau') \ \underline{F}^*(\bar{p},\tau") > \\
&= \iiiint_{z=0} d\bar{p}_1 d\bar{p}_2 d\bar{p}_3 d\bar{p}_4 \ \{ \ \overset{4}{\underset{i=1}{\pi}} \exp[-(x_i/a_x)^2 - (y_i/a_y)^2] \ \} \\
&\cdot \exp[-j(k/L)[(\bar{p} - \hat{x} v\tau')\cdot(\bar{p}_1 + \bar{p}_2) - (\bar{p} - \hat{x} v\tau")\cdot(\bar{p}_3 + \bar{p}_4)]] \\
&\cdot \exp[-(1/2) \ D(\ \bar{u}\Delta\tau, \ \bar{p}_1 - \bar{p}_3 + \Delta\tau(\bar{u} - \hat{x} v))] \\
&\cdot \exp[-(1/2) \ D(\ \bar{u}\Delta\tau, \ \bar{p}_2 - \bar{p}_4 + \Delta\tau(\bar{u} - \hat{x} v))]. \qquad (4.2.32)
\end{aligned}
$$

Let us first look at the small aperture limit. In this limit, we

may set $\bar{p}_1$, $\bar{p}_2$, $\bar{p}_3$, $\bar{p}_4 = \bar{0}$ inside the structure functions. The result is

$$
\begin{aligned}
< \underline{F}(\bar{p},\tau') \ \underline{F}^*(\bar{p},\tau") > = (\pi a_x a_y)^4 \ &\exp[-(k\hat{a}_y/L)^2 y^2] \\
&\cdot\exp[-2(ka_x/2L)^2((x-v\tau')^2+(x-v\tau")^2)] \\
&\cdot\exp[-D(\bar{u}_{\Delta}\tau,(\bar{u}-\hat{x}\,v)_{\Delta}\,\tau)],
\end{aligned}
$$

$$(4.2.33)$$

which is identical to (4.2.26) except for the exponential involving the structure function D: here, we have exp[-D] instead of exp[-2D].

This change in correlation function can be accounted for as follows. Because the transmitted and scattered beams travel through essentially independent atmospheric paths for the long-range case, the total mean-squared atmospheric fluctuation encountered by them is the sum of the mean-squared fluctuations encountered by each beam. For the short-range case, on the other hand, the transmitted and scattered beams are assumed to be completely correlated and as a result, the total mean-squared fluctuation encountered is four times the mean-squared fluctuation encountered in one-way propagation, thus the factor of two difference between the two cases.

An immediate consequence of this difference between the short-range and long-range correlations is that the expression for the effective coherence time t_o for the long-range case picks up a factor of $\sqrt{2}$.

We now examine the general case of arbitrarily large aperture. We will neglect the motion of the turbulence distribution for this analysis since it is likely to be negligible compared to the radar motion in most situations. This approximation will simplify the mathematics considerably without sacrificing much generality.

Under this approximation (setting $\bar{u} = \bar{0}$), the structure function is given by

$$D(\bar{0}, \Delta\bar{p} - \hat{x} \, v \, \Delta\tau) = |\Delta\bar{p} - \hat{x} \, v \, \Delta\tau|^2 / (p_o^T)^2, \qquad (4.2.34)$$

where

$$\Delta\bar{p} = \bar{p}_1 - \bar{p}_3 \text{ or } \bar{p}_2 - \bar{p}_4$$

p_o^T = transmitter-plane coherence length given by (4.2.10). [From now, we will drop the superscript T from p_o^T.] With (4.2.34) as the structure function, $< \underline{F}(\bar{p},\tau') \, \underline{F}^*(\bar{p},\tau") >$ of (4.2.32) can be evaluated as follows (see Appendix B for the calculation):

$$
\begin{aligned}
< \underline{F}(\bar{p},\tau') \, \underline{F}^*(\bar{p},\tau") > &= (\pi a_x a_y)^4 (1/\mu_x^2\mu_y^2) \\
&\quad \cdot \exp[-(v \, \Delta\tau)^2\{(ka_x/2L)^2 + (1/p_o\mu_x)^2\}] \\
&\quad \cdot \exp[-2j \, \Delta\tau(kv/L)(a_x/\mu_x p_o)^2(x - v\tau_s)] \\
&\quad \cdot \exp[-(ka_x/\mu_x L)^2(x - v\tau_s)^2] \\
&\quad \cdot \exp[-(ka_y/\mu_y L)^2 y^2],
\end{aligned}
$$

where $\hspace{8cm}$ (4.2.35)

$$
\begin{aligned}
\mu_x^2 &\equiv 1 + (a_x/p_o)^2 \\
\mu_y^2 &\equiv 1 + (a_y/p_o)^2 \\
\tau_s &\equiv (\tau' + \tau")/2.
\end{aligned}
$$

$\hspace{13cm}$ (4.2.36)

Looking at the expression for $< \underline{F}(\bar{p},\tau') \; \underline{F}^*(\bar{p},\tau") >$ above, we see that the effects of the atmospheric turbulence, guised under the p_0 and μ_x, μ_y terms, are evident in several places. A particularly interesting feature is the emergence of μ_x and μ_y, which is a direct consequence of relaxing the small aperture assumption. These factors account for the beam spreading in the x- and y-directions, respectively, due to turbulence; this is verified by the last two exponentials of (4.2.35) which give the beam pattern on the target.

In the small aperture limit (or equivalently large coherence length limit), where a_x/p_0, $a_y/p_0 \ll 1$ and μ_x, $\mu_y \longrightarrow 1$, there is little beam spreading and (4.2.35) reduces to the small aperture result of (4.2.33) (with $\bar{u} = \bar{0}$, of course). On the other hand, if the turbulence is severe enough or aperture large enough so that a_x/p_0, $a_y/p_0 \gtrsim 1$, then significant beam spreading occurs, with the beam size on the target determined largely by the coherence length.

The computation of $< I_y(t) >$ is carried out in the Appendix C. The result is

$$
\begin{aligned}
< I_y(t) > = \; & (\sqrt{2} \; \pi a_y^2/v^2 L^2) \; P_T \exp[-2\alpha L] \\
& \cdot (1/\mu_x^2 \mu_y^2) \; (\mu_x^2/(1 + \mu_x^2))^{1/2} \; (1/\eta_1) \\
& \cdot \int_{z=L} d\bar{p} \; \mathcal{J}(\bar{p}) \; \exp[-(ka_y/\mu_y L)^2 y^2] \\
& \cdot \exp[-(ka_x/L)^2 (x-vt)^2/(1 + \mu_x^2)] \\
& \cdot \exp[-2(x-vt)^2/(\eta_2 a_x)^2],
\end{aligned}
\tag{4.2.37}
$$

where

$$\eta_1 \equiv [1 + 2(L/ka_x p_o \mu_x)^2 + 2(L/kp_o^2 \mu_x)^2/(1 + \mu_x^2)]^{1/2},$$

$$\eta_2 \equiv \eta_1/(1 - (a_x/p_o)^2/(1 + \mu_x^2)). \tag{4.2.38}$$

Since we already know the small aperture behavior, let us now explore the other limiting case, the large aperture limit, where $a_x, a_y \gg p_o$ prevails. In the large aperture limit,

$$\mu_x \simeq a_x/p_o,$$

$$\mu_y \simeq a_y/p_o, \tag{4.2.39}$$

$$\eta_1 \simeq 2L/ka_x^2,$$

$$\eta_2 \simeq 2L/kp_o^2, \tag{4.2.40}$$

and

$$< I_y(t) > \simeq (\sqrt{2} \, \pi a_y^2/v^2 L^2) \, P_T \exp[-2\alpha L] \, (p_o^2/a_x a_y)^2 (ka_x^2/2L)$$

$$\cdot \int d\bar{p} \, \mathcal{J}(\bar{p}) \, \exp[-(kp_o/L)^2 y^2] \tag{4.2.41}$$

$$\cdot \exp_{z=L}[-(kp_o/L)^2(1 + 4(p_o/a_x)^2) \, (x-vt)^2].$$

From (4.2.41), we see that the focussing action of the SAR processor is completely undermined by the turbulence in this limit, and the spatial resolutions are essentially determined by the beam size on the target, which are dictated by the coherence length p_o instead of the transmitter beam size. The along- and cross-track resolutions are:

$$x_{res} \sim 2L/kp_o,$$

$$y_{res} \sim 2L/kp_o, \qquad\qquad (4.2.42)$$

respectively. This complete breakdown of the coherent processing is to be expected: the processing requires a temporal coherence (of the target return) on the order of $\lambda L/a_x v$ - or equivalently a spatial coherence of $\lambda L/ a_x$ - but in the large aperture limit, the coherence length is already much smaller than the aperture size, which in turn is much smaller than $\lambda L/a_x$. Fig. 4.7 shows the spatial resolution in the long-range case as a function of the coherence length p_o for a fixed range L.

The CNR for the large aperture limit can be obtained by combining (4.2.41) with (3.2.16), with the result

$$CNR_{CW\ SAR}(C_n^2 \neq 0) \simeq (P_T p_o^2 a_x\ \eta/vL^2 h\nu_0\ \sqrt{\pi^3/2}\ \exp[-2\alpha L] \mathcal{J}_{ave}(vt)$$

$$= CNR_{CW\ SAR}(C_n^2=0)\cdot\varepsilon_{turb} \qquad (4.2.43)$$

where

$CNR_{CW\ SAR}(C_n^2=0)$ = CNR for the ideal case (see (3.2.17)),

ε_{turb} = CNR loss factor

$\simeq 2(p_o/a_x)\cdot(p_o/a_y) \qquad (4.2.44)$

$\mathcal{J}_{ave}(vt)$ = spatial average of $\mathcal{J}(\bar{p})$ over a resolution cell centered at (vt,0).

As $a_x, a_y \gg p_o$ in the large aperture limit, the CNR loss is quite large. CNR in the long-range case is sketched as a function of p_o in Fig. 4.8 for a fixed range L.
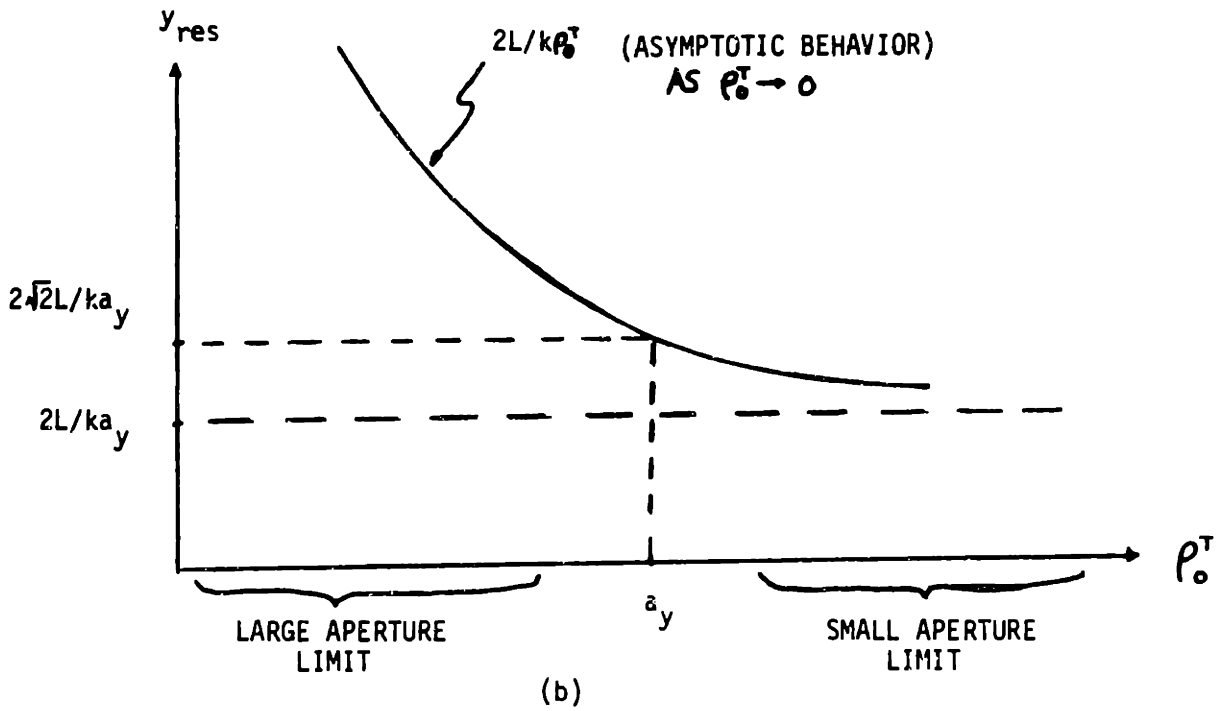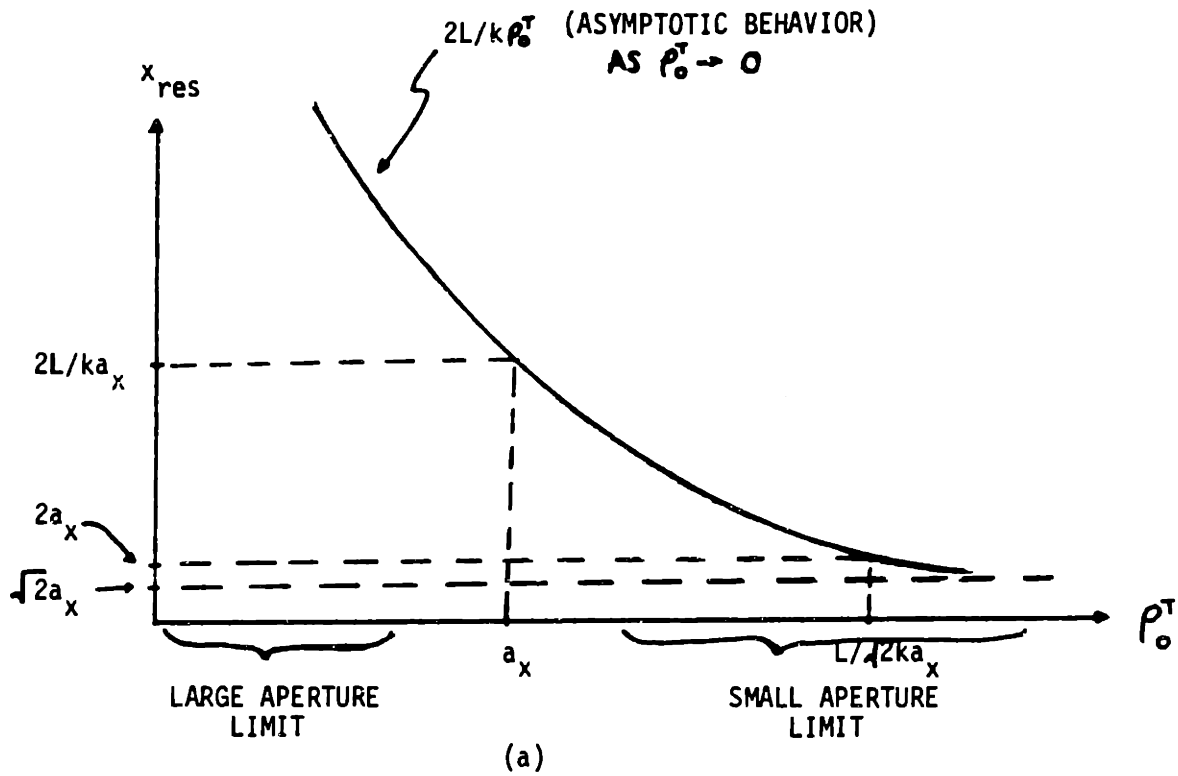
Fig. 4.7 CW SAR's Spatial Resolutions x_{res}, y_{res} vs. Transmitter-Plane Coherence Length ρ_o^T for the Long-Range Case (for a Fixed Range L)
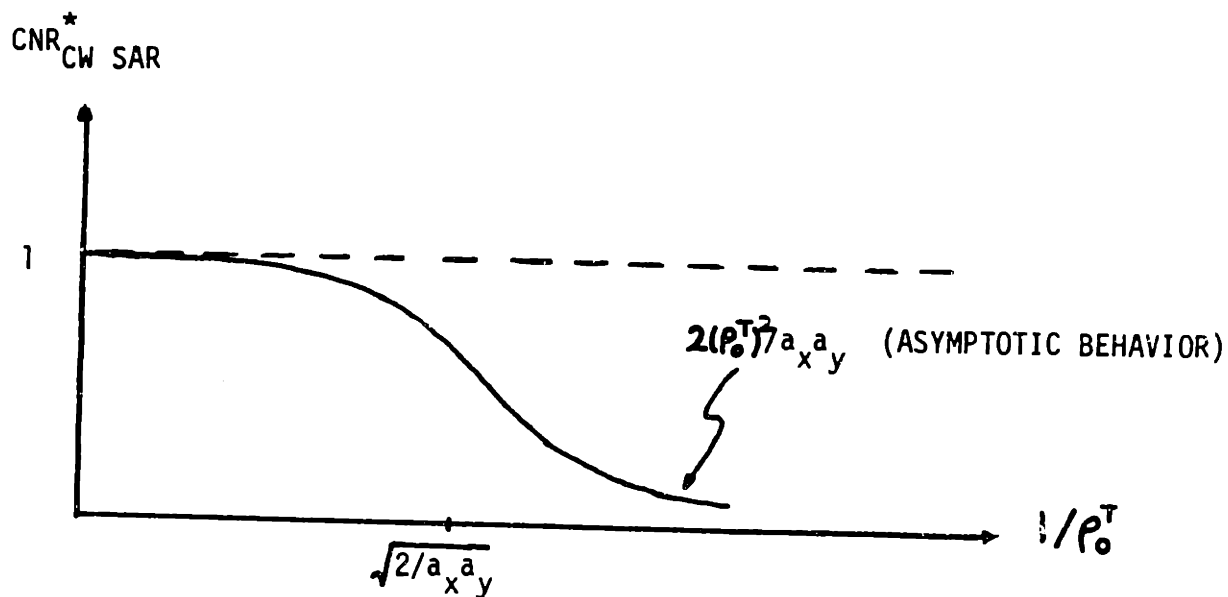
Fig. 4.8 CW SAR's Normalized CNR, $\text{CNR}^*_{\text{CW SAR}}$, vs. Transmitter-Plane
Coherence Length ρ^T_o for the Long-Range Case
(for a Fixed Range L)

$$\text{CNR}^*_{\text{CW SAR}} = \text{CNR}_{\text{CW SAR}}(C^2_n \neq 0)/\text{CNR}_{\text{CW SAR}}(C^2_n = 0)$$

Two loss mechanisms are at work behind this large aperture CNR behavior, both of which can be attributed to beam spreading. One of them is broadening of the target return spectrum, which gives rise to the loss associated with the along-track direction (p_o/a_x). Because the effective beamwidth on the target in the x-direction is much larger in the large aperture limit than in the diffraction-limited case ($\sim \lambda L/p_o$ vs. $\sim \lambda L/a_x$), the return (Doppler) bandwidth generated by the translational motion of the radar is also much greater ($\sim v/p_o$ vs. $\sim v/a_x$). As a result, only a small fraction of the energy originally present in the target return remains after IF filtering [recall that the CW SAR receiver bandwidth is only $\sim v/a_x$], which leads to a decrease in CNR.

The other CNR loss mechanism has to do with the decrease in heterodyne mixing efficiency. Physically, atmospheric turbulence distorts the wavefront of the scattered beam entering the receiver optics, and if there is a sufficient mismatch between the LO beam pattern and the beam pattern of the target return beam due to atmospheric distortion, a significant CNR loss can occur.

To explain the second CNR loss mechanism in another (more mathematical) way, we deduce that the residual CNR loss, the loss remaining after the loss associated with the along-track direction has been accounted for, must be connected in some way to the cross-track direction. Since IF filtering does not affect the cross-track resolution, the CNR loss associated with the

cross-track direction (p_0/a_y) can be seen directly from the overlap integral of the forward propagated transmitter beam and the backpropagated LO beam on the target plane. It turns out that the value of the overlap integral, for a fixed transmitted power, falls off linearly with increasing beam size on the (spatially resolved) target [47], and so, beam spreading leads to CNR loss in this manner as well.

In summarizing the CW SAR's CNR behavior, we have shown that beam spreading is the cause of CNR loss. This conclusion, supported by both the small and large aperture results, is consistent with the findings of a similar analysis on conventional angle-angle imagers [In fact, Eq. (4.2.44) is equal to the CNR loss factor expression given in [47] for the large aperture limit of conventional angle-angle imaging scenario].

This concludes our analysis on the effects of atmospheric turbulence on SAR performance. Obviously, the extent to which turbulence actually degrades the system performance will depend on the imaging configuration and the turbulence profile. We will provide some sample calculations in Chapter V.

4.2.3. RD Radar

This short section addresses issues that are relevant to RD imaging in the presence of atmospheric turbulence. There is a great deal of similarity in how turbulence affects RD imaging and SAR imaging. Thus, we will not dwell on the commonalities, but rather, we shall focus on the differences. Along the same vein, to avoid redundancy arising from two types of RD imaging, we shall limit our discussion to the Type A (cf. Section 3.3.1) processor.

The fundamental difference in how turbulence impacts SAR and RD imaging arises from motion: in SAR imaging the radar is in motion, whereas in RD imaging the target is moving. Therefore, two factors which reduce the target return coherence in the RD case are the movement of the turbulence distribution and the rotation of the target. This is in contrast to the SAR case, where the radar's translational motion and the turbulence motion are the causes of target return decorrelation. Along the same line, we note that for RD imaging the turbulence motion alone determines the extent to which the transmitted and the target return (scattered) beams are correlated. This, too, is different from the SAR case, where both the radar and the turbulence motions figure in determining whether we are operating in the short-range regime or the long-regime, etc. We will assume $|\bar{u}|$ is small enough so that the short-range case is in effect for our RD analysis.

In the short-range, small aperture limit, we have the following expression for the beam patterns of the forward propagated transmitter field and the backpropagated LO field at the target plane:

$$\underline{U}_L(\bar{p},t) = \underline{U}_B^*(\bar{p},t)$$
$$= (1/j\lambda L)\ \exp[-\alpha L/2]\ \exp[jkL + jk|\bar{p}|^2/2L]$$
$$\cdot\sqrt{2\pi a_x a_y}\ \exp[-(ka_x/2L)^2 x^2 - (ka_y/2L)^2 y^2]$$
$$\cdot\exp[\underline{\psi}(\bar{p} - \bar{u}t, -\bar{u}t)],\qquad (4.2.45)$$

where we have employed the usual elliptical-Gaussian beam profile. For an unresolved target, we then have the following expression for the $\underline{1}_y(t)$ (cf. (3.3.6)):

$$\underline{1}_y(t;\nu_D') = -\sqrt{P_T}(k^2 a_x a_y/2\pi L^2)\ \exp[-\alpha L]\int d\bar{s}_0\ \underline{T}(x_0,y_0,z_0)$$
$$\cdot\exp[2jk(L-z_0)]\ \exp[jk(x_0+y_0)^2/L]\ \underline{X}(\tau,\Delta\nu_D),$$

where
$$\qquad (4.2.46)$$

$$\underline{X}(\tau,\Delta\nu_D) \equiv \{\int_{-\infty}^{\infty} dt'\ \underline{s}_n^*(t'+\tau)\ \underline{s}_n(t')\ \exp[-j2\pi\Delta\nu_D\ t']$$
$$\cdot\exp[2\underline{\psi}(\bar{p}(t')-\bar{u}t', -\bar{u}t')]\ \}\qquad (4.2.47)$$
$$\cdot\exp[-j2\pi\nu_D' t]\ \exp[-j2\pi\Delta\nu_D\ 2(L-z_0)/c]$$

and τ, ν_D', and $\Delta\nu_D$ are as defined in Section 3.3.1 (cf. (3.3.8)). The time-dependence in $\bar{p}(t')$ of (4.2.47) embodies the rotational motion of the target.

Recall that we had earlier assumed a sufficiently short observation time so that the trajectory of a point scatterer on

the target can be linearized as follows: (cf. (3.3.4))

$$z(t) \simeq z_0 + (\Omega t)y_0,$$

$$y(t) \simeq y_0 - (\Omega t)z_0, \qquad\qquad (4.2.48)$$

$$x(t) = x_0,$$

where (x_0, y_0, z_0) are the coordinates of the scatterer at time $t = 0$. Using these linearized equations, $< | \underline{X}(\tau, \Delta\nu_D) |^2 >$ can be written as

$$< | \underline{X}(\tau, \Delta\nu_D) |^2 > = \int_{-\infty}^{\infty}\int_{-\infty}^{\infty} dt' dt'' \, \underline{s}_n^*(t'+\tau) \, \underline{s}_n(t') \, \underline{s}_n(t''+\tau) \, \underline{s}_n^*(t'')$$

$$\cdot \exp[-2D(\bar{p}(t') - \bar{p}(t'') - (t'-t'')\bar{u}, -(t'-t'')\bar{u})]$$

$$\cdot \exp[-j2\pi(t'-t'')\Delta\nu_D] \, \exp[4\sigma_\chi^2].$$

$$(4.2.49)$$

Let us explicitly write out the structure function with the help of Eq. (4.2.7).

$$D(-(\bar{u} + \hat{y}\Omega z_0) \, \Delta t, -\bar{u} \, \Delta t)$$

$$= 2.91 \, k^2 \int_0^L dz' \, C_n^2(z')[|(\bar{u} + \hat{y} \, \Omega z_0) \, \Delta t z' + (\bar{u} \, \Delta t)(L-z')|/L]^{5/3}$$

$$\simeq (2 \, \Delta \, t/t_0)^2, \qquad\qquad (4.2.50)$$

where

$$\Delta t = t' - t'',$$

$$t_0 \equiv 2 \, [2.91 \, k^2 \int_0^L dz' \, C_n^2(z')[|\bar{u}L + \hat{y}\Omega z_0 z'|/L]^{5/3}]^{-3/5}$$

$$(4.2.51)$$

The coherence time given by (4.2.51) bears a close resemblance to its counterpart (4.2.28) of the SAR case, which is (cf. Eq. (4.2.28))

$$t_o = 2 \left[2.91 \; k^2 \int_0^L dz' \; c_n^2(z')[\,|\bar{u}L - \hat{x}\,v(L-z')|/L]^{5/3} \right]^{-3/5}.$$

In fact, the $\hat{y}\Omega z_o z'$ term in (4.2.51), which accounts for the target rotation in the RD imaging configuration, plays the role of $-\hat{x}\,v(L-z')$ term in (4.2.28), which represents the radar's translational motion in the SAR configuration. Thus, we can give the same type of physical interpretation to the quantity t_o and its dependence on the directional relationship between the wind and the target rotation - $\bar{u}$ and $\hat{y}\,\Omega z_o$ - as we did in the SAR case.

However, there are some differences from the SAR case. One such difference is that the coherence time t_o depends on the target coordinate, as seen by the z_o-dependence in (4.2.51). The reason for this is obvious: different parts of the rotating target go through different amount of displacement in the transverse direction. This means that the extent of resolution loss due to atmospheric turbulence will depend on the target coordinate. The other major difference is that the target motion term $\hat{y}\,\Omega z_o$ term is given a different weighting factor (z') from the SAR case $(L-z')$. This is due to the earlier explained fact about the target being in motion for the RD radar and the radar being in motion for SAR. In fact, when $\bar{u} = \bar{0}$, vt_o, with t_o given by (4.2.28) is the usual transmitter-plane coherence length, whereas $\Omega t_o \overset{z_o}{\underset{\Lambda}{}}$, where t_o is given by (4.2.51), is the usual target-plane coherence length.

As with the SAR analysis earlier, the mathematics is now

almost identical to the frequency instability case, and we can obtain similar sorts of results. For the sake of brevity, however, their presentation will be omitted.

As far as RD radar's performance in the large aperture limit is concerned, we can state, without going into the specifics, that the major departure from the small aperture results would be in the CNR behavior. In both the small and large aperture limits, CNR loss due to spectrum broadening should be quite small in typical situations. However, in the large aperture limit, beam spreading will result in a significant reduction in the illumination intensity on the (spatially unresolved) target and thus lead to substantially lower CNR compared to the no-turbulence case.

We leave this section with the following observations. First, in all likelihood the spatial resolution of a RD imager is expected to suffer much smaller losses from the atmospheric turbulence than that of a SAR, the reason being optical RD radars can achieve excellent resolutions even with very short waveforms [as we shall see in Chapter V]. Second, as with SAR's, it makes a great deal of difference in practice how the imaging system is configured: because atmospheric turbulence is strongest near the ground, ground-based, airborne, and spaceborne RD radars will all be affected differently. [In the case of spaceborne RD radars, they will not be affected at all.] In Chapter V, we will calculate some numbers for an uplooking ground-based system.

4.3. Effects of Target/Radar Motion Errors

This section addresses two kinds of motion error problems
that take on a great deal of significance in the optical
frequency regime. Specifically, we will look at the possible
repercussions of: a) transmitter aim error; and b) target/radar
platform vibration. These departures from our ideal models,
which have not been analyzed before in the context of
high-resolution radars, will be examined in the CW SAR setting.
However, the general features of the analytical results ought to
be applicable to the 2D SAR's and RD radars as well.

4.3.1. Aim Error (CW SAR)

Because the angular width of a typical laser beam is so
narrow - typically on the order of tens of μrad to a mrad - a
very stringent requirement is placed on the imaging system's
alignment capability. When driven by spurious motions and
vibrations of the radar-carrying vehicle, this alignment
sensitivity can often lead to the laser beam's pointing at
erroneous target locations.

In this section, we shall explore the performance loss
incurred when transmitter aim errors are present in a CW SAR. To
do so, we will assume that actual transmitter plane is tilted
with respect to the nominal transmitter plane. In particular, we
will look closely at some limiting cases based on the extent of

the aim error and its correlation time. We start with the modelling of the transmitter aim error.

Let us suppose that the actual transmitter plane, defined by the plane normal to the direction of the transmitted beam's propagation, is tilted at some time-varying angle $\Theta(t)$ with respect to the nominal transmitter plane, and furthermore, that the motion of the transmitter plane is restricted to take place along a fixed transverse direction (see Fig. 4.9).

We will model the angular error $\Theta(t)$ as a stationary random process whose magnitude is much less than unity. Without loss of generality, we specify the following mean and covariance functions for $\Theta(t)$:

$$< \Theta(t) > \quad\quad = 0$$
$$< \Theta(t)\Theta(t') > \quad = \sigma_\Theta^2 \, K(t-t'), \quad\quad\quad\quad (4.3.1)$$

where

σ_Θ $\quad\quad$ = root-mean-square (rms) angular error

$K(t-t')$ $\quad$ = normalized covariance function.

Putting these pieces together, we can write the expression for the transmitter beam profile at the nominal transmitter plane $z = 0$ as follows:

$$\underline{U}_T(\bar{p}, t) = \sqrt{2/\pi a_x a_y} \, \exp[-(x/a_x)^2 - (y/a_y)^2 + jk\hat{\Phi}\cdot\bar{p} \, \sin\Theta(t)],$$

where $\quad\quad\quad\quad\quad\quad\quad\quad\quad\quad\quad\quad\quad\quad\quad\quad\quad (4.3.2)$

TRANSMITTER
BEAM
PROFILE

-y

ACTUAL
TRANSMITTER
PLANE

TILT
ANGLE

x

NOMINAL
TRANSMITTER PLANE

$\theta(t)$

z

LASER BEAM

TARGET

$\hat{\phi} = (\phi_x, \phi_y)$

-y

x

$\theta(t)$

TRANSMITTER PLANE

z

TILT IS CONFINED TO THE PLANE
DEFINED BY THE VECTOR $\pm\hat{\phi}$

Fig. 4.9 Tilt of the Transmitter Plane

LASER RADAR

$\hat{x}$ v

A: SPOT NOMINALLY ILLUMINATED
B: SPOT ACTUALLY ILLUMINATED

LASER BEAM

TARGET

A

$(vt, 0)$
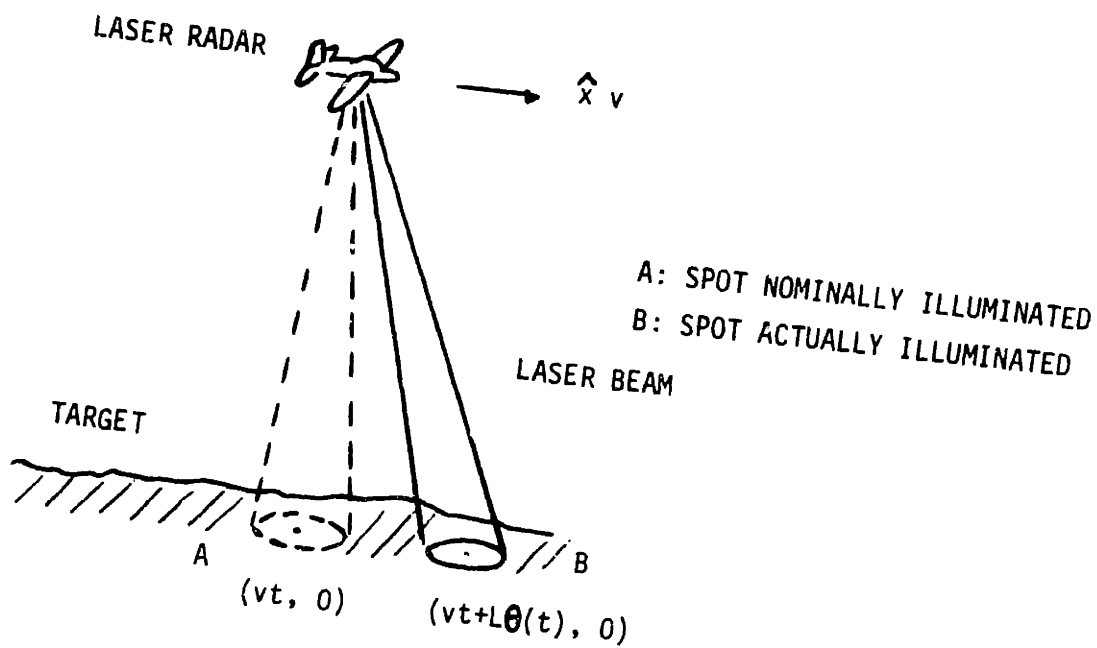
$(vt+L\theta(t), 0)$

B
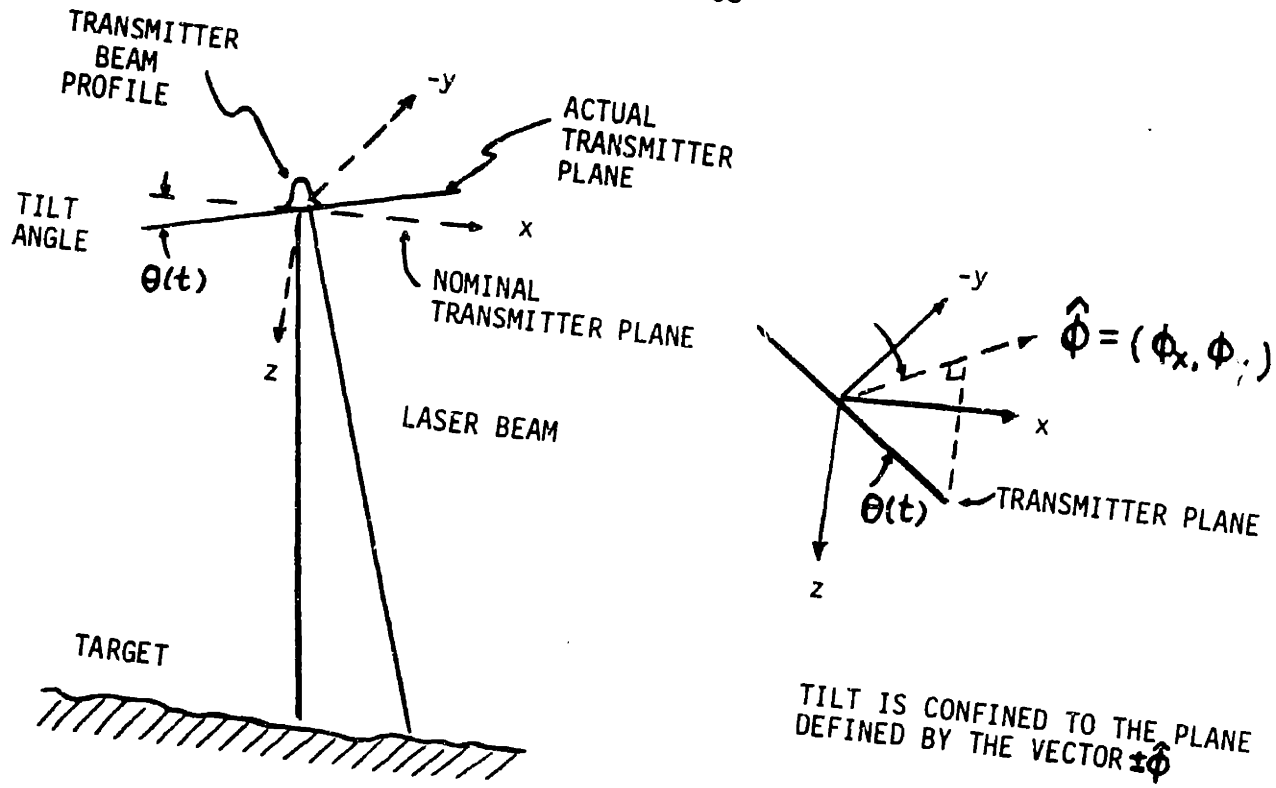
Fig. 4.10 Beam Wander due to Aim Error

$$\hat{\Phi} \quad = (\Phi_x, \Phi_y)$$

= unit vector giving the direction along which

   the transmitter plane's motion is confined,

$\Theta(t)$ = instantaneous angular error.

So, the field distribution at the nominal transmitter plane is equivalent to that produced by a localized plane wave impinging on the $z = 0$ plane at angle Θ, with its k-vector given by $\bar{k} = (k\Phi_x \sin\Theta, k\Phi_y \sin\Theta, k\cos\Theta)$.

A quick calculation yields the following expression for the transmitted beam at the target plane $z=L$ in the CW SAR configuration:

$$
\begin{aligned}
\underline{U}_L(\bar{p},t) \quad = & -j(k^2 a_x a_y/2\pi L^2)^{1/2} \exp[-\alpha L/2] \, \exp[jkL] \\
& \cdot \exp[j(k/2L)((x - vt)^2 + y^2)] \qquad\qquad (4.3.3) \\
& \cdot \exp[-(k/2L)^2 (a_x^2(x - vt - L\Phi_x \sin\Theta(t))^2 \\
& \qquad\qquad + a_y^2(y - L\Phi_y \sin\Theta(t))^2) \,].
\end{aligned}
$$

We see from (4.3.3) that the tilt of the transmitter plane displaces the laser beam on the target plane by $(L\Phi_x \sin\Theta(t), L\Phi_y \sin\Theta(t))$ from its nominal position $(vt, 0)$. Therefore, over the course of time, the laser beam on the target will move about its nominal position, following the time-varying, random tilt of the transmitter plane (see Fig. 4.10).

Note that the Doppler shift of the target return generated by the illumination (4.3.3) is unaffected by the aim error, as

evidenced by the absence of any $\Theta(t)$-dependence from the time-dependent phase term $\exp[j(k/2L)(x-vt)^2]$. This is because a tilt of the transmitter plane does not produce any change in the nominal range between the radar and the target. That the target return from a point scatterer acquires an amplitude modulation - via beam wander - as a result of an aim error but not phase-modulation is interesting in view of the importance of target return's phase history in SAR's operational scheme. We will come back to this point later.

For the target return component $\underline{l}_y(t) = \underline{y}(t) * \underline{h}(t)$, we have the following expression:

$$\underline{l}_y(t) = -\sqrt{P_T}(k^2 a_x a_y/2\pi L^2)\ \exp[-\alpha L]\ \exp[2jkL]$$
$$\cdot\int d\bar{p}\ \underline{T}(\bar{p})\ \exp[j(k/L)y^2]$$
$$\cdot\int^{z=L} d\tau\ \exp[-(2(ka_x/2L)^2 + j(k/L))(vt - v\tau)^2]$$
$$\cdot\exp[j(k/L)(x-v\tau)^2 - 2(ka_x/2L)^2(x-v\tau-L\Phi_x\sin\Theta(\tau))^2]$$
$$\cdot\exp[-2(ka_y/2L)^2(y-L\Phi_y\sin\Theta(\tau))^2]. \qquad (4.3.4)$$

The corresponding average intensity is obtained after some lengthy manipulations (see Appendix D for details).

$$< I_y(t) > = P_T(k^2 a_x a_y/2\pi L^2)^2 \lambda^2\ \exp[-2\alpha L]$$
$$\cdot\int d\bar{p}\ \underline{J}(\bar{p})\ \exp[-2(ka_x/2L)^2(x-vt)^2 - (ka_y/L)^2 y^2]$$
$$\cdot\int d\tau_d \exp[-2j(kv/L)(x-vt)\tau_d]\ \exp[-2(ka_x/2L)^2(v\tau_d)^2]$$
$$\cdot[1 + 4q\sigma_\Theta^2 + 4q^2\sigma_\Theta^4(1-K^2)]^{-1/2}[\pi/(v^2(\alpha_x - \beta c_x^2))]^{1/2}$$
$$\cdot\exp[\ \gamma(c_x v\tau_d/2)^2] \qquad (4.3.5)$$
$$\cdot\exp[(\alpha_x\beta/(\alpha_x-\beta c_x^2))\cdot(c_x(x-vt)/2 + c_y y)^2],$$

where

$$a_x \equiv 2(ka_x/L)^2$$

$$c_x \equiv (ka_x)^2 \Phi_x/L$$

$$c_y \equiv (ka_y)^2 \Phi_y/L$$

$$q \equiv ((ka_x\Phi_x)^2 + (ka_y\Phi_y)^2)/2 \qquad\qquad (4.3.6)$$

$$K \equiv K(\tau_d)$$

$$ß \equiv \sigma_\Theta^2(1 + K + 2q\sigma_\Theta^2(1 - K^2))/(1 + 4q\sigma_\Theta^2 + 4q^2\sigma_\Theta^4(1 - K^2))$$

$$\gamma \equiv \sigma_\Theta^2(1 - K + 2q\sigma_\Theta^2(1 - K^2))/(1 + 4q\sigma_\Theta^2 + 4q^2\sigma_\Theta^4(1 - K^2)).$$

In deriving the above, we have assumed $\Theta(t)$ to be a Gaussian random process, and have replaced $\sin\Theta(t)$ by $\Theta(t)$ since $\Theta(t) \ll 1$. In addition, we shall assume throughout the section that $q \gg 1$, since the angular beamwidth is much less than unity.

The τ_d-integral in (4.3.5) is difficult to evaluate in a general setting, and so, we will restrict our analysis to limiting cases. We start with the small perturbation case.

In the small perturbation case, it is assumed that $q\sigma_\Theta^2 \ll 1$. In physical terms, this means that the extent of (angular) beam wander is negligible compared to the (angular) beamwidth itself. Since $q\sigma_\Theta^2$ and $q^2\sigma_\Theta^4$ terms may then be ignored when they are accompanied by terms on the order of unity, we have the following simplification of (4.3.5):

$$< I_y(t) > \simeq P_T(k^2 a_x a_y/2\pi L^2)^2 \lambda^2 \exp[-2\alpha L]$$

$$\cdot \int d\bar{p} \; \mathcal{J}(\bar{p}) \; \exp[-2(ka_x/2L)^2(x-vt)^2 - (ka_y/L)^2 y^2]$$

$$\cdot \int d\tau_d \ [\pi/v^2 a_x]^{1/2} \ \exp[-2j(kv/L)(x-vt)\tau_d]$$

$$\cdot \ \exp[-2(ka_x/2L)^2 (v\tau_d)^2]$$

$$\cdot \ \exp[(1-K)\sigma_\Theta^2 (c_x v\tau_d/2)^2] \qquad\qquad (4.3.7)$$

$$\cdot \ \exp[(1+K)\sigma_\Theta^2 (c_x(x-vt)/2 + c_y y)^2].$$

In deriving the above, we have used the approximations $\beta \simeq \sigma_\Theta^2(1 + K)$ and $\gamma \simeq \sigma_\Theta^2(1-K)$.

The last two exponentials in (4.3.7) involving σ_Θ and K conveniently represent the effects of transmitter aim error. When they are compared with $\exp[-2(ka_x/2L)^2(v\tau_d)^2]$ and $\exp[-2(ka_x/2L)^2(x-vt)^2 - (ka_y/L)^2 y^2]$ terms , however, their exponents are seen to be only a small fraction - factor of $q\sigma_\Theta^2$ ($<< 1$) or so - of their counterparts.

Thus, in the small perturbation limit, there is no appreciable change in either the resolution or the CNR from the ideal no-aim-error case. This is true regardless of the correlation time t_Θ since we have not placed any constraint on t_Θ in our analysis.

The result we have just obtained makes good intuitive sense, since the basic nature of the target return should not change significantly because of an aim error of this magnitude. To elaborate, we note that whereas the strength of the target return (from a point scatterer) does vary with the aim error, this fluctuation is quite small in the small perturbation limit because the extent of beam's excursion is small.

We now investigate the large perturbation case, where $q\sigma_\Theta^2 \gg 1$, so that a typical (angular) aim error greatly exceeds the beamwidth itself. It follows then we can make the following approximations involving β, γ, $a_x - \beta c_x^2$, and $a_x\beta/(a_x - \beta c_x^2)$:

$$\beta(\tau_d) \simeq (1/2q)(1 - \epsilon(\tau_d))$$

$$\simeq 1/2q, \qquad\qquad (4.3.8)$$

where

$$\epsilon(\tau_d) \; \text{--> } \begin{cases} 1/(4q\sigma_\Theta^2) & \text{for } \tau_d \text{ --> } 0 \\ 1/(2q\sigma_\Theta^2) & \text{for } \tau_d \text{ --> } \infty, \end{cases}$$

$$\gamma(\tau_d) \; \text{--> } \begin{cases} 0 & \text{for } \tau_d \text{ --> } 0 \\ 1/2q & \text{for } \tau_d \text{ --> } \infty, \end{cases} \qquad (4.3.9)$$

$$a_x - \beta c_x^2 \simeq a_x(1 - (ka_x\Phi_x)^2 \cdot (1-\epsilon)/4q))$$

$$\text{[using (4.3.8)]} \qquad\qquad (4.3.10)$$

$$\simeq a_x[1 - (ka_x\Phi_x)^2/4q],$$

$$a_x\beta/(a_x - \beta c_x^2) \simeq 2(1 - \epsilon'(\tau_d)/(2(ka_y\Phi_y)^2 + (ka_x\Phi_x)^2)),$$

where $\qquad\qquad (4.3.11)$

$$\epsilon'(\tau_d) \equiv 4q\epsilon/(2(ka_y\Phi_y)^2 + (ka_x\Phi_x)^2).$$

In making the approximations above, we have used the relations $K(0) = 1$ and $K(\infty) = 0$. Incidentally, it can be shown - though not done here - that the transition of β from $\tau_d = 0$ to $\tau_d = \infty$ is smooth and monotonic, independent of what form K takes. The same

holds true for $\gamma(\tau_d)$, provided that K is positive-semidefinite. Applying these approximations to (4.3.5) yields

$$
\begin{aligned}
< I_y(t) > \simeq \ &P_T(k^2 a_x a_y/2\pi L^2)^2 \lambda^2 \ \exp[-2\alpha L] \\
&\cdot \int d\bar{p} \ \mathcal{J}(\bar{p}) \ [\pi/v^2 a_x]^{1/2}[1 - (ka_x\Phi_x)^2/4q]^{-1/2} \\
&\cdot \exp[-(\Phi_y(x-vt)-\Phi_x y)^2(k^2 a_x a_y/L)^2 \\
&\quad /(2(ka_y\Phi_y)^2+(ka_x\Phi_x)^2)] \\
&\cdot \int d\tau_d \ \exp[-(c_x(x-vt)+2c_y y)^2 \\
&\quad \cdot 2q\epsilon(\tau_d)/(2(ka_y\Phi_y)^2+(ka_x\Phi_x)^2)^2] \\
&\cdot \exp[-2j(kv/L)(x-vt)\tau_d] \\
&\cdot \exp[-2(ka_x/2L)^2(v\tau_d)^2(1 - (ka_x\Phi_x)^2 \ \gamma(\tau_d)/2)] \\
&\cdot [1 + 4q\sigma_\theta^2 + 4q^2\sigma_\theta^4(1-K^2)]^{-1/2}.
\end{aligned} \tag{4.3.12}
$$

There are a couple of things worth mentioning in regards (4.3.12). First, the two quadratic exponentials involving x-vt and y effectively give the on-target beam pattern in the presence of aim error. This becomes more obvious when we look at special cases. For example, suppose that the aim-error-induced beam movement occurs only along the x-direction. In our notation, this amounts to having $\Phi_x = 1$, $\Phi_y = 0$, $c_x = (ka_x)^2/L$, $c_y = 0$, and $q = (ka_x)^2/2$. The two quadratic exponentials in (4.3.12) are then reduced to

$$
\exp[-(ka_y/L)^2 y^2] \ \exp[- \eta(\tau_d)(1/L\sigma_\theta)^2(x-vt)^2]. \tag{4.3.13}
$$

where

$$
\eta(\tau_d) \longrightarrow \begin{cases} 1/2 & \text{for } \tau_d \longrightarrow 0 \\ 1 & \text{for } \tau_d \longrightarrow \infty \end{cases}
$$

Hence, we wind up with effective beamwidths of $\sim L\sigma_\Theta$ and
$\sim \lambda L/a_y$ in the x- and y-directions, respectively. When compared
with the beamwidths of the ideal case - $\sim \lambda L/a_x$ and $\sim \lambda L/a_y$,
respectively - we see that the effective beamwidth in the
y-direction is same as in the ideal case, whereas the effective
beamwidth in the x-direction greatly exceeds its counterpart in
the ideal case [since $q\sigma_\Theta \gg 1$]. Note that the effective
beamwidth in the x-direction is simply the extent of beam
excursion due to the transmitter aim error. Then, it should also
make sense that the effective beamwidth along the y-direction has
not changed from the ideal case, since there is no beam motion in
that direction. Same sort of situation prevails when the aim
error occurs only in the y-direction. In that case, we have

$$\exp[- \eta(\tau_d)(1/L\sigma_\Theta)^2 y^2] \exp[-2(ka_x/2L)^2(x-vt)^2] \qquad (4.3.14)$$

for the two quadratic exponential terms, and we can give the same
kind of interpretations as we did with the $\Phi_x = 1$, $\Phi_y = 0$ case.

The other point worth mentioning in regards to (4.3.12) is
that some of the factors in (4.3.12) may be either rid of their
τ_d-dependences or completely dropped without drastically
affecting the nature of the final result. For one, we may purge
the τ_d-dependence from the exponential term

$$\exp[-(c_x(x-vt)+2c_y y)^2 2q\varepsilon(\tau_d)/(2(ka_y\Phi_y)^2+(ka_x\Phi_x)^2)^2]$$

by replacing $\varepsilon(\tau_d)$ with its asymptotic $(\tau_d \longrightarrow \infty)$ value $1/(2q\sigma_\Theta^2)$.
This simplification can be justified to some extent by the fact
that the asymptotic value of $\varepsilon(\tau_d)$ is of the same order as its
initial-value $(\tau_d \longrightarrow 0)$ - twice to be exact - as shown in
(4.3.8). By applying a similar type of reasoning, we may drop
the γ term from $1 - (ka_x\Phi_x)^2 \gamma/2$ since $(ka_x\Phi_x)^2 \gamma/2$ is bounded
between 0 and 1/2. From a more practical standpoint, these
approximations make calculations easier. Obviously these
approximations will affect the CNR and resolution results
somewhat, but at this point, we are mainly looking for rough
estimates and a good understanding of the mechanism which governs
their behavior. Hence, we will use these approximations in the
subsequent analysis.

Unfortunately, we cannot make drop the τ_d-dependence from
$[1 + 4q\sigma_\Theta^2 + 4q^2\sigma_\Theta^4(1-K^2)]^{-1/2}$ as easily because of the order of
magnitude difference between its asymptotic value $1/(2q\sigma_\Theta^2)$ and
its initial-value $1/(4q\sigma_\Theta^2)^{1/2}$. So, to facilitate the
calculation, we adopt the following simple model for the
normalized covariance function:

$$K(\tau) = \begin{cases} 1 & \text{for } |\tau| \leq t_\Theta \\ 0 & \text{for } |\tau| > t_\Theta. \end{cases} \qquad (4.3.15)$$

where t_Θ may be viewed as the correlation time of $\Theta(t)$.
[Strictly speaking, this is not allowable as a covariance
function since its spectrum takes on negative values.

However, since we are carrying out only an approximate analysis, we will overlook this point].

We will now explore two limiting cases within the large perturbation regime: i) quasi-static case in which $t_\Theta \gg T$ prevails; and ii) dynamic case, in which $t_\Theta \ll T$ prevails, where T ($= 4L/ka_x v$) is the CW SAR's coherent processing time.

We shall investigate the quasi-static case first. With the covariance model of (4.3.15), the breakpoint of $[1 + 4q\sigma_\Theta^2 + 4q^2\sigma_\Theta^4(1-K^2)]^{-1/2}$ is determined by the correlation time t_Θ. Since $t_\Theta \gg T$ in the quasi-static limit and T gives the approximate width of the exponential term $\exp[-2(ka_x/2L)^2(v\tau_d)^2]$, we may therefore replace $[1 + 4q\sigma_\Theta^2 + 4q^2\sigma_\Theta^4(1-K^2)]^{-1/2}$ with $(4q\sigma_\Theta^2)^{-1/2}$ inside the τ_d integral. The τ_d-integral in (4.3.12) can then be approximated by

$$
\int_{-\infty}^{\infty} d\tau_d \ (4q\sigma_\Theta^2)^{-1/2} \exp[-2j(kv/L)(x-vt)\tau_d] \ \exp[-2(ka_x/2L)^2(v\tau_d)^2]
$$
$$
= (4q\sigma_\Theta^2)^{-1/2}\sqrt{2\pi} \ (L/ka_x v) \ \exp[-2(x-vt)^2/a_x^2] \qquad (4.3.16a)
$$

[the exponential term involving $\epsilon(\tau_d)$ has been taken outside the τ_d-integral since we have dropped the τ_d-dependence from it]. Combining this with the remaining terms of (4.3.12) involving $x-vt$ and y yields

$$
\left\{
\begin{array}{l}
(4q\sigma_\Theta^2)^{-1/2}\exp[-2(x-vt)^2/a_x^2] \; \exp[-(x-vt)^2/(L\sigma_\Theta)^2] \\[2mm]
\qquad \exp[-(ka_y/L)^2y^2], \qquad\qquad \text{for } \Phi_x = 1,\; \Phi_y = 0 \\[2mm]
\hfill (4.3.16b) \\[4mm]
(4q\sigma_\Theta^2)^{-1/2}\exp[-2(x-vt)^2/a_x^2] \; \exp[-2(ka_x/2L)^2(x-vt)^2] \\[2mm]
\qquad \exp[-y^2/(L\sigma_\Theta)^2], \qquad\qquad \text{for } \Phi_x = 0,\; \Phi_y = 1
\end{array}
\right.
$$

[omitting inessential terms]

Resolution and CNR behavior of a CW SAR in the presence of aim errors can be examined with the help of (4.3.16b). As borne out by the $\exp[-2(x-vt)^2/a_x^2]$ term, the along-track resolution is seen to be preserved from the ideal case regardless of the transmitter plane's tilt orientation; it is still $\sim a_x$ [Of course, the approximations we have made along the way would have degraded the actual resolution somewhat]. The cross-track resolution, on the other hand, does depend on the tilt orientation. With beam wander in the x-direction only, y_{res} is $\sim \lambda L/a_y$ and thus unchanged from the ideal case, whereas it is much worse - $\sim L\sigma_\Theta$ - with beam wander in the y-direction only.

CNR loss can be estimated by taking into account the constant factor $(4q\sigma_\Theta^2)^{-1/2}$ ($\ll 1$) in front of (4.3.16b) - for the ideal case, this factor would be replaced by 1 - and the resolution loss. In the first case of (4.3.16b), the CNR loss is quite large because of the constant factor, even though the resolution loss is negligible. In the second case, because the resolution loss in the y-direction leads to a larger target area contributing to $< I_y(t) >$, the CNR loss is minimal.

Although we have examined only two special cases here, it is clear that for an intermediate case - mixed tilt orientation (Φ_x, $\Phi_y \neq 0$) - we would have a partial loss of CNR and a partial loss of cross-track resolution. Valuable physical insight in interpreting these long-term (ensemble average) behaviors can be gained by studying the short-term behavior. We will now do so.

The key to understanding the effects of aim errors on CW SAR is to realize that the SAR's sharp along-track resolution is derived from utilizing the target return's Doppler history. In the quasi-static limit of the large perturbation regime, the laser beam could be illuminating a part of the target very far from the spot which is supposed to be illuminated. However, as pointed out previously, the Doppler history of the target return for each point scatterer is unaffected by this. Furthermore, since the laser beam wanders very slowly when measured on the scale of the coherent integration time T (in the quasi-static limit), the temporal coherence of the target return is well maintained. Together, these ensure that the SAR images the part of the target with the correct along-track coordinate, namely vt, and does so with the same resolution as in the ideal case ($\sim a_x$).

Since CW SAR does not provide such focussing action in the cross-track direction, the cross-track coordinates of the target area imaged by the SAR are simply those of the target region actually illuminated by the laser beam, and the target image's instantaneous cross-track resolution is given by the actual

beamwidth $\sim \lambda L/a_y$. It follows then that one of the main short-term effects of aim errors is geometric distortion of the target image; target region in the vicinity of $(vt, y_I(t))$ is imaged at time t instead of the nominal area centered at $(vt, 0)$, where $y_I(t)$ is the y-coordinate of the target region illuminated by the laser beam at the time.

The other major short-term effect of aim errors is CNR loss. Even though SAR selects the correct along-track coordinate on the target, the actual illumination intensity on that spot could be quite weak because of the beam wander (see Fig. 4.10), and thus, a large CNR loss is possible. In fact, the short-term CNR loss would be proportional to $\exp[-(ka_x/2L)^2 \delta x^2(t)]$, where $\delta x(t)$ is the difference in the along-track coordinate between the nominal spot and the spot actually illuminated at time t. As a result, we would have a time-varying CNR over the course of time, as the laser beam wanders about.

The long-term behaviors we discussed earlier are just a natural extension of these short-term behaviors. Since the short-term along-track resolution is unaffected by aim error, neither is the long-term along-track resolution. The long-term cross-track resolution, on the other hand, reflects the extent of beam wandering in the y-direction over the course of time. Similarly, the long-term CNR behavior reflects the effect of averaging over the short-term behavior.

Our findings suggest that even though it may be difficult to suppress the type of aim error modelled in this section, we may

still be able to compensate for its effects in certain cases of the quasi-static limit. For example, if the aim error occurs along the x-direction and we have a means of measuring the error, we can estimate the actual beam intensity falling on the nominal target location. This estimate may then be used to assign an appropriate weighting factor to the raw target pixel intensity so that we have a correct representation of the nominal spot's true reflectivity.

We now explore the other extreme limit of the large perturbation case, the dynamic limit. Since the correlation time t_Θ is assumed to be much shorter than the coherent processing time T in this limit, the τ_d-integral of Eq. (4.3.12) may be written as a sum of several integrals as follows:

$$\int_{-\infty}^{\infty} d\tau_d \ \exp[-2j(kv/L)(x-vt)\tau_d] \ \exp[-2(ka_x/2L)^2(v\tau_d)^2]$$
$$\cdot [1 + 4q\sigma_\Theta^2 + 4q^2\sigma_\Theta^4(1-\kappa^2)]^{-1/2}$$
$$\simeq \ \{ \int_{-t_\Theta}^{t_\Theta} d\tau_d \ (4q\sigma_\Theta^2)^{-1/2} + (\int_{-\infty}^{\infty} - \int_{-t_\Theta}^{t_\Theta})d\tau_d \ (4q^2\sigma_\Theta^4)^{-1/2} \ \}$$
$$\cdot [\text{exponential terms}] \qquad (4.3.17)$$
$$\equiv \ I_1 + I_2$$

where

$$I_1 \equiv ((4q\sigma_\Theta^2)^{-1/2} - (4q^2\sigma_\Theta^4)^{-1/2}) \int_{-t_\Theta}^{t_\Theta} d\tau_d \ [\text{exponential terms}]$$
$$I_2 \equiv (4q^2\sigma_\Theta^4)^{-1/2} \int_{-\infty}^{\infty} d\tau_d \ [\text{exponential terms}]$$

The integral I_1 may be evaluated approximately by noting that $4q\sigma_\Theta^2 << 4q^2\sigma_\Theta^4$ and that in the dynamic limit the Gaussian

integrand varies very slowly on the scale of t_Θ. The result is

$$I_1 \simeq (q\sigma_\Theta^2)^{-1/2}[\sin((2kv/L)(x-vt)t_\Theta)] \, / \, [(2kv/L)(x-vt)] \tag{4.3.18}$$

This function has the first nulls at $x-vt = \pm \, \lambda L/4vt_\Theta$ and the peak value of $t_\Theta(q\sigma_\Theta^2)^{-1/2}$. If we define the width of I_1 to be the separation distance between the first nulls, then it is $\pi L/2kvt_\Theta$ or equivalently $(\pi/8)(T/t_\Theta)a_x$. Incidentally, the $(\sin z)/z$ type of dependence above is a direct consequence of using a rectangular form of covariance function. If some other form had been used, we would have had a different type of function for '4.3.18).

The integral I_2 turns out to be

$$I_2 \simeq (L/ka_xv)(\sqrt{\pi/2} \, / \, q\sigma_\Theta^2) \, \exp[-2(x-vt)^2/a_\lambda^2]. \tag{4.3.19}$$

which has the width equivalent to the along-track resolution of the ideal case, viz. $\sqrt{2} \, a_x$. Note that by definition of the dynamic limit we are operating in, the width of I_2 is much narrower than that of I_1.

It is easy to see in I_1 the effect of the transmitter aim error on the SAR's pulse compression operation. Although the loss of target return temporal coherence here is caused by an amplitude fluctuation arising from the laser beam's rapid wandering - unlike in the atmospheric turbulence and frequency instability case where a phase fluctuation is responsible - , it

nevertheless, reduces the effectiveness of the pulse compression operation. This is verified by the fact that the width of I_1 is inversely proportional to t_Θ.

To decide what the along-track resolution is in this case, we need to compare the contributions (to $< I_y(t) >$) of I_1 and I_2, after having taken into account the x-dependent part of the effective beam pattern given by $\exp[-(\Phi_y(x-vt)-\Phi_x y)^2 (k^2 a_x a_y/L)^2 /(2(ka_y\Phi_y)^2+(ka_x\Phi_x)^2))] \cdot \exp[-(c_x(x-vt)+2c_y y)^2 /(\sigma_\Theta^2(2(ka_y\Phi_y)^2 + (ka_x\Phi_x)^2)^2))]$ of Eq. (4.3.12) against one another. It is clear that the cross-track resolution is still determined by the effective beamwidth in the y-direction alone.

The width of I_2, $\sqrt{2}\, a_x$, is always much narrower than the effective beamwidth in the x-direction, which could be anywhere between $\sim L/ka_x$ and $\sim L\sigma_\Theta$ depending on the tilt orientation. We cannot make such general statement about the width of I_1 $(\pi/8)(T/t_\Theta)a_x$. If we limit our discussion to situations wherein $L/ka_x \gg (T/t_\Theta)a_x$ prevails - which is equivalent to the condition $t_\Theta \gg a_x/v$ - then, we may essentially ignore the beam pattern term. Roughly estimating the contributions of I_1 and I_2 to $< I_y(t) >$, we have $\sim Ta_x/(q\sigma_\Theta^2)^{1/2}$ for I_1 and $\sim Ta_x/q\sigma_\Theta^2$ for I_2. This means that the along-track resolution in this case is basically given by the width of I_1, which, as pointed out before, is much worse than the resolution for the ideal case.

At this point, we should observe that it may be possible to recover the along-track resolution of the ideal case in the situation described above. This may be accomplished by (high-

pass) filtering the output of the SAR's IF filter to remove the low-frequency component I_1 before it is square-law detected.

We now attempt to provide some insight into the resolution behavior of the dynamic limit. Suppose we were to sketch a typical target return from a point scatterer as a function of time. It might resemble Fig. 4.11, where t_1, t_2, and t_3 denote the following quantities:

t_1 = time during which the scatterer is illuminated as the rapid tilt of the transmitter plane causes the laser beam to sweep across the scatterer.

t_2 = interarrival time between successive illuminations of the scatterer.

t_3 = time during which the laser beam is able to illuminate the scatterer: beyond this time, the scatterer cannot be reached by the beam.

Fig. 4.11 is drawn based on a premise that in the dynamic limit of the large perturbation regime, the laser beam typically wanders far enough ($\sigma_\Theta \gg \lambda /a_{x,y}$) and quickly enough ($t_\Theta \ll T$) so that it can illuminate a given spot on the target on several different occasions during the coherent processing time. In this limit, we have
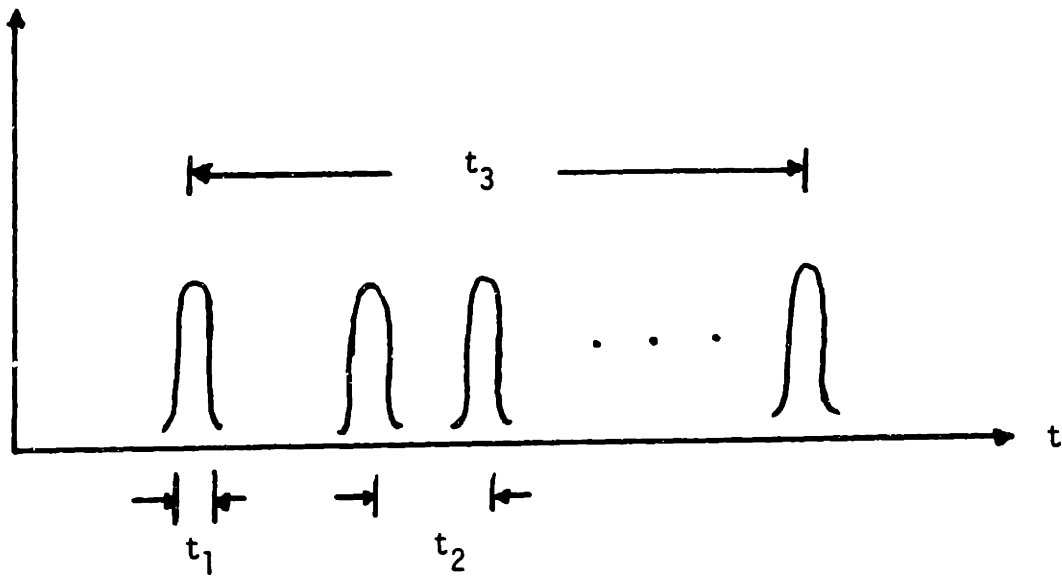
Fig. 4.11 A Typical Return from a Point Scatterer
in the Dynamic Limit of Large Perturbation Case

$$vt_\Theta \ll vT \sim \lambda L/a_x \ll L\sigma_\Theta. \tag{4.3.20}$$

In other words, the rms velocity associated with the beam wander - approximately $L(\sigma_\Theta/t_\Theta)$ - is much greater than the nominal translation velocity of the radar v. Taking a rough estimate of the averages $\langle t_1 \rangle$, $\langle t_2 \rangle$, and $\langle t_3 \rangle$, we have

$$\langle t_1 \rangle \sim \left(\begin{array}{c} \text{angular beamwidth} \\ \text{of the laser beam} \end{array} \right) \Big/ \left(\begin{array}{c} \text{rms angular velocity of} \\ \text{the beam due to the tilt} \end{array} \right)$$

$$\sim (\lambda /a_{x,y})/(\sigma_\Theta/t_\Theta) \ll t_\Theta,$$

$$\langle t_2 \rangle \sim t_\Theta, \tag{4.3.21}$$

$$\langle t_3 \rangle \sim \begin{cases} L\sigma_\Theta/v & (\gg T) \qquad \text{for } \Phi_x = 1, \ \Phi_y = 0 \\ T & \qquad \text{for } \Phi_x = 0, \ \Phi_y = 1. \end{cases}$$

The important question is then when does the beam wander due to the tilt of the transmitter plane begin to seriously affect the pulse compression operation of CW SAR's? In this regard, we may view the skinny pulses of Fig. 4.11 which are separated by $\langle t_2 \rangle$ seconds on the average, as time samples of the continuous target return from the scatterer [granted that they are not periodic samples]. As we learned from the 2D SAR analysis in Section 3.2.2, for a SAR to operate properly, the sampling rate must be greater than the speckle decorrelation rate v/a_x. Thus, we need to have at least $t_\Theta \lesssim a_x/v$. However, in deriving the

results for the dynamic limit earlier, we had assumed that $t_\Theta \gg a_x/v$, and consequently, the along-track resolution has turned out to be much worse than that of the ideal case.

To discuss the CNR behavior, we only need to compare I_1 with its counterpart for the ideal case, which is $\sim T$ $\cdot \exp[-2(x-vt)^2/a_x^2]$ — since there is no change in the y-direction from the quasi-static case. As mentioned before, the contribution of I_1 to $< I_y(t) >$ in the limit $t_\Theta \gg a_x/v$ is $\sim Ta_x/(q\sigma_\Theta^2)^{1/2}$, while for the ideal case, the exponential contributes $\sim Ta_x$. Thus, the CNR behavior in this regime is similar to that of the quasi-static limit of the large perturbation regime which we earlier encountered (cf. (4.3.16b)). This is somewhat surprising: we might expect a further CNR loss in the dynamic limit because of the shorter correlation time t_Θ. The reason for this similarity is that although the along-track resolution does suffer from a shorter t_Θ, I_1's (peak) amplitude also decreases by the same factor, thus offsetting the resolution loss.

This concludes the performance analysis of the CW SAR's that suffer from random aim errors.

4.3.2. Vibration (CW SAR)

In coherent laser radar imaging, many physical processes which could be ignored in microwave imaging become significant because of the shortness of laser wavelengths. Target/radar platform vibration is one such area. The extent of target/radar platform vibration likely to be encountered in normal imaging environments may be modest when measured on the scale of tens of centimeters or so, but it could be quite large on the scale of tens of microns. Since vibration of such magnitude can dramatically change the target return's Doppler shift history, high-resolution radars could suffer a considerable performance loss as a result.

From a mathematical point, we may consider the problem of analyzing the effects of radar platform vibration as being equivalent to that of target vibration analysis. Therefore, in this section, we shall assume that only target vibration exists and analyze its effects in the context of CW SAR. We start with a very simple model of the target vibration.

We will assume the target vibration to be of longitudinal nature and varying sinusoidally in time. [A short, qualitative discussion of the random vibration case is given after the periodic vibration analysis]. In equation form,

$$d(\bar{p}, t) = a_n(\bar{p}) \sin(\omega_n t + \Phi_n(\bar{p})), \qquad (4.3.22)$$

where

$d(\bar{p}, t)$ = displacement of the target from its

equilibrium position at time t,

$\left\{ \begin{array}{c} a_n(\bar{p}) \\ \Phi_n(\bar{p}) \end{array} \right\}$ = amplitude and the phase of the vibration mode

ω_n = frequency of the vibration

[(4.3.22) could represent a particular mode of the vibration, say the n-th mode, in which case we can obtain the total response by summing over all the modes at the end.] The $\bar{p}$-dependence in a_n and Φ_n allows us to accomodate the transverse mode pattern.

To the lowest order, the optical phase corresponding to the change in the roundtrip path length between the radar and the target due to $d(\bar{p}, t)$ is,

$$\Theta(\bar{p}, t) \equiv 2kd(\bar{p}, t), \qquad (4.3.23)$$

where we have assumed that the displacement of the target surface during the roundtrip delay 2L/c is negligible compared to the wavelength λ . Incorporating this effect into our laser radar model we obtain

$$\begin{aligned}
\underline{y}(t) = &-\sqrt{P_T} \, (k^2 a_x a_y / 2\pi L^2) \, \exp[-\alpha L] \, \exp[2jkL] \\
&\cdot \int d\bar{p} \, \underline{T}(\bar{p}) \, \exp[j(k/L)((x-vt)^2 + y^2)] \qquad (4.3.24) \\
&\cdot \exp[-2(ka_x/2L)^2(x-vt)^2 - 2(ka_y/2L)^2 y^2] \\
&\cdot \exp[2jka_n(\bar{p})\sin(\omega_n t + \Phi_n(\bar{p}))].
\end{aligned}$$

Putting this through the SAR's processor, we come up with the following mean intensity $< I_y(t) > (= < | \underline{y}(t) * \underline{h}(t) |^2 >)$ expression:

$$< I_y(t) > = P_T(k^2 a_x a_y/2\pi L^2)^2 \exp[-2\alpha L] \lambda^2$$
$$\cdot \int d\bar{p} \; \mathcal{J}(\bar{p}) \exp[(ka_y/L)^2 y^2] \; g_x(\bar{p},t), \qquad (4.3.25)$$

where

$$g_x(\bar{p},t) \equiv \exp[-2(ka_x/2L)^2(x-vt)^2]$$
$$\cdot | \int d\tau \exp[2j(k/L)((x+vt)/2 -v\tau)(x-vt)]$$
$$\cdot \exp[-(ka_x/L)^2((x+vt)/2 -v\tau)^2] \exp[2jkd(\bar{p},\tau)]|^2$$

$$(4.3.26)$$

Note that the cross-track resolution is still determined by the beamwidth in the y-direction $(2L/ka_y)$ whereas the along-track resolution is determined by the width of the function $g_x(\bar{p},t)$.

Using a Fourier series representation of $\exp[2jkd(\bar{p},\tau)]$

$$\exp[-ja\sin\Theta] = \sum_{m=-\infty}^{\infty} (-1)^m J_m(a) \exp[jm\Theta], \qquad (4.3.27)$$

where J_m is the m-th order Bessel function, we can rewrite (4.3.26) as

$$\pi (L/ka_x v)^2 \exp[-2(k\bar{a}_x/2L)^2(x-vt)^2]$$
$$\cdot | \sum_m (-1)^m J_m(2ka_n(\bar{p})) \exp[-jm(\Phi_n(\bar{p}) + \omega_n(x+vt)/2v)]$$
$$\cdot \exp[-((x-vt) + m \omega_n /2(kv/L))^2/a_x^2]|^2 \qquad (4.3.28)$$

The first question we would like to ask is the following:

under what conditions does the target vibration not affect the CW SAR's performance significantly? To answer this question, it may be better to look at (4.3.26) rather than the Bessel function representation (4.3.28). In the context of (4.3.26), our question can be recast as follows: when can the $\exp[2jkd(\bar{p},\tau)]$ term be neglected?

There are two situations under which $\exp[2jkd(\bar{p},\tau)]$ can be ignored. The first case is when

$$2k|a_n(\bar{p})|_{max} \underset{\sim}{<} \pi/4 \qquad (4.3.29)$$
$$\text{-->} \quad |a_n(\bar{p})|_{max} \underset{\sim}{<} \lambda/16.$$

This corresponds to the maximum phase change due to the target displacement being negligible.

The second case is when the maximum phase change due to the vibration over the (temporal) width of the $\exp[-(ka_x/L)^2((x+vt)/2 - v\tau)^2]$ term is small. Taking the width as the coherent processing time T ($=4L/ka_x$), and assuming $2k|a_n(\bar{p})|_{max} \underset{\sim}{>} \pi/4$ (otherwise, we revert to the first case), we arrive at the condition

$$2k|a_n(\bar{p})|_{max} \Delta|\sin(\omega_n\tau + \Phi_n(\bar{p}))|_{max} \underset{\sim}{<} \pi/4, \qquad (4.3.30)$$

where $|a_n(\bar{p})|_{max} \Delta|\sin(\omega_n\tau + \Phi_n(\bar{p}))|_{max}$ is the maximum target displacement at $\bar{p}$ during T seconds. A sufficient condition for the above inequality is obtained by taking

$\Delta |\sin(\omega_n \tau + \Phi_n(\bar{p}))|_{max}$ to be $\sim \omega_n T$ (assuming $\omega_n T < \pi/4$). Under this condition, (4.3.30) reduces to

$$\omega_n \equiv 2\pi/T_n \lesssim (\pi/4)(1/2k|a_n(\bar{p})|_{max}) \ (1/T)$$
$$\longrightarrow T_n \gtrsim 16T \ k|a_n(\bar{p})|_{max}. \qquad (4.3.31)$$

Physically, the first condition corresponds to the target displacement not being noticeable on scale of the optical wavelength. In this case, only the m = 0 term in the expansion (4.3.28) is significant enough to be retained. The second condition corresponds to a quasistatic situation where the target is vibrating sufficiently slowly so that the Doppler shift associated with the vibration is not resolvable during the coherent processing time T. This is seen by rearranging (4.3.31) as follows

$$T \lesssim 1/|\omega_v|_{max} \sim 1/(2k|a_n(\bar{p})|_{max} \omega_n), \qquad (4.3.32)$$

where $|\omega_v|_{max}$ is the maximum Doppler shift associated with the target vibration ($|a_n(\bar{p})|_{max}\omega_n$ = maximum velocity).

Before we proceed, we should point out that because of the $\bar{p}$-dependence in the phase term $\Phi_n(\bar{p})$, the along-track resolution may vary with $\bar{p}$.

Another question we can ask is: can we retain at least the along-track resolution of the ideal case if not the CNR? The answer to this question can be found by examining the

Fourier-series representation of $g_x(\bar{p},t)$ given by (4.3.28). We note that the Gaussian exponentials representing different m-terms are separated by $\Delta(x-vt) \equiv \omega_n /(2kv/L)$. Therefore, if this separation is larger than the width of the envelope function $\exp[-2(ka_x/2L)^2(x-vt)^2]$, then only the m = 0 term will be included in the output. This condition just stated amounts to

$$\omega_n \gtrsim v/a_x. \tag{4.3.33}$$

When this condition is satisfied, we retain the along-track resolution of $\sqrt{2}\ a_x$.

The inequality expressed by (4.3.33) is nothing new to us. It is the same old Nyquist sampling rate in the time domain. Unlike in Section 3.2.2, however, there are no periodically transmitted pulses that sample the Doppler history of the target return. Instead, the periodic vibration of the target generates an infinite number of harmonics with fundamental frequency ω_n. As a result, the target return spectrum is that of a stationary target - stationary in a sense that it is not vibrating - duplicated at frequencies $\omega = m\omega_n$, m = 0, ± 1, $\pm 2,\dots$. (see Fig. 4.12) Clearly, the condition stated in (4.3.33) is necessary to avoid the overlapping of the different harmonic components, each of which has bandwidth of $\sim v/a_x$.

There is a mathematical difference as well as a physical difference between the periodic vibration addressed here and the periodic sampling of Section 3.2.2. The difference is that the
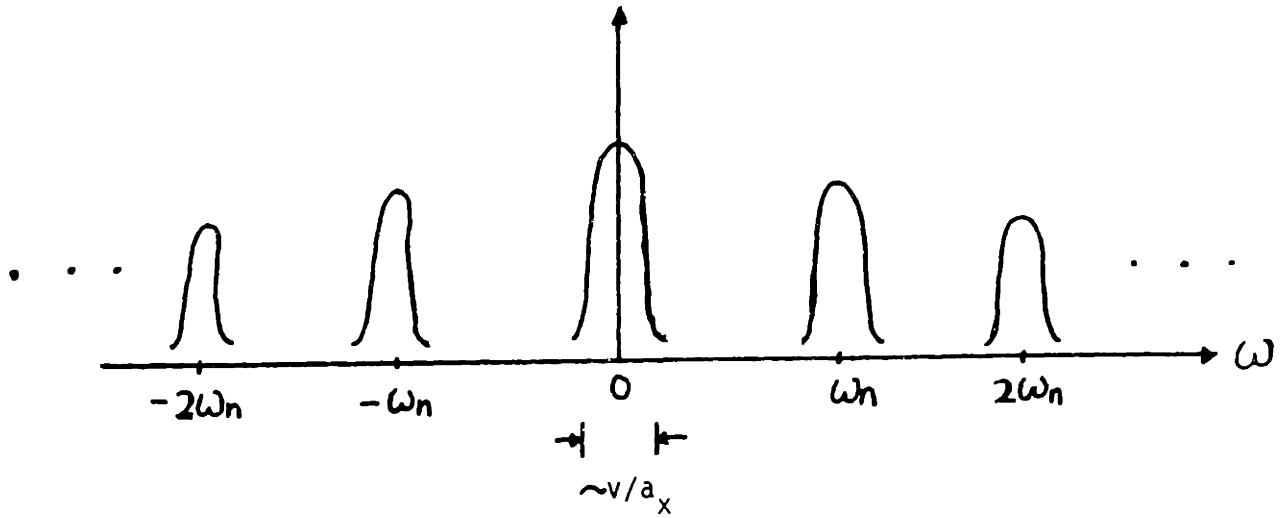
Fig. 4.12   Spectrum of the Target Return from a Point Scatterer:
Periodic Vibration Generates Harmonic Components

vibration-induced harmonics in general have different amplitude coefficients: the amplitude coefficients are Bessel functions $J_m(2ka_n(\bar{p}))$. [Periodic sampling, on the other hand, produces spectra of equal amplitude]

Assuming that the vibration frequency is high enough to satisfy (4.3.33), we have for $g_x(\bar{p},t)$

$$g_x(\bar{p},t) \simeq \pi \, (L/ka_x v)^2 \, |J_0(2ka_n(\bar{p}))|^2 \qquad (4.3.34)$$
$$\cdot \exp[-2(ka_x/2L)^2 (x-vt)^2] \, \exp[-2(x-vt)^2/a_x^2].$$

This result is identical to that of the ideal case (no vibration) except for the presence of the Bessel function. If the amplitude of vibration is large compared to the wavelength, i.e., $ka_n(\bar{p}) \gg 1$, then we may use the following asymptotic approximation:

$$J_m(x) \sim \sqrt{2/\pi|x|} \, \cos(x - \pi/4 - m\pi/4) \quad \text{as} \quad |x| \longrightarrow \infty \qquad (4.3.35)$$

Therein lies the problem with the target vibration when the amplitude of the vibration is large: even if we can maintain the ideal along-track resolution, the CNR loss will be dramatic. The reason for this loss is rather obvious. The energy in the target return is divided among all harmonics, and by retaining only the fundamental mode (m = 0) in an attempt to maintain the along-track resolution of the ideal case, we lose most of the energy present in the higher harmonics.

To calculate the CNR loss in the high-frequency, large

vibration limit, we should first compare the scale of variation for $a_n(\bar{p})$ to the along-track resolution $\sqrt{2}\, a_x$. If $a_n(\bar{p})$ changes fast enough so that $\Delta|ka_n(\bar{p})|_{max}$ within one resolution width $\sqrt{2}\, a_x$ exceeds the order of unity, then we have $g_x(\bar{p},t)$ that is oscillatory as a function of $\bar{p}$ (because of the $\cos(x - \pi/4 - m\pi/4)$ asymptotic behavior), and $|J_o(2ka_n(\bar{p}))|^2$ term averages out to be $1/(2\pi k\bar{a}_n(\bar{p}))$, where $\bar{a}_n(\bar{p})$ is the spatial average over the resolution width. On the other hand, if $a_n(\bar{p})$ changes sufficiently slowly on the scale of a_x, then we have a CNR-loss factor which is coordinate dependent. In summary, we have

$$CNR(a_n(\bar{p}) \neq 0)/CNR(a_n(\bar{p})=0)$$

$$\simeq \begin{cases} 1/(2\pi k\bar{a}_n(\bar{p})) & : \text{fast variation} \\ (1/\pi ka_n(\bar{p}))\cos(2ka_n(\bar{p}) - \pi/4) & : \text{slow variation} \end{cases}$$

where $\hspace{10cm}$ (4.3.36)

$$CNR(a_n(\bar{p}) \neq 0) = \text{CNR with target vibration}$$

$$CNR(a_n(\bar{p})=0) = \text{CNR without target vibration}$$

for the case where $ka_n(\bar{p}) \gg 1$ and $\omega_n \gtrsim v/a_x$.

Thus far, we have dealt only with periodic vibrations. Next, we briefly discuss CW SAR's performance loss due to random vibrations of target/radar platform which are characterized by rms amplitude σ_d (equivalent to optical phase fluctuation of $2k\sigma_d$ according to Eq. (4.3.23)) and correlation time t_d.

Based on the periodic vibration analysis, we know that there

exist circumstances under which the effect of random vibration would be minimal. One such situation arises when σ_d does not exceed the order of wavelength. Another scenario, perhaps more likely one, given the shortness of optical wavelengths, involves the quasi-static case, in which the vibration occurs sufficiently slowly so that the target/radar platform moves less than a fraction of a wavelength during the coherent integration time.

On a more general note, if we assume that $d(t)$, the displacement of the target/radar platform due to vibration, is a zero-mean, WSS Gaussian random process with a Gaussian covariance function ($K_{dd}(\tau) \equiv \langle d(t)d(t+\tau) \rangle = \sigma_d^2 \exp[-(\tau/t_d)^2]$), then, the correlation $R(\tau) \equiv \langle \exp[-2jkd(t)] \exp[2jkd(t+\tau)] \rangle$ is given by

$$R(\tau) = \exp[-(2k\sigma_d)^2(1 - \exp[-(\tau/t_d)^2])]. \qquad (4.3.37)$$

For a large vibration, i.e., for $k\sigma_d \gg 1$, $R(\tau)$ falls off very rapidly to values below e^{-1} even for $|\tau| \ll t_d$. In this regime, the correlation function may be approximated by

$$R(\tau) \simeq \exp[-8(\tau/t_v)^2], \qquad (4.3.38)$$

where

t_v = correlation time of the phase term
induced by random vibration
$= \sqrt{2}\, t_d/k\sigma_d$.

Note that $t_v \ll t_d$. At this point, we can write down the

along-track resolution loss by inspection, as there is a precise analogy between this problem and the frequency instability problem (see Eqs. (4.1.6) and (4.1.16) for example). The resolution loss factor ε is

$$\varepsilon \simeq [1 + (T/t_v)^2]^{1/2}, \tag{4.3.39}$$

where T is the coherent integration time. The CNR result also carries over from the frequency instability analysis, with t_v playing the role of t_θ.

We conclude this section with three remarks. First, the lower limit of SAR's along-track resolution is provided by the beamwidth in the x-direction, as with the frequency instability case and some atmospheric turbulence cases. Second, it is conceivable that we may be able to measure and remove the effect of target vibrations from the target return. In fact, we will see in Chapter V, where we calculate some numbers, that performance loss due to vibration can be quite serious - especially for an airborne SAR - and must be properly taken care of. Finally, from the SAR analysis just concluded, we can see - without going through the mathematics - that the vibration can have damaging effects on RD radar's performance as well, especially on the Doppler resolution. However, because RD radars tend to employ shorter coherent integration times than SAR's do, the effect will not be as severe.

CHAPTER V

SYSTEM CALCULATIONS

Thus far, we have considered the performance of high-resolution imagers only analytically. In this chapter, we develop a deeper appreciation for the results of the earlier chapters by calculating the performance measures in two specific imaging configurations: airborne SAR looking down at a ground target and a ground-based RD radar looking up at a rotating, airborne target. For the SAR, the operating range of interest is assumed to be on the order of a hundred km or less, whereas it is presumed to be as long as hundreds or even a thousand km for the RD radar. For these calculations, parameter values afforded by existing laser radar technologies are utilized whenever appropriate.

Chapter V is organized as follows. First, spatial resolution and CNR of optical SAR's and RD radars are computed and plotted for a variety of parameter values, assuming no laser frequency instability, atmospheric turbulence, or motion errors. The assumption of an ideal operating environment is then relaxed and the performance measures are reevaluated. Finally, the feasibility of these imagers are discussed based on the preceding results.

5.1. Ideal Case

In this section, we calculate the performance of optical SAR's and RD radars operating under ideal conditions for the two imaging scenarios mentioned earlier. These calculations are carried out at the wavelength of 10.6 μm, mainly because there already exist fairly efficient, stable, and powerful CO_2 lasers and wideband HgCdTe detectors at this wavelength [3,4,49-51], and also because the atmospheric attenuation characteristics are relatively benign in the 10 μm region compared to other wavelengths.

Fig. 5.1 provides a quick comparison between the along-track resolution afforded by SAR processing, viz. $\sqrt{2}\, a_x$, and the along-track resolution of a conventional angle-angle imager, $2\sqrt{2}\, L/ka_x$, for several transmitter beam cross-section values and far-field propagation. Advantage of the SAR over the angle-angle imager is evident in the figure.

Fig. 5.2 features a similar comparison between the cross-track resolution of a 2D SAR and that of an angle-angle imager, this time with the bandwidth B of the transmitted pulse as the key parameter. As a reference, the two resolutions are:

$$Y_{2D\ SAR} = 2/[(ka_\perp \sin \psi/L)^2 + (B\cos \psi/c)^2]^{1/2} \qquad (5.1.1)$$

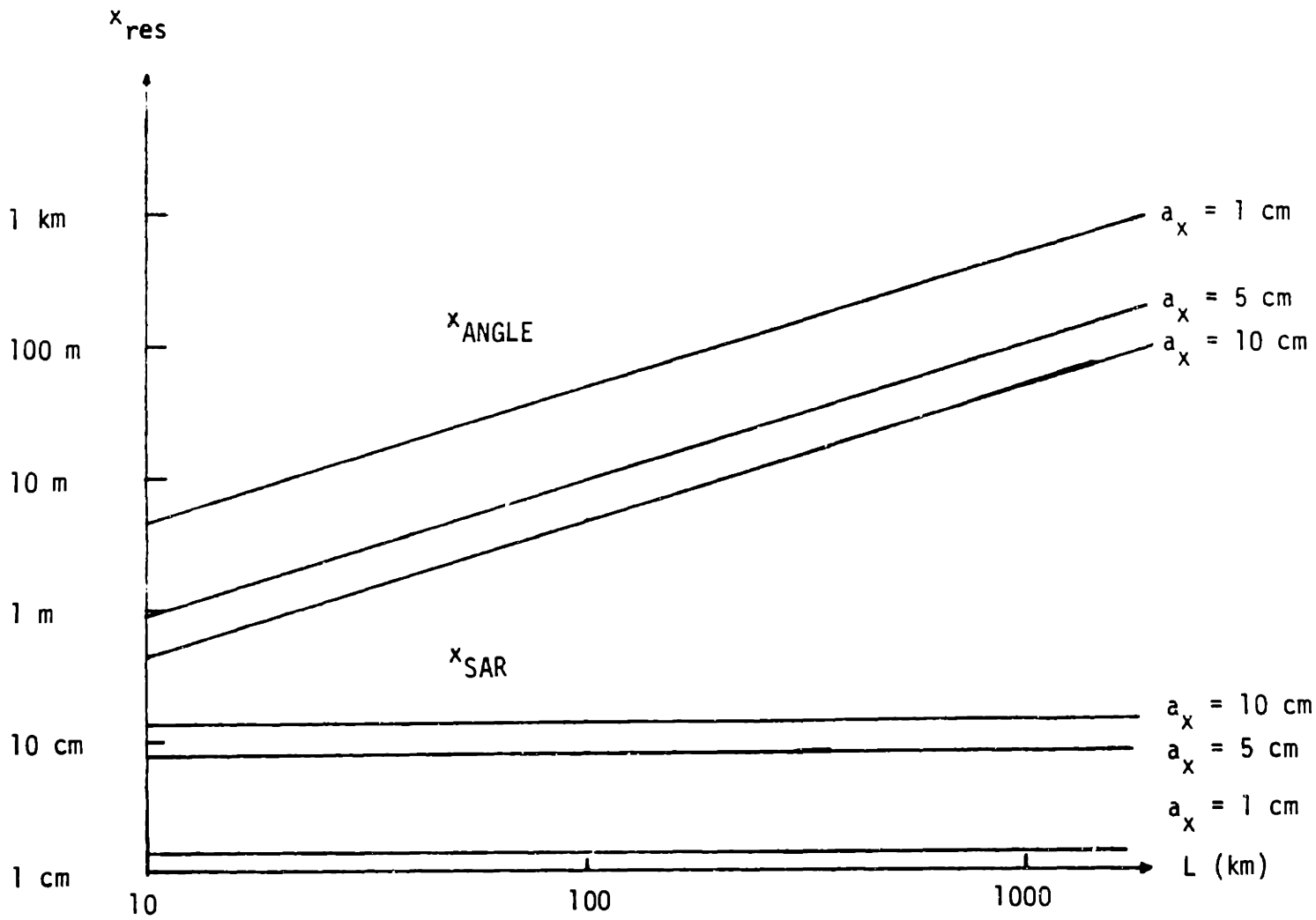and

$$Y_{ANGLE} = 2L/ka_\perp \sin \psi , \qquad (5.1.2)$$

Fig. 5.1 Comparison of SAR's Along-Track Resolution x_{SAR} and Angle-Angle Imager's Resolution x_{ANGLE} at 10.6 μm (Ideal Case)
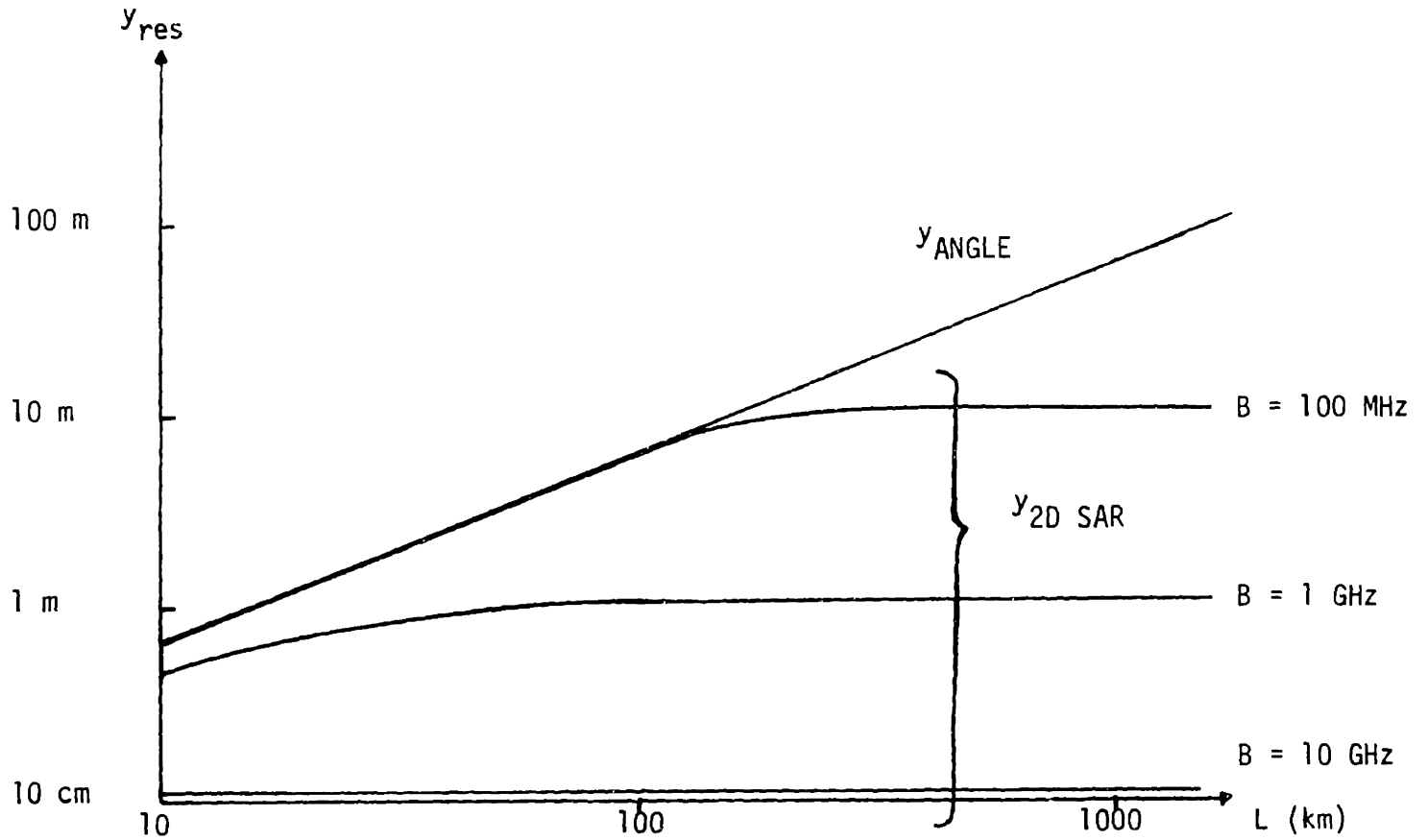
Fig. 5.2 Comparison of 2D SAR's Cross-Track Resolution $y_{2D\ SAR}$
and Angle-Angle Imager's Resolution y_{ANGLE}
at 10.6 μm (Ideal Case)

$a_{\perp} = 5$ cm, $\Psi = 60^{0}$

respectively (cf. Eqs. (3.2.42) and (3.2.14)). In the figure, we have let $\psi = 60^{\circ}$ and $a_{\perp} = 5$ cm.

While we are on the subject of bandwidth, we should point out that although a chirp bandwidth as large as 1 GHz has been demonstrated in an experimental setting [52], obtaining a wideband signal through frequency modulation in a practical setting is still quite difficult at this point. On the other hand, intense pulses of tens of ns duration or shorter - equivalent to hundreds of MHz or larger in bandwidth - can be routinely generated by existing compact lasers using Q-switching and cavity dumping [50,53]. [Modelocking can allow much shorter pulses than these but the peak power is not as high [24,53]].

We now carry out sample CNR calculations for a CW SAR. Recall that (cf. (3.2.19) and (3.2.20))

$$CNR_{CW\ SAR} = (\eta\ P_T/h\nu_0\ B_{CW\ SAR}) \cdot (A_R \varepsilon_{het} \rho /\pi L^2)$$
$$\cdot \exp[-2\alpha L]\ \varepsilon_{opt}. \qquad (5.1.3)$$

A new feature in Eq. (5.1.3) is the optical efficiency term ε_{opt}, which we have thus far ignored; it takes into account the losses arising from propagation of the laser beam through various optical elements. We take it to be 0.1 for all our CNR calculations. Other parameters are given the following values:

$a_x = 1$ cm, $a_y = 5$ cm, $v = 100$ m/s, $\eta = 0.2$, and $\rho = 0.1$.
Losses due to atmospheric attenuation are assumed to be constant at 10 dB, i.e., $\exp[-2\alpha L] = 0.1$ [since α rapidly falls off to

zero beyond 10 - 20 km in altitude and we are interested in operating our imagers beyond that range].

Fig. 5.3 is a CNR plot of the system just detailed for several values of transmitted power P_T, ranging from 10 to 200 W. It suggests that, at least from the CNR standpoint, we are fully capable of operating a CW SAR in 100-150 km range with existing compact CO_2 lasers. [CW power of close to 200 W has been achieved with compact, sealed-off CO_2 waveguide lasers [49]. CO_2 lasers built on a much larger scale, for example the MIT Firepond Laser, are capable of producing several kW power [4]; however, because of size and other restrictions, they are more suitable for ground-based RD radars than airborne SAR's.]

Fig. 5.4 displays the range dependence of 2D SAR's CNR for a set of average transmitted power (P_{ave}) values ranging from 1 W to 10 W [cf. Eqs. (3.2.39) and (3.2.40)]. Parameter values used in the figure are: $\psi = 60^{\circ}$, $a_x = 5$ cm, $a_{\perp} = 5$ cm, and B = 1 GHz. [Other parameter values are kept same as those of Fig. 5.3]. The figure indicates useful range of up to about 100 km when average power of 10 W is transmitted. In examining Fig. 5.4, however, it must be remembered that peak power constraint on pulsed laser output can seriously curtail the average transmitted power - especially when extremely short, unmodulated pulses are used - thus limiting the CNR.

Moving on to RD radars, we have plotted in Fig. 5.5 the cross-range resolution of a RD radar as a function of coherent integration time T for a set of target rotation rates. The
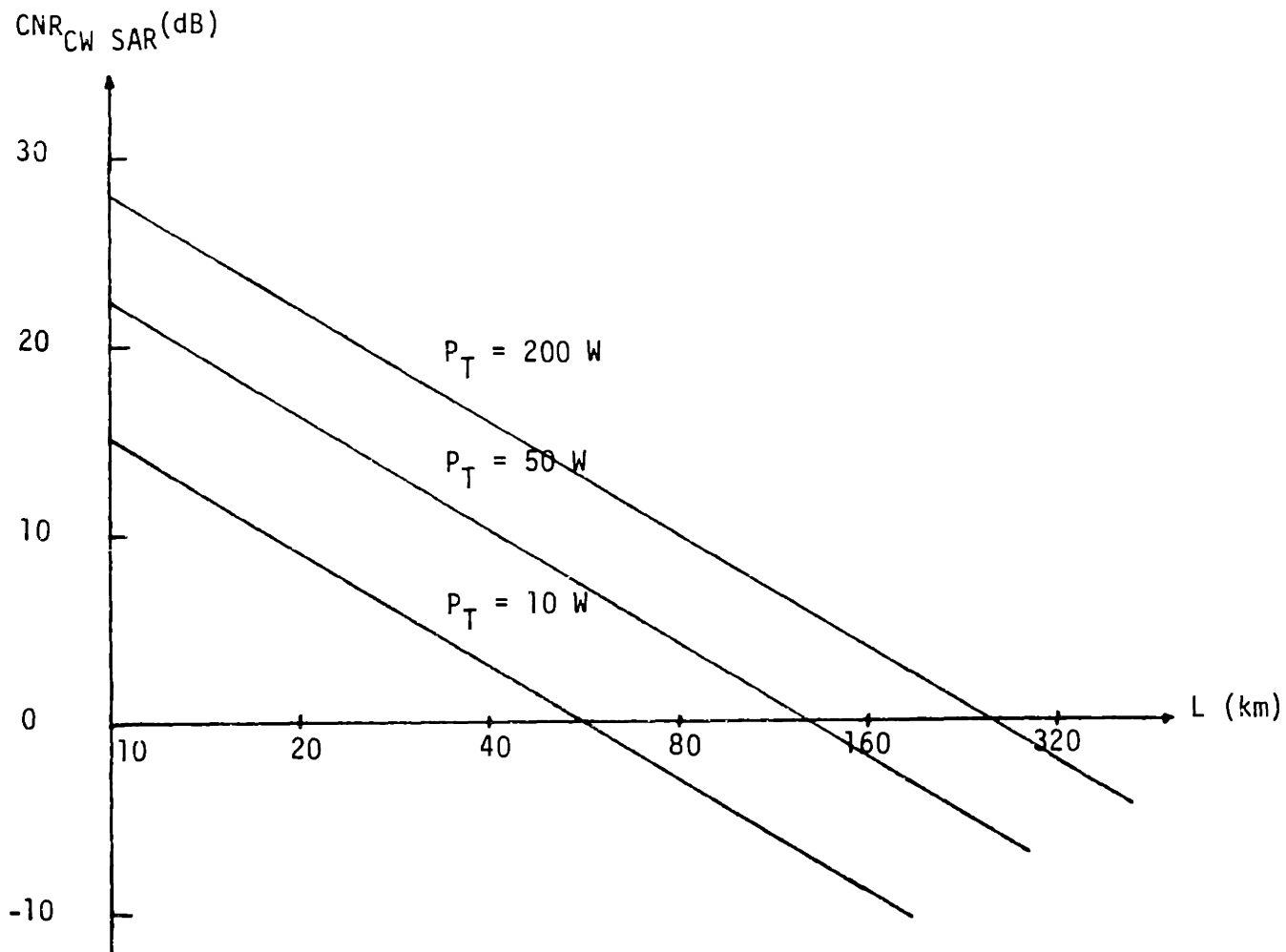
$CNR_{CW\ SAR}(dB)$

Fig. 5.3 CW SAR's CNR, $CNR_{CW\ SAR}$, vs. Range L (Ideal Case)

λ = 10.6 μm, v = 100 m/s, a_x = 1 cm, a_y = 5 cm,
η = 0.2, ρ = 0.1, ϵ_{opt} = 0.1, exp[-2αL] = 0.1
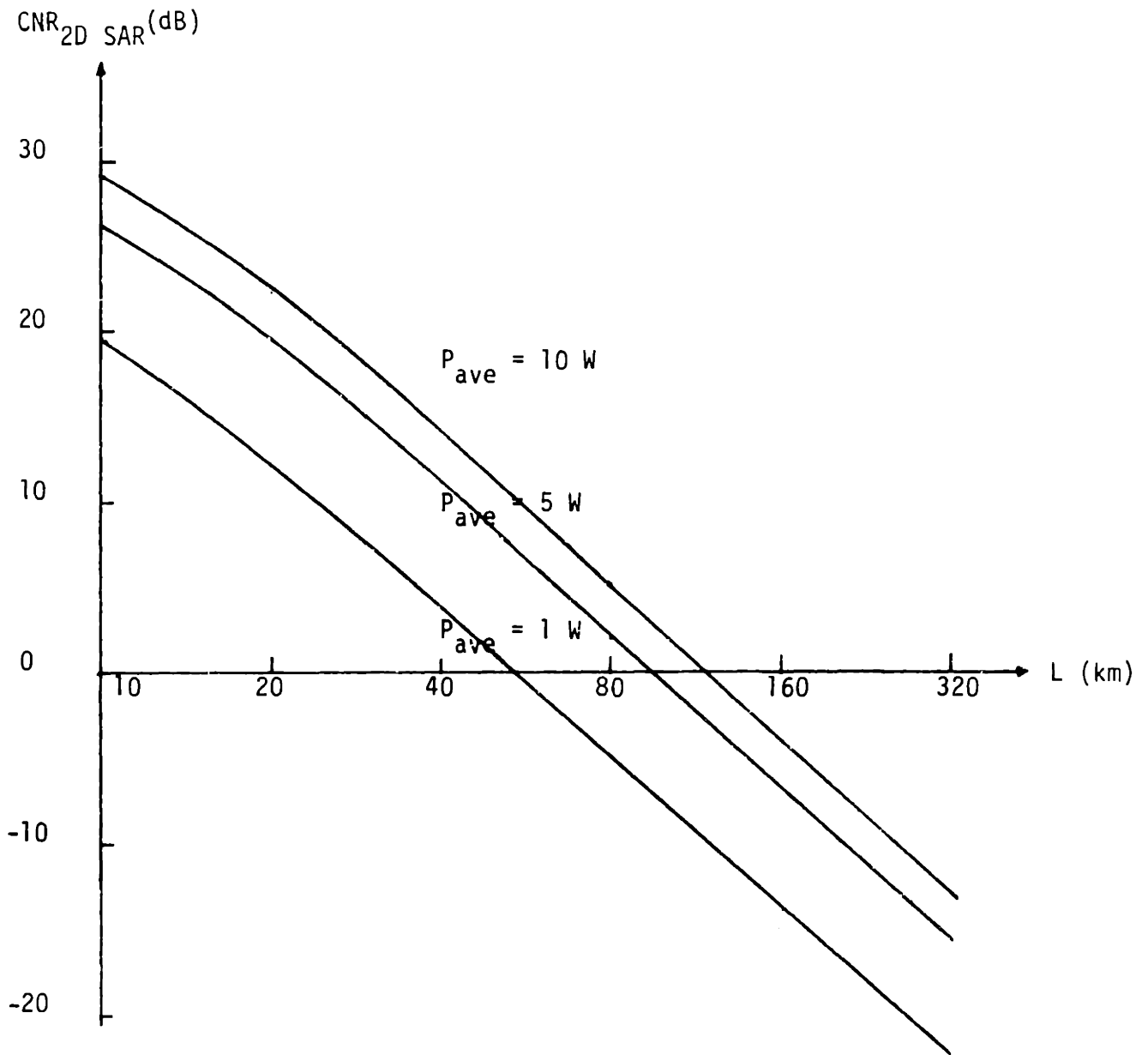
Fig. 5.4 2D SAR's CNR, $CNR_{2D\ SAR}$, vs. Range L (Ideal Case)

$\lambda = 10.6$ m, v = 100 m/s, $a_x = 5$ cm, $a_\perp = 5$ cm

$\eta = 0.2$, $\rho = 0.1$, $\epsilon_{opt} = 0.1$, $\exp[-2\alpha L] = 0.1$
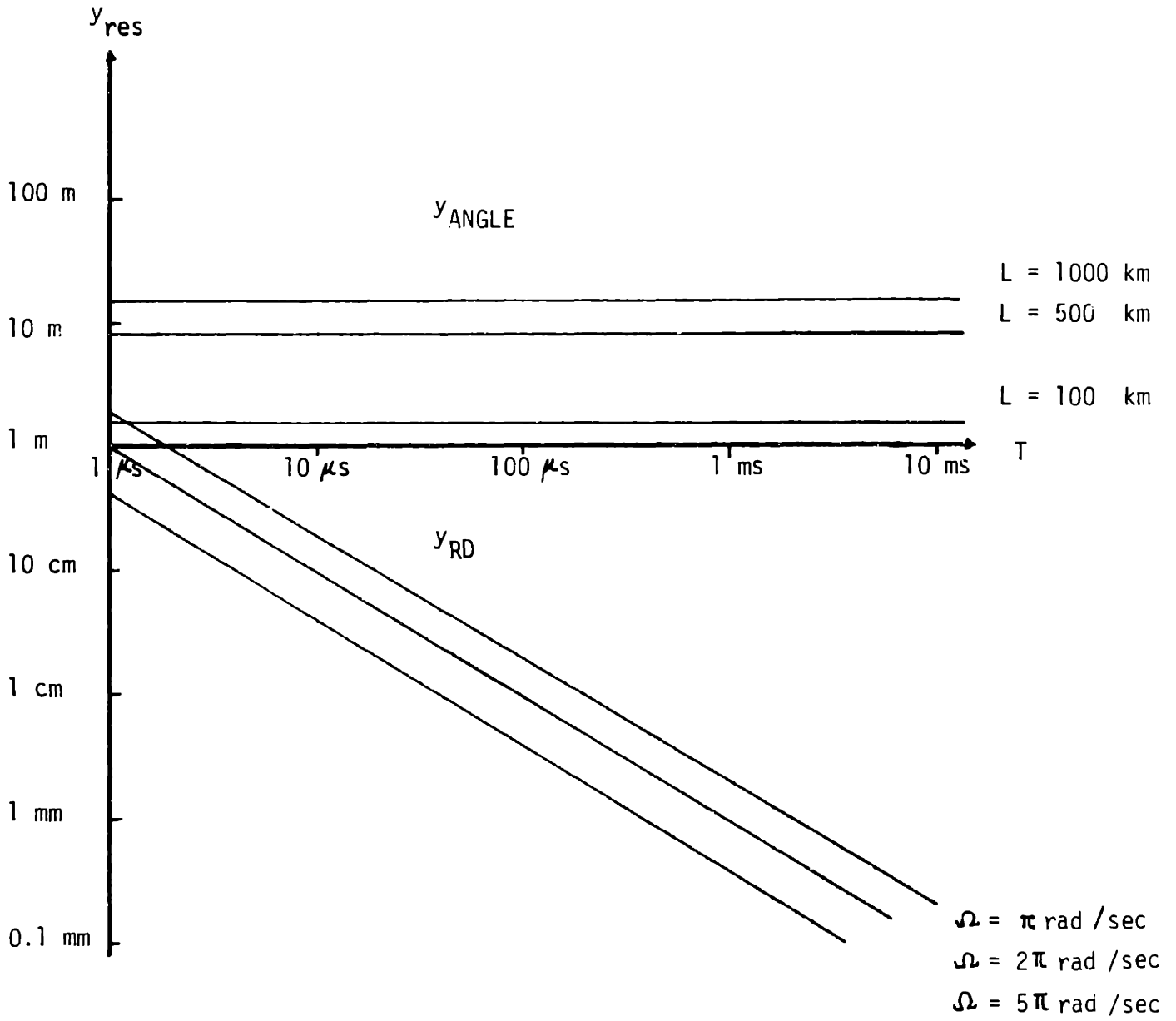
B = 1 GHz, $\psi = 60^0$

Fig. 5.5 RD Radar's Cross-Range Resolution y_{RD} vs.
Coherent Integration Time T (Ideal Case)

$\lambda = 10.6 \mu m$, $a_y = 20$ cm

figure, based on Eq. (3.3.27)

$$Y_{RD} = 2 \lambda / \pi \Omega T \qquad\qquad (5.1.4)$$

also includes, as a reference, diffraction-limited resolutions
at various ranges for a_y equal to 20 cm. Note that shortness of
the infrared wavelength affords the RD radar extremely sharp
cross-range resolution compared to the angle-angle imager of
equal aperture size, even with a short coherent integration time.
For example, with $\Omega = \pi$ rad/sec, $T = 100$ µs, and $L = 100$ km in
the figure, the angle-angle imager's resolution is 1.6 m, whereas
the RD radar's resolution is only 2 cm! This feature and the
fact that RD radar's coherent integration time is independent of
range - whereas SAR's grows linearly with the range - make RD
radars much more robust than SAR's with respect to laser
frequency instabilities and atmospheric turbulence [as will be
seen below].

5.2. Frequency Instability Case

This section looks at the effects of laser frequency
drifting on some sample high-resolution radars.

Fig. 5.6 shows the range dependence of SAR's along-track
resolution according to Eqs. (4.1.13) - (4.1.16). Parameter
values used in the figure are: $a_x = 5$ cm, $v = 100$ m/s, $\sigma_f = 1$
kHz, and $t_f = 50$ ms [this sort of frequency stability can be
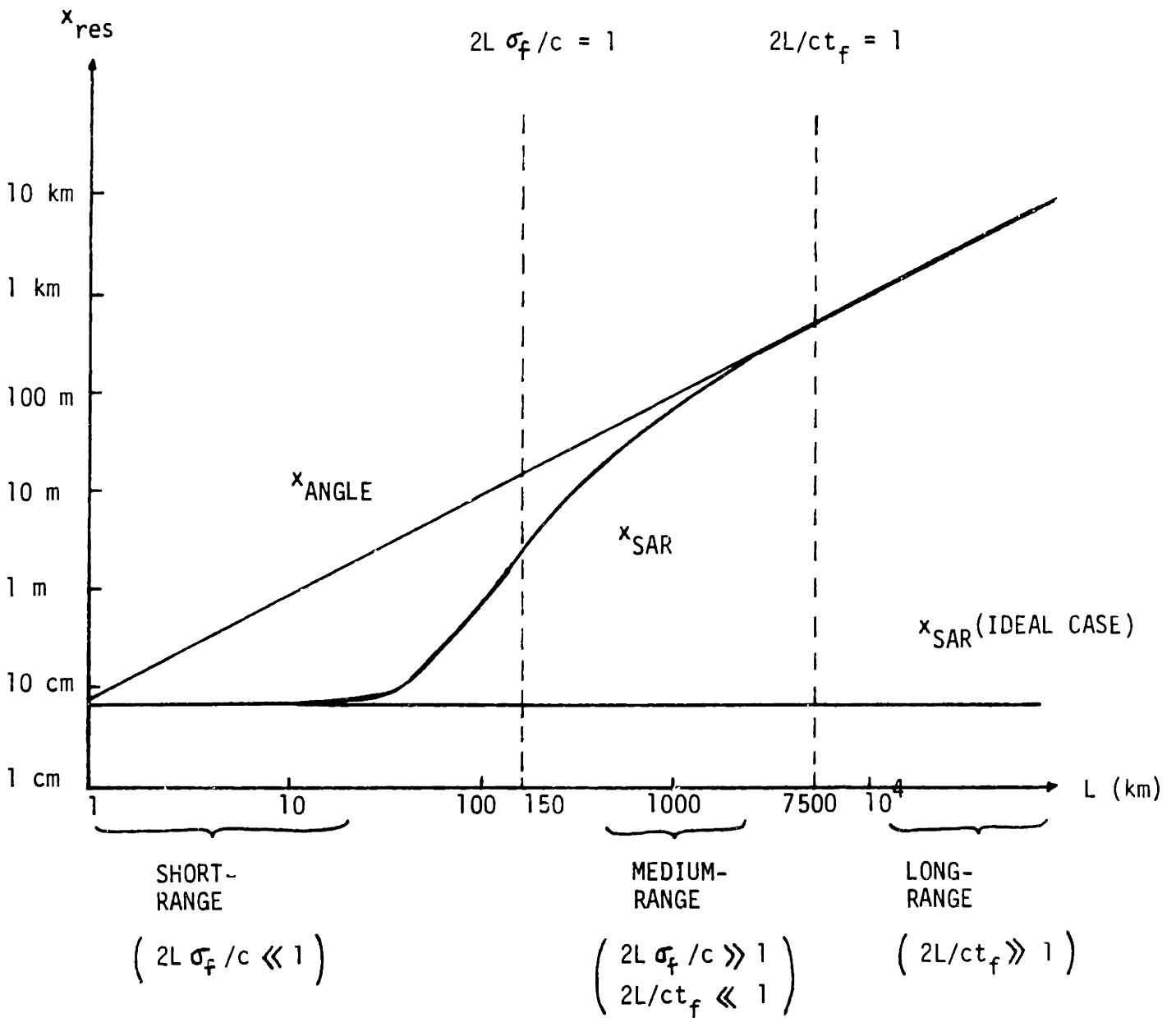
Fig. 5.6   SAR's Along-Track Resolution x_{SAR} in the Presence of Frequency Instability

$\lambda = 10.6\ \mu m$, $a_x = 5$ cm, $v = 100$ m/s

$\sigma_f = 1$ kHz, $t_f = 50$ ms

realized without too much difficulty]. In addition, we have also plotted in the same figure the along-track resolution of an angle-angle imager under equivalent conditions.

Surveying Fig. 5.6, we note that the SAR's along-track resolution remains close to its ideal value up to a substantial range - between 30 and 50 km - and only when the range is in the vicinity of 1500 km, does the resolution approach that of the angle-angle imager. This result is quite encouraging for the airborne SAR application.

Next, cross-range resolution behavior of a RD radar is examined. Fig. 5.7 displays the RD radar's (normalized) cross-range resolution behavior for a set of coherent integration time (T) values ranging from 1 µs to 100 ms. The values of σ_f and t_f are 5 kHz and 10 ms, respectively, and the normalization constant y_0 is the (laser frequency) drift-bandwidth-limited resolution $2 \lambda \sigma_f / \Omega$. It is evident from the figure that excellent cross-range resolution can be obtained despite laser frequency instability; for example, if we employ a coherent integration time longer than 0.1 ms when $\Omega = 2\pi$ rad/sec, the worst possible resolution - the drift-bandwidth-limited resolution - is still only 1.6 cm!

Let us now address the effects of frequency jitter on other performance measures such as cross-track resolution (2D SAR), range resolution (RD), and CNR. As far as the first two are concerned, little losses are expected since in most cases duration of each transmitted pulse is apt to be much shorter than
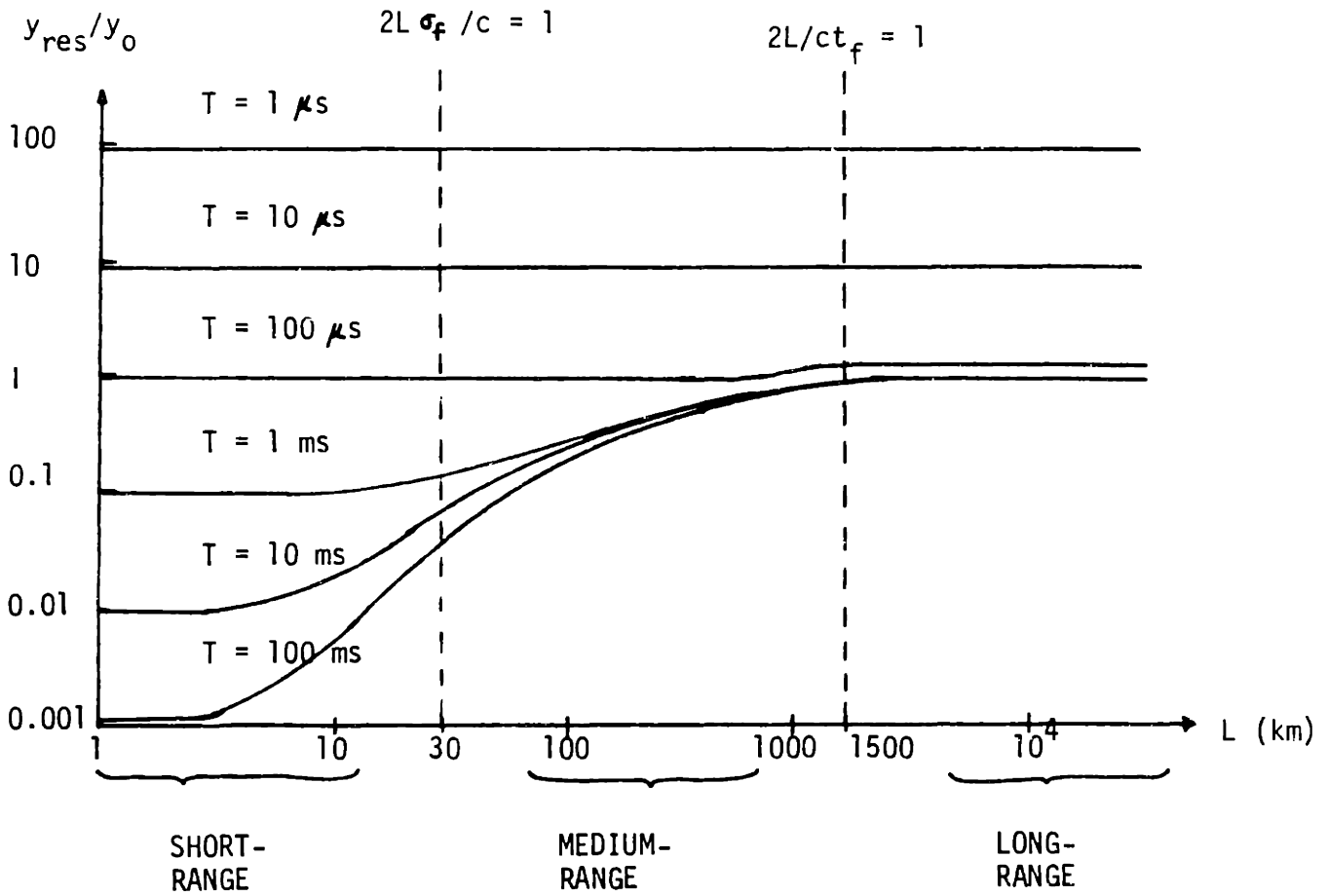
Fig. 5.7 RD Radar's (Normalized) Cross-Range Resolution
in the Presence of Frequency Instability

$$\lambda = 10.6\,\mu m, \quad \sigma_f = 5 \text{ kHz}, \quad t_f = 10 \text{ ms}$$

$$y_o = 2\lambda\sigma_f / \Omega$$

the frequency instability correlation time.

If we assume that the cross-track and range resolution losses are negligible, then the CNR losses for SAR's and RD radars can be attributed solely to the loss of the along-track and cross-range resolutions, respectively. In that case, analysis of Section 4.1 states that for SAR, any appreciable CNR loss - if at all - occurs well past the resolution breakpoint. In the long-range regime, the CNR loss factor assumes the asymptotic form $1/[1 + (\sqrt{2}\,\pi\sigma_f/(v/a_x))^2]^{1/2}$ (obtained by combining Eqs. (4.1.19), (4.1.16), (4.1.6c), and (3.2.14)). For the case of Fig. 5.6, its value is 0.41. So, the SAR's CNR loss, while not insignificant, is quite manageable.

Frequency instability of this magnitude (a few kHz in drift bandwidth) should present even less of a problem insofar as RD radar's CNR is concerned because of large Doppler bandwidths generated by rotating targets. For example, if the target dimension D_y = 1 m, Ω = 2π rad/sec, and λ = 10.6 µm, then the Doppler bandwidth, taken as $\Omega D_y/\lambda$, is hundreds of kHz, much greater than the drift bandwidth; thus the CNR loss due to frequency instability - via frequency broadening of the target return - is minimal.

This completes the section on the effects of laser frequency instability on optical SAR's and RD radars. The calculations carried out in this section indicate that lasers whose frequency stability is a few kHz in drift bandwidth and tens of ms in coherence time are quite adequate for use in high-resolution imagers.

5.3. Atmospheric Turbulence Case

In this section, we estimate the effects of atmospheric turbulence on the performance of downlooking SAR's and uplooking RD radars for a specific turbulence model. In particular, we shall look into the impact the turbulence has on the along-track resolution (SAR), the cross-range resolution (RD), and the CNR.

We start by presenting a model atmospheric turbulence height profile. The following c_n^2 profile, while being much simpler than a typical profile, nevertheless, captures its essential features [9]:

$$
c_n^2(h) = \begin{cases}
1.5 \times 10^{-14} & \text{for } 0 \quad \leq h \leq 10 \text{ m} \\
(1.5 \times 10^{-13})/h & \text{for } 10 \text{ m} \leq h \leq 20 \text{ km} \\
[\text{h in meters}] & \\
0 & \text{for } h > 20 \text{ km}
\end{cases} \tag{5.3.1}
$$

In the equation above, h is the altitude with respect to sea level and the unit of c_n^2 is $m^{-2/3}$.

Using this model, we shall now calculate the resolution and the CNR losses for airborne SAR configuration. We will assume that the short-range situation described in Section 4.2.1 prevails.

A key quantity in determining the along-track resolution and CNR loss is the transmitter(radar)-plane coherence length. Substituting the c_n^2 profile given by (5.3.1) into Eq. (4.2.10),

we obtain the following expression for the transmitter-plane coherence length p_o^T:

$$p_o^T = \begin{cases} 3.9 \text{ m} & \text{for } L \leq 20 \text{ km} \\ (1.95 \times 10^{-4})L & \text{for } L > 20 \text{ km}, \end{cases} \qquad (5.3.2)$$

[L in meters]

for wavelength of 10.6 μm, and vertical line-of-sight between the radar and the target [For 2D SAR configuration, p_o^T above is simply scaled by csc ψ , where ψ is the lookdown angle introduced in Section 3.2.2]. It is assumed that L is much greater than 10 m, whereby the contribution of the thin turbulent layer near the ground is negligible.

The calculated coherence length above is quite large compared to typical transmitter beam dimensions expected for airborne SAR's, and consequently, there should be little beam spreading.

In Fig. 5.8, we have sketched the range dependence of SAR's along-track resolution (x_{SAR}) using the turbulence profile of (5.3.1) [based on Eqs. (4.2.28)-(4.2.30)]. The parameter values used in the figure are: $v = 100$ m/s, $\bar{u} = -\hat{x}$ 10 m/s, and $a_x = 5$ cm, where the prescribed $\bar{u}$ term represents a 10 m/s wind blowing in the opposite direction as the radar motion. As usual, angle-angle imager's diffraction-limited resolution (x_{ANGLE}) is included for comparison. Note that the SAR's along-track resolution is far superior to the angle-angle imager's resolution
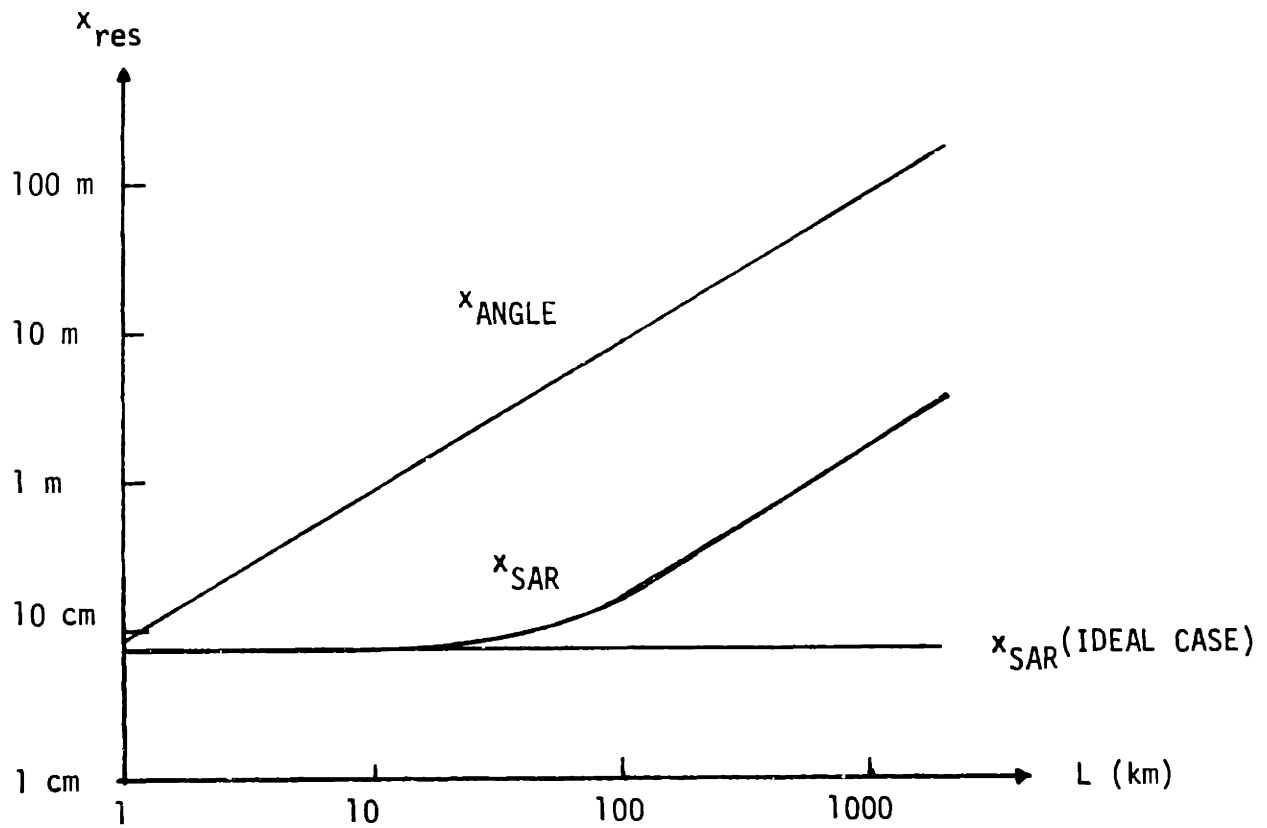
Fig. 5.8   SAR's Along-Track Resolution x_{SAR} in the Presence of
Atmospheric Turbulence

$\lambda = 10.6 \ \mu m, \quad a_x = 5 \ cm, \quad v = 100 \ m/s, \quad \bar{u} = -\hat{x} \ 10 \ m/s$

for all ranges.

Let us now examine the SAR's CNR loss behavior. As pointed out previously, CNR loss of a SAR in the presence of atmospheric turbulence is mainly caused by beam spreading. For the case we are considering, beam spreading is quite negligible, and thus, the CNR loss is minimal.

Next, we look at the effects of turbulence on ground-based RD radars. This requires us to take into account both the transmitter and the target plane coherence length because the former determines the extent of beamspreading - and thus the CNR loss - whereas the latter determines, in part, the extent of cross-range resolution loss due to target rotation. As with the SAR calculations above, we assume that the short-range regime prevails; in addition, we also assume that the turbulence motion due to wind is negligible. We start with the cross-range resolution analysis.

Since the target plane coherence length here is just the transmitter plane coherence length for the SAR configuration encountered earlier, the target return coherence time - for a point scatterer - based on the target plane coherence length is simply (cf. (4.2.51)):

$$t_o = 2p_o^T/\Omega \ |z_o| \ ,$$

where   (5.3.3)

p_o^T = coherence length given by (5.3.2)

Ω = target rotation rate

z_o = range coordinate of a scatterer on the target (deviation from the nominal target range).

Let us plug in some numbers. If we take the target dimension in the range direction to be 1 m and Ω to be 20π rad/sec, then the minimum t_o value - corresponding to the minimum p_o^T value of 3.9 m and the maximum z_o value of 1 m - is about 0.12 s, more than adequate to yield a superb cross-range resolution (cf. Fig. 5.5). In fact, even if we assume a 10 m/s wind, the turbulence decorrelation time due to that wind turns out to be quite long - 0.16 s - and the overall picture does not change too much. Therefore, atmospheric turbulence hardly presents a problem in terms of RD radar's cross-range resolution.

We now examine the RD radar's CNR loss due to beam spreading [recall that beam spreading leads to a smaller fraction of the transmitter power illuminating the spatially unresolved target]. To estimate the extent of beam spreading, we need to compute the transmitter plane coherence length. By using the c_n^2 profile given by (5.3.1) in Eq. (4.2.10), we find that the approximate coherence length at 10.6 μm wavelength decreases monotonically, from about 1.23 m at L = 1 km to the asymptotic value of 79 cm for L >> 20 km. This result is quite pleasing; it predicts that, for the given c_n^2 profile, significant beam spreading is unlikely.

This brings us to the end of Section 5.3. The main conclusion we can draw from the sample calculations in this section is that light-to-moderate atmospheric turbulence does not

cause a major problem for airborne SAR's and ground-based RD radars.

5.4. Motion Error Case

Here, we assess the extent of performance loss caused by aim error and target/radar platform vibration, based on the analysis of Section 4.3 and a set of plausible numbers.

Suppose we have a laser radar whose transmitter beam dimensions are on the order of 10 cm. The angular beamwidth of this beam in the far-field at 10.6 μm wavelength is about 0.1 mrad. Now, from the analysis of Section 4.3.1, we know that it is best to limit the transmitter aim error to less than this angular beamwidth. Fortunately this kind of aim accuracy - even with an airborne radar - is attainable with a gyroscopically stabilized optics head [54], and thus, we do not expect aim error to be a major problem.

On the other hand, aircraft vibrations are likely to be much more difficult to control and their consequences much more damaging. For example, a 2 kHz vibration with only 1 mm amplitude can introduce an optical phase change of 400 π rad in 1 ms at 10.6 μm (cf. (4.3.23)). Given that a typical coherent integration time for SAR runs easily into tens of ms for the ranges discussed in earlier sections, we can expect a significant resolution loss even with this weak vibration. In fact, with only 1 mm vibration amplitude and 10 ms coherent integration

time, the vibration frequency must be of the order of 1 Hz for the quasi-static case to prevail with certainty (see Eq. (4.3.31)). Similarly, if we assume a random vibration with parameters σ_d = 1 mm and t_d = 10 ms, the correlation time t_v, as defined by Eq. (4.3.38), at 10.6 μm turns out to be only about 0.02 ms under the model used in Section 4.3.2, which all but guarantees large resolution and CNR losses. Clearly, vibration is potentially a very serious problem and must be dealt with [for example, by measuring it with an optical sensor and cancelling its effect from the target return prior to IF processing].

We may add that vibration should be less of a problem for ground-based RD radars than for airborne SAR's because: one, it ought to be easier to isolate a ground-based radar from various vibrations; and two, RD radars tend to employ shorter coherent integration times.

This concludes our cursory look at the type of performance we may expect with optical airborne SAR's and ground-based RD radars under a variety of operating conditions. Calculations indicate that laser frequency instability and atmospheric turbulence do not pose prohibitive problems. On the other hand, vibration of the target/radar platform is seen as a very serious problem, especially for the SAR. If the imager's full potential is to be realized, we must have very sensitive vibration measurements, along with appropriate compensations.

On a more general note, we need improvements in several key

technologies to make these imagers more feasible. Some of those
needs, as perceived in our analyses, are: more stable and
powerful lasers, faster and more efficient photodetectors, and
precision sensors to monitor various motion errors. It is
encouraging, however, that rapid improvements have been made
within last ten to fifteen years in these areas and that they are
expected to continue in the future, and we are hopeful that the
optical SAR's and RD radars can fill the need of extremely
high-resolution imaging that microwave radars cannot provide.
The ground-based RD radars, in particular, seem quite promising;
in fact, a pilot RD radar program has been carried out in mid
70's at Lincoln Laboratory [4] with moderate success.

CHAPTER VI

SUMMARY

In this thesis, we examined SAR's and RD radars in the optical context, studying their performance under both ideal and nonideal operating conditions. In particular, we concentrated our efforts on analyzing the effects of various factors that are either unique or particularly significant at optical frequencies, such as laser frequency drifting, atmospheric turbulence, and motion errors.

Here, we summarize the thesis and present a list of future work that could be carried out.

In Chapter II, we presented a system model for the high-resolution radars following the usual laser radar theory for angle-angle imagers: models for transmitter, propagation in clear weather, target-beam interaction, and heterodyne detection were established.

In Chapter III, the following performance measures for SAR's and RD radars were derived under ideal operating conditions: spatial resolution, CNR, and SNR. Two types of SAR's were considered; those with temporal modulation of the transmitted beam (2D) and those without (CW). Analysis of RD radars was also divided into two parts according to the type of IF processing used.

In Chapter IV, we evaluated the imagers' performances under

more realistic scenarios. Specifically, we let the systems be subjected to laser frequency instability, atmospheric turbulence, radar aim error, and target/radar platform vibrations. For each of these cases, we assumed a simple but physically reasonable model and interpreted the results.

In Chapter V, we used the results of the previous chapters to carry out sample calculations of the system performance for two specific imaging configurations: downlooking airborne SAR and uplooking ground-based RD radar.

The main accomplishments of this thesis are that it quantifies the effects of various important phenomena on the performance of optical high-resolution imagers and provides a physical understanding of these effects. In doing so, we have also demonstrated that these imagers may be feasible in the near future.

Despite these achievements, there remains much work that can be done to improve our understanding of high-resolution laser radars. Some key issues are:

1)   Relaxation of some of the assumptions. For example, the target could be modelled as a composite of speckle and glint targets instead of a pure speckle target.

2)   Performance optimization. One may look into choosing the system parameters in such a way that the performance is

optimized for a given operating environment.

3) Investigation of alternative/additional processing architectures. For example, one may consider using autodyne detection [5,55] instead of heterodyne detection to minimize the effects of frequency instability and/or platform vibration, or applying spatial filtering to reduce target speckle.

4) Refinement of perturbation models. One may, for example, use a more accurate and elaborate frequency drift model or atmospheric turbulence profile to better reflect the reality.

APPENDIX A: Computation of $< | Q'(x,y,m,\tau) |^2 >$

[cf. (4.1.24) of Section 4.1.2]

$$< | Q'(x,y,m,\tau) |^2 > = \iint d\tau' d\tau'' \ \underline{f}^*(\tau-\tau') \ \underline{f}(\tau'-2y\cos\psi/c)$$

$$\cdot \ \underline{f}(\tau-\tau'') \ \underline{f}^*(\tau''-2y\cos\psi/c)$$

$$\cdot \sum_{m=-\infty}^{\infty} \sum_{m'=-\infty}^{\infty} \exp[-(ja_1+a_2)(m-m')^2 + (ja_1-a_2)(m-m'')^2]$$

$$\cdot \exp[+(ja_1-a_2)(\tilde{x}-m')^2 - (ja_1+a_2)(\tilde{x}-m'')^2]$$

$$\cdot R_{ww}((m'-m'')T_s+(\tau'-\tau'')), \qquad (A.1)$$

where

$$a_1 \equiv (k/L)(vT_s)^2$$

$$a_2 \equiv 2(ka_x/2L)^2(vT_s)^2$$

$$\tilde{x} \equiv x/vT_s \qquad\qquad (A.2)$$

$$R_{ww}(u) = \text{correlation function of } \underline{w}(t)$$

$$[\ \exp[-8(u/t_\theta)^2] \ \text{assumed} \ ].$$

In the above expression, we have dropped the τ' and τ'' dependences from $\tilde{x}$ since they are negligible. We will continue to assume that $\underline{f}(t) = \exp[-j\pi W_0 t^2/T_0 - 4(t/T_0)^2]$.

By expanding R_{ww} in terms of $(m'-m'')T_s$ and $\tau'-\tau''$, and using nge of variables, the $\tau'-$ and $\tau''-$ integrals may collectively be approximated by the following:

$$(\pi T_0^2/8\varepsilon_a) \ \exp[-((\pi W_0/\varepsilon_a)^2 + (4/T_0)^2)\cdot(\cos\psi/c)^2$$

$$\cdot(y-c\tau/2\cos\psi)^2] \qquad\qquad (A.3)$$

$$\cdot \exp[-2j(\pi W_o/T_o)\cdot(2y\cos\psi/c - \tau)(m'-m'')T_s$$
$$/ (1 + (t_\theta/T_o)^2/2)]$$
$$\cdot \exp[8(T_s/t_\theta)^2(m'-m'')^2/(1 + (t_\theta/T_o)^2/2)],$$

where

$$\varepsilon_a \equiv [1 + 2(T_o/t_\theta)^2]^{1/2}. \qquad (A.4)$$

Taking into account the m'- and m''-dependent terms of (A.3), we can express the m'- and m''- summations in the following form:

$$\exp[-2a_2(m^2 + \tilde{x}^2)]\cdot\{ \sum_{m_s} \sum_{m_d} \exp[-2jm_d(a_1(\tilde{x} - m)$$
$$+ (\pi W_o/T_o)T_s(2y\cos\psi/c - \tau))/(1 + (t_\theta/T_o)^2/2)]$$
$$\cdot\exp[-a_2(m_s^2 - 2m_s(m + \tilde{x}) + m_d^2)]$$
$$\cdot\exp[-m_d^2(2T_s/T_o)^2/(1 + (t_\theta/T_o)^2/2)]\}, \qquad (A.5)$$

where

$$m_s \equiv m' + m''$$
$$m_d \equiv m' - m'', \qquad (A.6)$$

and the summations are taken over integer values of m_s and m_d such that sum of m_s and m_d is an even number. These summations in turn can be written as a sum of two double summations which we shall denote by S_1 and S_2. S_1 is the result of summing the terms of (A.5) over all integer values of m_s and m_d with the m_s and m_d in (A.5) replaced by $2m_s$ and $2m_d$, respectively. S_2 is exactly same as S_1 except that m_s and m_d are replaced by $2m_s + 1$ and $2m_d + 1$, respectively.

After some algebra, we find S_1 to be

$$S_1 = (\pi/4a_2\varepsilon_b) \cdot \exp[-a_2(m - \tilde{x})^2] \tag{A.7}$$

$$\cdot \{ \sum_{l'=-\infty}^{\infty} \exp[-(2\pi l')^2/16a_2] \exp[-j(m + \tilde{x})\pi l'] \}$$

$$\cdot \{ \sum_{l''=-\infty}^{\infty} \exp[-(a_1^2/\varepsilon_b^2 a_2) \cdot (\tilde{x} - m + \pi l''/2a_1$$

$$+ (\pi W_O/T_O)T_S(2y\cos\psi/c - \tau)/a_1(1 + (t_\Theta/T_O)^2/2))^2]$$

where

$$\varepsilon_b \equiv [1 + (2T_S/T_O)^2/a_2/(1 + (t_\Theta/T_O)^2/2)]^{1/2}. \tag{A.8}$$

S_2 is given by the same expression as (A.7) except that in the l'- and l"-summations there are extra terms of $(-1)^{l'}$ and $(-1)^{l''}$, respectively, in the summands.

APPENDIX B: Computation of $< \underline{F}(\bar{p}, \tau') \; \underline{F}^*(\bar{p}, \tau") >$

[cf. (4.2.32) and (4.2.34) of Section 4.2.2]

Combining (4.2.32) and (4.2.34), we have

$$< \underline{F}(\bar{p}, \tau') \; \underline{F}^*(\bar{p}, \tau") >$$

$$= \iiiint_{z=0} d\bar{p}_1 d\bar{p}_2 d\bar{p}_3 d\bar{p}_4 \; \{ \prod_{i=1}^{4} \exp[-(x_i/a_x)^2 - (y_i/a_y)^2] \}$$

$$\cdot \exp[-j(k/L)[(\bar{p} - \hat{x} v\tau') \cdot (\bar{p}_1 + \bar{p}_2) - (\bar{p} - \hat{x} v\tau") \cdot (\bar{p}_3 + \bar{p}_4)]]$$

$$\cdot \exp[- |(\bar{p}_1 - \bar{p}_3) - \hat{x} v\Delta\tau|^2 / 2p_o^2]$$

$$\cdot \exp[- |(\bar{p}_2 - \bar{p}_4) - \hat{x} v\Delta\tau|^2 / 2p_o^2]. \tag{B.1}$$

Using the following coordinate transformations

$$\bar{p}_{as} = \bar{p}_1 + \bar{p}_3 \qquad\qquad \bar{p}_1 = (\bar{p}_{as} + \bar{p}_{ad})/2$$

$$\bar{p}_{ad} = \bar{p}_1 - \bar{p}_3 \qquad\qquad \bar{p}_3 = (\bar{p}_{as} - \bar{p}_{ad})/2 \tag{B.2}$$

$$\bar{p}_{bs} = \bar{p}_2 + \bar{p}_4 \qquad\qquad \bar{p}_2 = (\bar{p}_{bs} + \bar{p}_{bd})/2$$

$$\bar{p}_{bd} = \bar{p}_2 - \bar{p}_4 \qquad\qquad \bar{p}_4 = (\bar{p}_{bs} - \bar{p}_{bd})/2,$$

we can rewrite some of the terms in (B.1) as follows:

$$\prod_{i=1}^{4} \{\exp[-(x_i/a_x)^2 - (y_i/a_y)^2]\}$$

$$= \exp[-(1/2a_x^2)(x_{as}^2 + x_{ad}^2 + x_{bs}^2 + x_{bd}^2)] \tag{B.3}$$

$$\cdot \exp[-(1/2a_y^2)(y_{as}^2 + y_{ad}^2 + y_{bs}^2 + y_{bd}^2)],$$

$$\exp[-j(k/L)[(\bar{p} - \hat{x} v\tau') \cdot (\bar{p}_1 + \bar{p}_2) - (\bar{p} - \hat{x} v\tau") \cdot (\bar{p}_3 + \bar{p}_4)]]$$

$$= \quad \exp[-j(k/L)\{(x_{as} + x_{bs})(v_\Delta\tau/2)$$
$$+ (x_{ad} + x_{bd})(x - v(\tau' + \tau'')/2) + (Y_{ad} + Y_{bd})y\}], \quad (B.4)$$

$$\exp[- \ |(\bar{p}_1 - \bar{p}_3) - \hat{x} \ v \ _\Delta\tau|^2 / \ 2p_o^2]$$
$$\exp[- \ |(\bar{p}_2 - \bar{p}_4) - \hat{x} \ v \ _\Delta\tau|^2 / \ 2p_o^2]$$

$$= \quad \exp[-(v \ _\Delta\tau/p_o)^2] \quad\quad\quad\quad\quad (B.5)$$
$$\cdot\exp[-(1/2p_o^2)[\ x_{ad}^2 - 2x_{ad} \ (v \ _\Delta\tau) + y_{ad}^2$$
$$+ x_{bd}^2 - 2x_{bd} \ (v \ _\Delta\tau) + y_{bd}^2]].$$

Collecting these terms gives us

$$< \underline{F}(\bar{p},\tau') \ \underline{F}^*(\bar{p},\tau'') >$$
$$= \quad (1/16) \ \exp[-(v \ _\Delta\tau/p_o)^2]$$
$$\cdot\iint dx_{as}dy_{as} \ \exp[-x_{as}^2/2a_x^2] \ \exp[-j(kv \ _\Delta\tau/2L) \ x_{as}] \ \exp[-y_{as}^2/2a_y^2]$$
$$\cdot[\ \text{ditto for } x_{bs}\text{- and } y_{bs}\text{-integrals} \ ]$$
$$\cdot\int dx_{ad} \ \exp[-x_{ad}^2/2a_x^2] \ \exp[-j(k/L)(x - v(\tau'+\tau'')/2)x_{ad}]$$
$$\exp[-[x_{ad}^2 - 2x_{ad}(v \ _\Delta\tau)]/ \ 2p_o^2] \quad\quad (B.6)$$
$$\cdot\int dy_{ad} \ \exp[-y_{ad}^2/2a_y^2] \ \exp[-j(k/L)y \ y_{ad}] \ \exp[-y_{ad}^2/ \ 2p_o^2]$$
$$\cdot[\ \text{ditto for } x_{bd}\text{- and } y_{bd}\text{-integrals} \ ].$$

These integrals are easily evaluated. The end result is

$$< \underline{F}(\bar{p},\tau') \ \underline{F}^*(\bar{p},\tau'') > = (\pi a_x a_y)^4 (1/\mu_x^2\mu_y^2)$$
$$\cdot\exp[-(v \ _\Delta \ \tau)^2\{(ka_x/2L)^2 + (1/p_o\mu_x)^2\}]$$
$$\cdot\exp[-2j \ _\Delta \tau(kv/L)(a_x/\mu_x p_o)^2(x - v\tau_s)]$$
$$\cdot\exp[-(ka_x/\mu_xL)^2(x - v\tau_s)^2]$$
$$\cdot\exp[-(ka_y/\mu_yL)^2y^2], \quad\quad (B.7)$$

where

$$\mu_x^2 \equiv 1 + (a_x/P_0)^2$$
$$\mu_y^2 \equiv 1 + (a_y/P_0)^2 \tag{B.8}$$
$$\tau_s \equiv (\tau' + \tau'')/2.$$

APPENDIX C: Computation of $< I_y(t) >$

[see (4.2.25) and (4.2.35) of Section 4.2.2]

Combining Eqs. (4.2.25), (4.2.26), (4.2.35), and (4.2.36), we arrive at the following:

$$
\begin{aligned}
< I_y(t) > = & (2/\pi a_x a_y)^2 (1/\lambda L)^4 \exp[-2\alpha L] \\
& \cdot \int_{z=L} d\bar{p}\, \lambda^2\, \bar{J}(\bar{p}) \iint d\tau_s d\tau_d\, P_T \\
& \cdot \exp[-(ka_x v/L)^2 (t-\tau_s)^2 - (ka_x v/2L)^2 \tau_d^2] \\
& \cdot \exp[2j(kv/L)(x-vt)\tau_d] \\
& \cdot (1/\mu_x^2\mu_y^2)\ (\pi a_x a_y)^4 \\
& \cdot \exp[-(v\tau_d)^2\{(ka_x/2L)^2 + (1/p_o\mu_x)^2\}] \\
& \cdot \exp[-2j\tau_d(kv/L)(a_x/\mu_x p_o)^2 (x-v\tau_s)] \\
& \cdot \exp[-(ka_x/\mu_x L)^2 (x-v\tau_s)^2]\ \exp[-(ka_y/\mu_y L)^2 y^2]
\end{aligned}
\tag{C.1}
$$

where we have made use of the following change of variables

$$
\begin{aligned}
\tau_s &\equiv (\tau'' + \tau')/2 \\
\tau_d &\equiv \tau'' - \tau'
\end{aligned}
\tag{C.2}
$$

Let us carry out the τ_s-integral first.

$$
\begin{aligned}
T_s \equiv \int_{-\infty}^{\infty} d\tau_s\ & \exp[-(ka_x v/L)^2 (t-\tau_s)^2] \\
& \cdot \exp[-(ka_x/\mu_x L)^2 (x-v\tau_s)^2] \\
& \cdot \exp[-2j\tau_d(kv/L)(a_x/\mu_x p_o)^2 (x-v\tau_s)].
\end{aligned}
\tag{C.3}
$$

After some manipulations, we obtain

$$T_s = [\pi\mu_x^2/(ka_x v/L)^2(1 + \mu_x^2)]^{1/2}$$
$$\cdot \exp[-(ka_x/L)^2(x-vt)^2/(1 + \mu_x^2)]$$
$$\cdot \exp[-2j(kv/L)(a_x/p_0)^2(x-vt)\tau_d/(1 + \mu_x^2)] \qquad (C.4)$$
$$\cdot \exp[-(v\tau_d)^2(a_x/\mu_x p_0^2)^2/(1 + \mu_x^2)].$$

Combining the τ_d-dependent part of (C.4) with the remaining τ_d-dependent terms of (C.1), we obtain the following result.

$$T_d \equiv \int_{-\infty}^{\infty} d\tau_d \, \exp[j\omega \, \tau_d] \, \exp[-\alpha\tau_d^2]$$
$$= \sqrt{\pi/\alpha} \, \exp[-\omega^2/4\alpha], \qquad (C.5)$$

where

$$\omega \equiv (2kv/L)(x-vt) \{ 1 - (a_x/p_0)^2/(1 + \mu_x^2)\} \qquad (C.6)$$
$$\alpha \equiv v^2\{2(ka_x/2L)^2 + 1/(p_0\mu_x)^2 + (a_x/\mu_x p_0^2)^2/(1 + \mu_x^2)\}$$

After collecting all the terms and rearranging them, we have

$$< I_y(t) > = (\sqrt{2} \, \pi a_y^2/v^2L^2) \, P_T \exp[-2\alpha L]$$
$$\cdot (1/\mu_x^2\mu_y^2) \, (\mu_x^2/(1 + \mu_x^2))^{1/2} \, (1/\eta_1)$$
$$\cdot \int_{z=L} d\bar{p} \, \mathcal{J} \, (\bar{p}) \, \exp[-(ka_y/\mu_y L)^2 y^2] \qquad (C.7)$$
$$\cdot \exp[-(ka_x/L)^2(x-vt)^2/(1 + \mu_x^2)]$$
$$\cdot \exp[-2(x-vt)^2/(\eta_2 a_x)^2]$$

where

$$\eta_1 \equiv [1 + 2(L/ka_x p_0\mu_x)^2 + 2(L/kp_0^2\mu_x)^2/(1 + \mu_x^2)]^{1/2}$$
$$\eta_2 \equiv \eta_1 /(1 - (a_x/p_0)^2/(1 + \mu_x^2)) \qquad (C.8)$$

APPENDIX D: Computation of $< I_y(t) >$ Based on a Stochastic

Model for Transmitter Aim Error.

[cf. Section 4.3.1]

From (4.3.4), we have

$$
\begin{aligned}
< I_y(t) > &= <|\underline{1}_y(t)|^2> \\
&= P_T(k^2 a_x a_y/2\pi L^2)^2 \; \lambda^2 \exp[-2\alpha L] \int d\bar{p} \; \mathcal{J}(\bar{p}) \Big|_{z=L} \\
&\quad \cdot \int\int d\tau_1 d\tau_2 \; \exp[-(2(ka_x/2L)^2 + j(k/L))(vt - v\tau_1)^2] \\
&\qquad \cdot \exp[-(2(ka_x/2L)^2 - j(k/L))(vt - v\tau_2)^2] \\
&\qquad \cdot \exp[j(k/L)((x-v\tau_1)^2 - (x-v\tau_2)^2)] \\
&\quad \cdot E\{ \exp[- 2(ka_x/2L)^2[(x-v\tau_1-L\Phi_x\Theta(\tau_1))^2 \\
&\qquad\qquad + (x-v\tau_2-L\Phi_x\Theta(\tau_2))^2] \\
&\quad \cdot \exp[- 2(ka_y/2L)^2[(y-L\Phi_y\Theta(\tau_1))^2 \\
&\qquad\qquad + (y-L\Phi_y\Theta(\tau_2))^2]\} \quad\quad (D.1)
\end{aligned}
$$

where we have assumed $|\Theta(t)| << 1$ for all t and replaced $\sin \Theta(t)$
by $\Theta(t)$. The E stands for expectation over the random tilt of
the transmitter plane. The determinstic exponential terms inside
the τ_1- and τ_2-integrals can be rewritten as follows:

$$
\begin{aligned}
&\exp[-2(ka_x/2L)^2(2v^2(t - \tau_s)^2 + (v\tau_d)^2/2)] \\
&\cdot \exp[-2j(kv/L)\tau_d(x-vt)], \quad\quad (D.2)
\end{aligned}
$$

where

$$
\tau_s \equiv (\tau_1 + \tau_2)/2
$$

$$
\tau_d \equiv \tau_1 - \tau_2.
$$

Similarly, the expectation term can be written as

$$
\exp[-(ka_x/L)^2(x-v\tau_s)^2 - (ka_x/2L)^2(v\tau_d)^2 - (ka_y/L)^2 y^2]
$$

$$
\cdot E\{ \exp[-2(ka_x/2L)^2 [-2(x-v\tau_s)L\Phi_x(\Theta(\tau_1) + \Theta(\tau_2))
$$

$$
+ (L\Phi_x)^2(\Theta^2(\tau_1) + \Theta^2(\tau_2)) + v\tau_d L\Phi_x(\Theta(\tau_1) - \Theta(\tau_2))]
$$

$$
-2(ka_y/2L)^2 [-2yL\Phi_y(\Theta(\tau_1) + \Theta(\tau_2))
$$

$$
+ (L\Phi_y)^2(\Theta^2(\tau_1) + \Theta^2(\tau_2))]] \}. \qquad (D.3)
$$

Computation of the expectation in (D.3) can be carried out by using the following identity [48]:

$$
\int_{-\infty}^{\infty} d\underline{x} \, \exp[-\underline{x}^T A \underline{x} + \underline{f}^T \cdot \underline{x}]
$$

$$
= [\pi^{N/2}/\sqrt{\det A}] \exp[(\underline{f}^T A^{-1} \underline{f})/4], \qquad (D.4)
$$

where

$\underline{x}$ = N-dimensional real-valued vector

$\quad = [x_1 \ x_2 \ \ldots \ldots \ x_N]^T$

A = N x N complex-valued, symmetric matrix

$\quad$ satisfying the condition Re (A) > 0

$\quad = [a_{ij}] \qquad i,j = 1, 2, \ldots, N$

$\underline{f}$ = N-dimensional, complex-valued vector

$\quad = [f_1 \ f_2 \ \ldots \ldots \ f_N]^T$.

If we assume that $\Theta(t)$ is a zero-mean, wide-sense stationary (WSS), Gaussian random process with covariance matrix

-234-

$$\Lambda \quad \equiv \mathbf{E}\{ \; \underline{\theta} \; \underline{\theta}^T \; \}$$

$$= \begin{bmatrix} \lambda_{11} & \lambda_{12} \\ \lambda_{21} & \lambda_{22} \end{bmatrix} \qquad\qquad (D.5)$$

$$= \begin{bmatrix} \sigma_{\theta}^2 & \sigma_{\theta}^2 K(\tau_d) \\ \sigma_{\theta}^2 K(\tau_d) & \sigma_{\theta}^2 \end{bmatrix}$$

where

$$\underline{\theta} \quad = \quad [\; \theta(\tau_1) \quad \theta(\tau_2) \;]^T$$

$K(\tau_d)$ = normalized covariance function of $\theta(\tau)$

σ_{θ} = standard deviation of $\theta(\tau)$,

then we may cast the calculation of the expectation term in (D.3) into the canonical form of (D.4) as follows:

$$\mathbf{E}\{ \; \exp[\; \dots \;] \; \}$$

$$= \int_{-\infty}^{\infty}\int_{-\infty}^{\infty} dx_1 dx_2 \; p_{x_1, x_2} \exp[\; \dots \;]$$

$$= \int\int dx_1 dx_2 \; [(2\pi)^2 \det{}_{\Lambda_x}]^{-1/2} \exp[\; -(\underline{x}^T \Lambda_x^{-1} \; \underline{x} \;)/2 \;] \; \exp[\; \dots \;]$$

$$= \int\int dx_1 dx_2 \; [(2\pi)^2 \det{}_{\Lambda_x}]^{-1/2} \exp[\; -(\underline{x}^T A \; \underline{x} \; \} + \underline{f}^T \cdot \underline{x} \;],$$

where $\qquad\qquad$ (D.6)

$$\underline{x} \quad \equiv \underline{\theta} \; ; \quad \Lambda_x = \Lambda$$

p_{x_1, x_2} = joint probability density function of $\underline{x}$

$$A \quad \equiv \Lambda_x^{-1}/2 + qI \qquad\qquad (D.7)$$

$$f_1 \quad \equiv (ka_x/L)^2 L\Phi_x(x - v\tau_s - v\tau_d/2) + (ka_y/L)^2 L\Phi_y y$$

$$f_2 \quad \equiv (ka_x/L)^2 L\Phi_x(x - v\tau_s + v\tau_d/2) + (ka_y/L)^2 L\Phi_y y$$

$$q \quad \equiv ((ka_x\Phi_x)^2 + (ka_y\Phi_y)^2)/2$$

I and Λ_x^{-1} are the identity matrix and the inverse matrix of Λ_x, respectively. Computing the elements of A, we get

$$a_{11} = a_{22}$$
$$= q + 1/(2\sigma_\Theta^2(1 - K^2))$$

$$(D.8)$$

$$a_{12} = a_{21}$$
$$= - K/(2\sigma_\Theta^2(1 - K^2))$$

Clearly, matrix A as defined in (D.7) meets the positive-definiteness and the symmetry requirements of (D.4).

The expectation of (D.6) can now be expressed as

$$E\{ \exp[\ldots] \}$$
$$= [4 \det \Lambda \det A]^{-1/2} \exp[(\underline{f}^T A^{-1} \underline{f})/4].$$

$$(D.9)$$

A little algebra leads to

$$[4 \det \Lambda \det A]^{-1/2}$$
$$= [1 + 4q\sigma_\Theta^2 + 4q^2\sigma_\Theta^4(1 - K^2)]^{-1/2}$$

$$(D.10)$$

and

$$(\underline{f}^T A^{-1} \underline{f})/4$$
$$= \beta(c_x(x-v\tau_s) + c_y y)^2 + \gamma (c_x v\tau_d/2)^2$$

$$(D.11)$$

where

$$c_x \equiv (ka_x)^2\Phi_x/L$$

$$c_y \equiv (ka_y)^2 \Phi_y / L \tag{D.12}$$

$$\beta \equiv \sigma_\Theta^2 (1 + K + 2q\sigma_\Theta^2(1-K^2)) \ / \ (1 + 4q\sigma_\Theta^2 + 4q^2\sigma_\Theta^4(1 - K^2))$$

$$\gamma \equiv \sigma_\Theta^2 (1 - K + 2q\sigma_\Theta^2(1-K^2)) \ / \ (1 + 4q\sigma_\Theta^2 + 4q^2\sigma_\Theta^4(1 - K^2))$$

Combining all these, we wind up with the following expression for $< I_y(t) >$

$$
\begin{aligned}
< I_y(t) > = {} & P_T(k^2 a_x a_y / 2\pi L^2)^2 \ \lambda^2 \exp[-2\alpha L] \int d\bar{p} \ \mathcal{J}(\bar{p}) \\
& \cdot \exp[-2(ka_x/2L)^2(x-vt)^2 - (ka_y/L)^2 y^2] \\
& \cdot \iint d\tau_s d\tau_d \ \exp[-2j(kv/L)(x-vt)\tau_d] \\
& \cdot \exp[-2(ka_x/2L)^2(v\tau_d)^2] \\
& \cdot \exp[-2(ka_x/L)^2(v\tau_s - (x+vt)/2)^2] \\
& \cdot [1 + 4q\sigma_\Theta^2 + 4q^2\sigma_\Theta^4(1 - K^2)]^{-1/2} \\
& \cdot \exp[\ \beta(c_x(x-v\tau_s) + c_y y)^2] \\
& \cdot \exp[\ \gamma(c_x v\tau_d/2)^2].
\end{aligned} \tag{D.13}
$$

We can carry out the τ_s-integral, with the result

$$
\begin{aligned}
\int d\tau_s \ [\ \ldots\ ] = {} & [\pi/v^2(\alpha_x - \beta c_x^2)]^{1/2} \\
& \cdot \exp[(\alpha_x \beta/(\alpha_x - \beta c_x^2)) \cdot (c_x(x-vt)/2 + c_y y)^2]
\end{aligned} \tag{D.14}
$$

where

$$\alpha_x \equiv 2(ka_x/L)^2.$$

The τ_d-integral cannot be obtained in closed form.

REFERENCES

1. M.I. Skolnik, Introduction to Radar Systems, 2nd ed., McGraw-Hill, New York, 1980.

2. W.I. Thompson,III, Atmospheric Transmission Handbook, Technical Report for NASA, Report No. DOT - TSC - NASA - 71 - 6, Washington, D.C., 1971.

3. R.C. Harney and R.J. Hull, "Compact Infrared Radar Technology," CO_2 Laser Devices and Applications, Proc. SPIE, Vol. 227, 1980.

4. A.B. Gschwendtner, R.C. Harney and R.J. Hull, "Coherent IR Radar Technology," D.K. Killinger and A. Mooradian (eds), Optical and Laser Remote Sensing, Springer-Verlag, Berlin, 1983.

5. C.C. Aleksoff, J.S. Accetta, L.M. Peterson, et. al., "Synthetic Aperture Imaging with a Pulsed CO_2 TEA Laser," Laser Radar II, Proc. SPIE, Vol. 783, 1987.

6. J.H. Shapiro, B.A. Capron and R.C. Harney, "Imaging and Target Detection with a Heterodyne-Reception Optical Radar," Applied Optics, Vol. 20, No. 19, October 1981.

7. J.Y. Wang and P.A. Pruitt, "Laboratory Target Reflectance Measurements for Coherent Laser Radar Applications," Applied Optics, Vol. 23, No. 15, 1984.

8. H.L. Van Trees, Detection, Estimation, and Modulation Theory, Part III, John Wiley and Sons, New York, 1968.

9. W.L. Wolfe and G.J. Zissis (eds), The Infrared Handbook, Environmental Research Institute of Michigan, Chs. 5 and 6 (Eq. (6-20)), Ann Arbor, MI, 1978.

10. J.H. Shapiro, Class Notes for Optical Detection and Communication, 6.453, Dept. of Elect. Engin., MIT.

11. D.M. Papurt, J.H. Shapiro and S.T. Lau, "Measured Turbulence and Speckle Effects in Laser Radar Target Returns," Coherent Infrared Radar Systems and Applications II, Proc. SPIE, Vol. 415, 1983.

12. J.W. Goodman, "Statistical Properties of Laser Speckle Patterns," Laser Speckle and Related Phenomena, J.C. Dainty (ed.), Springer-Verlag, Berlin, 1975.

13. J.H. Shapiro, "Target Reflectivity Theory for Coherent Laser Radars," Applied Optics, Vol. 21, No. 18, September, 1982.

14. D.M. Papurt, J.H. Shapiro, R.C. Harney, "Atmospheric Propagation Effects on Coherent Laser Radars," Physics and Technology of Coherent Infrared Radar, Proc. SPIE, Vol. 300, 1981.

15. J.H. Shapiro, "The Correlation Scales of Laser Speckle in Heterodyne Reception", Applied Optics, Vol. 24, June 1985.

16. J.H. Shapiro, R.W. Reinhold and D. Park, "Performance Analyses for Peak-detecting Laser Radars," Laser Radar Technology and Applications, Proc. SPIE, Vol. 663, 1986.

17. R.O. Harger, Synthetic Aperture Radar Systems, Academic Press, New York, 1970.

18. D.R. Wehner, High Resolution Radar, Artech House, Dedhmam, MA, 1987.

19. J.L. Walker, "Range-Doppler Imaging of Rotating Objects," IEEE Trans. on AES, Vol. AES-16, No. 1, January 1980.

20. D.A. Ausherman, A. Kozma, J.L. Walker, et. al., "Developments in Radar Imaging," IEEE Trans. on AES, Vol. AES-20, No. 4, July 1984.

21. J.V. Evans and T. Hagfors, Radar Astronomy, McGraw-Hill, New York, 1968.

22. L.J. Porcello, et. al., "The Apollo Lunar Sounder Radar System," Proc. IEEE, Vol. 62, No. 6, June 1974.

23. J.H. Shapiro, "Reciprocity of the Turbulent Atmosphere," JOSA, Vol. 61, No. 4, 1971.

24 A. Yariv, Quantum Electronics, 2nd ed., John Wiley and Sons, New York, 1975.

25. A.E. Siegman, "The Antenna Properties of Optical Heterodyne Receivers," Proc. IEEE, Vol. 54, No. 10, October 1966.

26. W.K. Pratt, Digital Image Processing, John Wiley & Sons, New York, 1978.

27. T.S. Huang, G.J. Yang, and G.Y. Tang, "A Fast Two-Dimensional Median Filtering Algorithm," IEEE Trans. on ASSP, Vol. ASSP-27, No. 1, February 1979.

28. J. Lee, "Speckle Suppression and Analysis for Synthetic Aperture Radar Images," Optical Engineering, Vol. 25, No. 5, May 1986.

29. T.R. Crimmins, "Geometric Filter for Reducing Speckle," Optical Engineering, Vol. 25, No. 5, May 1986.

[Refs. 30-36 appear in Synthetic Aperture Radar, J.J. Kovaly (ed.), Artech House, Inc., Dedham, MA, 1976.]

30. W.M. Brown, "Synthetic Aperture Radar," IEEE Trans. on AES, Vol. AES-3, No. 2, March 1967.

31. J.A. Develet Jr., "Performance of a Synthetic-Aperture Mapping Radar System," IEEE Trans. on ANE, Vol. ANE-11, No. 3, September 1964.

32. L.J. Cutrona and G.O. Hall, "A Comparison of Techniques for Achieving Fine Azimuth Resolution," IRE Trans. on MIL, Vol. MIL-6, No. 2, April 1962.

33. J.A. Develet Jr., "The Influence of Random Phase Errors on the Angular Resolution of Synthetic-Aperture Radar Systems," IEEE Trans. on ANE, Vol. ANE-11, No. 1, March 1964.

34. C.A. Greene and R.T. Moller, "The Effect of Normally Distributed Random Phase Errors on Synthetic Array Gain Patterns," IRE Trans. on MIL, Vol. MIL-6, No. 2, April 1962.

35. L.J. Porcello, "Turbulence-Induced Phase Errors in Synthetic-Aperture Radars," IEEE Trans. on AES, Vol. AES-6, No. 5, September 1970.

36. L.A. Rondinelli and G.W. Zeoli, "Evaluation of the Effect of Random Tropospheric Propagation Phase Errors on Synthetic Array Performance," Eighth Annual Radar Symposium Record, University of Michigan, June 1962.

37. J.H. Shapiro and P.L. Mesite, "Performance Analyses for Doppler and Chirped Laser Radars," Appendix C in R.J. Hull, D.G. Biron, S. Marcus and J.H. Shapiro, "Coherent Laser Radar Remote Sensing," Final Report, MIT Lincoln Laboratory, September 1983, DTIC AD-A13944815.

38. R.L. Fante, "Electromagnetic Beam Propagation in Turbulent Media," IEEE Proc., Vol. 63, No. 12, December 1975.

[Refs. 39-42 appear in Laser Beam Propagation in the Atmosphere, J.W. Strohbehn (ed.), Springer-Verlag, Berlin, 1978.]

39. J.W. Strohbehn, "Introduction (Ch. 1)."

40. S.F. Clifford, "The Classical Theory of Wave Propagation in a Turbulent Medium (Ch. 2)."

41. J.W. Strohbehn, "Modern Theories in the Propagation of Optical Waves in a Turbulent Medium (Ch. 3)."

42. J.H. Shapiro, "Imaging and Optical Communication Through Atmospheric Turbulence (Ch. 6)."

43. R.L. Fante, "Electromagnetic Beam Propagation in the Turbulent Media: An Update," IEEE Proc., Vol. 68, No. 11, November 1980.

44. W.S. Ross, W.P. Jaeger, J. Nakai, et. al., "Atmospheric Optical Propagation - an Integrated Approach,", Optical Engineering, Vol. 21, No. 4, August 1982.

45. D.L. Fried, "Optical Heterodyne Detection of an Atmospher- ically Distorted Signal Wave Front," IEEE Proc., Vol. 55, No. 1, January 1967.

46. S. Wandzura, "Meaning of quadratic structure functions," JOSA, Vol. 70, June 1980.

47. N.E. Zirkind, Ph.D. Thesis Proposal, Dept. of Elect. Engin., MIT, September 1987.

48. R.E. Bellman, Introduction to Matrix Analysis (2nd Ed.), McGraw-Hill, New York, 1970.

49. L.A. Newman and R.A. Hart, "Recent R&D Advances in Sealed- Off CO_2 Lasers," Laser Focus/Electro-Optics, June 1987.

50. S. Marcus and G.M. Carter, "Electrooptically Q-Switched CO_2 Waveguide Laser," Applied Optics, Vol. 18, No. 16, August 1979.

51. D.L. Spears, "Theory and Status of High Performance Hetero- dyne Detectors," Physics and Technology of Coherent Infrared Radar, Proc. SPIE, Vol. 300, 1981.

52. G.M. Carter and H.A. Haus, "Optical Single Sideband Genera- tion at 10.6 μm," IEEE JQE, Vol. QE-15, No. 4, April, 1979.

53. L.M. Laughman, R.J. Wayne, and C.R. Lane, "Programmable Transmitters for Coherent Laser Radars," Physics and Technology of Coherent Infrared Radar, Proc. SPIE, Vol. 300, 1981.

54. Private communication with R.J. Hull of MIT Lincoln Laboratory.

55. D.U. Fluckiger, R.J. Keyes, and J.H. Shapiro, "Optical Autodyne Detection: Theory and Experiment," Applied Optics, Vol. 26, No. 2, January 1987.

BIOGRAPHICAL NOTE

Dongwook Park was born in Seoul, Korea on December 15, 1959 as the oldest of three children to Young Joon Park and Ok Hee Shim. He received S.B., S.M., and Ph.D. degrees in electrical engineering in June 1982, June 1984, and January 1988, respectively, at MIT. His research interests are in the fields of laser radar, optical communication, and electromagnetics. Mr. Park is a member of Tau Beta Pi, SPIE, and IEEE. He is currently employed at the Electronic Systems Group, TRW in Redondo Beach, Calif.